universität
wien

MASTERARBEIT / MASTER'S THESIS

Titel der Masterarbeit / Title of the Master's Thesis

„Measurement of ion residence times in the ILIAMS cooler with a new multi-beam switcher"

verfasst von / submitted by

Felix Maximilian Albrecht, B.Sc.

angestrebter akademischer Grad / in partial fulfilment of the requirements for the degree of

Master of Science (MSc)

Wien, 2024 / Vienna, 2024

Studienkennzahl lt. Studienblatt / degree programme code as it appears on the student record sheet:	UA 066 876
Studienrichtung lt. Studienblatt / degree programme as it appears on the student record sheet:	Masterstudium Physics
Betreut von / Supervisor:	Univ.-Prof. Dipl.-Ing. Dr. Robin Golser
Mitbetreut von / Co-Supervisor:	Mag. Dr. Martin Martschini

Danksagung (Acknowledgements)

An erster Stelle möchte ich meinen aufrichtigen Dank an Robin Golser aussprechen. Seine Betreuung und Unterstützung während der Durchführung und Verfassung meiner Masterarbeit waren entscheidend. Nicht minderer Dank gebührt Martin Martschini, der mich tatkräftig bei Messungen, Datenauswertung, dem Bau und dem Korrekturlesen der Arbeit unterstützt hat. Ohne seine hervorragende Mitbetreuung wäre das Ergebnis nicht dasselbe.

Ein besonderer Dank geht an Michael Kern, dessen Hilfe bei der detaillierte Planung und dem Bau des MBS für den Erfolg meiner Arbeit von essentieller Bedeutung waren. Seine Hingabe während der Fertigung und des Einbaus der Bauteile verdienen besondere Anerkennung. Daniel Baumgartner möchte ich danken für die Einführung in COMSOL sowie seine Magnetfeld-Simulationen, die anregenden Diskussionen über die Physik hinter dem Ionenkühler sowie für sein Korrekturlesen einiger Kapitel meiner Arbeit.

Silke Merchel gebührt mein Dank für die geduldige Einführung in die Probenaufbereitung und das Pressen von Chlorproben. Ebenso schätze ich ihre Hilfe beim Korrekturlesen einiger Abstracts sowie ihre Tipps zu Vorträgen. Besonderer Dank gilt auch Peter Steier für seine zahlreichen Hilfestellungen bei Messungen und Reparaturen am Beschleuniger sowie für die interessanten Gespräche über Physik und Netzwerktechnologie.

Helga Schmelzer-Vincro und Sigrid Lielacher gilt mein Dank für die hilfsbereite Unterstützung bei allen administrativen Angelegenheiten. Außerdem gebührt Markus Schiffer mein Dank für seine fortwährende Hilfsbereitschaft bei Fragen zur Ionenoptik, zum Bau des MBS sowie zur Messung von Verweildauern.

Des Weiteren möchte ich Stephanie Adler, Sophie Schoberleitner, Tabea Fuchs, Aline Zoufal, Alexander Wieser, Oscar Marchhart, Andreas Wiederin, Leopold Unterweger und Denis Ibrahimovic für die anregenden Diskussionen über AMS und ILIAMS danken. Ein großer Dank geht an alle bereits genannten für die unterhaltsamen Mittagspausen und Seminar-Nachsitzungen.

Michael Paping gebühren Dank und Anerkennung für das selbstlose Korrekturlesen eines Großteils meiner Arbeit.

Zuletzt, und eigentlich zuallererst, möchte ich meine aufrichtige Dankbarkeit gegenüber meinen Eltern ausdrücken. Ihre stetige Unterstützung war für mich von unschätzbarem Wert. Nicht weniger gilt mein herzlicher Dank meiner Freundin Miele für ihren emotionalen Rückhalt und ihre fortwährende Unterstützung. Ohne euch alle hätte ich diese Masterarbeit nicht erfolgreich abschließen können!

Zusammenfassung

Der **Vienna Environmental Research Accelerator (VERA)** ist ein Beschleunigermassenspektrometer, mit dem Verhältnisse von Radioisotopen zu stabilen Isotopen bis zu 10^{-16} in einem Ionenstrahl aus Probenmaterial bestimmt werden können. Dazu müssen Isobare, Teilchen gleicher Masse die oft um Größenordnungen häufiger auftreten, von den zu vermessenden Isotopen getrennt werden. Bei VERA wurde das weltweit einzigartige Setup zur **Ion-Laser InterAction Mass Spectrometry (ILIAMS)** entwickelt, bei dem der Ionenstrahl in einem Ionenkühler auf kinetische Energien im Bereich von eV gebracht wird. Reaktionen mit einem Gas sowie Photodetachment mithilfe eines Lasers führen zur Neutralisation der anionischen Isobare, wobei die Verweildauer der Ionen im Kühler entscheidend für den Grad der Unterdrückung ist. Diese hängt maßgeblich vom injizierten Ionenstrom ab, und kann durch den Gasdruck eines Puffergases sowie das Potential von Leitelektroden im Kühler variiert werden. Bislang wurde der Ionenstrahl mit einem Dipolmagneten in den Kühler injiziert, was einen schnellen Wechsel der zu injizierenden Masse verhindert.

Im Rahmen dieser Arbeit wurde mithilfe von Simulationen ein neuer Multi-Beam-Switcher (MBS) konstruiert. Das Anlegen einer Spannung bis 5 kV an der Vakuumkammer im Magneten führt zu einer Beschleunigung und somit veränderten Ablenkung der Ionen. Die vorhandene Kammer wurde elektrisch von der restlichen Beamline isoliert und mithilfe eines Schaltnetzteils lässt sich die Spannung so schnell ändern (134 V/µs), dass nahezu instantan zwischen verschiedenen Isotopen gewählt werden kann, die in den Kühler injiziert werden. Dies kann in Zukunft genutzt werden, um die Reproduzierbarkeit von AMS-Messungen mit ILIAMS zu erhöhen.

Da das elektrische Feld der Magnetkammer die Ionenoptik und damit die Ionentransmission in den Kühler beeinflusst, waren ionenoptische Simulationen erforderlich. Der Ionenstrahl wurde mit SIMION 8.1 simuliert, um die Form von zusätzlichen Elektroden, die folglich an der Magnetkammer befestigt wurden, auf hohe Transmission zu optimieren. Darüber hinaus wurden Phasenraummessungen des Ionenstrahls vor dem Magneten durchgeführt, um realistische Ionentrajektorien für die Simulation zu erhalten, und somit den Aufbau vor dem Kühler genauer zu charakterisieren. Es wurde gezeigt, dass ein vorhandener x/y-Steerer als elektrostatische Quadrupollinse verwendet werden könnte, um den je nach Messbedingungen astigmatischen Strahl besser zu fokussieren und die Ionentransmission in den Kühler um bis zu 20 % zu erhöhen.

Schließlich wurden die Isolatoren und Elektroden des MBS eingebaut und damit die Verweildauer von $^{35}\mathrm{Cl}^{-}$- und $^{37}\mathrm{Cl}^{-}$-Ionen im Kühler bestimmt, indem dem Ionenstrahl

ein zeitlich definiertes Merkmal hinzugefügt wurde. Dazu wurden die beiden Isotope sequenziell in den Kühler injiziert und jeweils die Auswaschfunktion des Ionenstromes eines der Isotope beobachtet, anhand welcher die Verteilung der Verweildauer abgeleitet werden konnte. Bei typischen Einstellungen des Kühlers wurde eine mittlere Verweildauer eines $^{35}\text{Cl}^-$-Strahls bei einem injizierten Strom von 200 nA von 1.048(55) ms gemessen. Ein geringerer Strom von 55 nA eines $^{37}\text{Cl}^-$-Strahls erhöhte die mittlere Verweildauer auf 1.529(78) ms, eine weitere Stromreduktion auf 7 nA erhöhte sie weiter auf 2.092(21) ms.

Durch die unterschiedliche relative Häufigkeit der beiden Isotope ^{35}Cl und ^{37}Cl von 3:1 konnten außerdem Raumladungseffekte im Kühler beobachtet und charakterisiert werden, welche bislang nur durch Simulationen zugänglich waren. Dabei sorgte der intensivere $^{35}\text{Cl}^-$-Strahl bei seinem Einschuss für promptere Ejektion der zuvor injizierten $^{37}\text{Cl}^-$-Ionen aus dem Kühler, ein Effekt der schon 240 µs nach dem Wechsel der Isotope bemerkbar war. Die Raumladungseffekte propagierten damit je nach Puffergasdruck 4- bis 10-mal so schnell durch den Kühler wie die Ionen selbst.

Abstract

The **Vienna Environmental Research Accelerator (VERA)** is an accelerator mass spectrometer that is used to measure radioisotope-to-stable-isotope ratios down to 10^{-16} in an ion beam comprised of sample material. For this, isobars, particles of the same mass often orders of magnitude more abundant, need to be separated from the desired isotopes. At VERA, the world's unique setup for **Ion-Laser InterAction Mass Spectrometry (ILIAMS)** was developed, consisting of an ion cooler, in which the ion beam is decelerated to kinetic energies in the range of eV. Neutralization of the anionic isobars occurs through gas reactions and photodetachment using a laser, with the degree of suppression determined by the ion residence time in the cooler. The latter is chiefly dependent on the current of the injected ion beam and can be varied through the pressure of a buffer gas, as well as the field strength of guiding electrodes inside the cooler. So far, the ion beam has been injected into the cooler using a dipole magnet, which prohibits fast switching of the injected mass.

As part of this thesis, simulations aided in the design and construction of a new multi-beam switcher (MBS). The application of a voltage of up to 5 kV to the vacuum chamber inside the magnet leads to an acceleration and thus, a modified deflection angle of the ions. The existing chamber was electrically insulated from the rest of the beamline and using a switching power supply, this voltage can be rapidly changed (134 V/µs), enabling nearly instantaneous switching between particles of different mass injected into the cooler. In the future, this can be used to increase the precision of AMS measurements with ILIAMS.

To address ion-optical effects caused by the electric field of the magnet chamber, which in turn influence the ion beam transmission into the cooler, ion-optical simulations were necessary. The software SIMION 8.1 was used to optimize the shape of additional electrodes attached to the magnet chamber for high transmission. In addition, phase space measurements of the ion beam in front of the magnet were conducted to obtain realistic ion trajectories for simulations and subsequently characterise the setup in front of the cooler more accurately. It was shown that an existing x/y steerer could be used as an electrostatic quadrupole lens to better focus the, depending on measurement conditions, astigmatic beam and increase the ion transmission into the cooler by up to 20 %.

Ultimately, the installation of insulators and electrodes of the MBS allowed the measurement of the residence time of $^{35}\mathrm{Cl}^-$ and $^{37}\mathrm{Cl}^-$ ions in the cooler by introducing a time-defined feature to the ion beam. The two species were sequentially injected

into the cooler and for either isotope, the washout function of the ion beam current was observed, from which the residence time distribution could be derived. At typical cooler settings, the mean residence time of a $^{35}\mathrm{Cl}^{-}$ beam of 200 nA injected current was measured to be 1.048(55) ms. A reduced current of 55 nA of a $^{37}\mathrm{Cl}^{-}$ beam increased the mean residence time to 1.529(78) ms, and a further reduction to 7 nA increased it to 2.092(21) ms.

Notably, through the different relative abundances of the two ion species $^{35}\mathrm{Cl}$ and $^{37}\mathrm{Cl}$ of 3:1, space charge effects inside the cooler were directly observed, previously accessible only by computer simulations. Upon its injection, the more intense $^{35}\mathrm{Cl}^{-}$ ion beam led to an accelerated emission of the previously injected $^{37}\mathrm{Cl}^{-}$ ions out of the cooler, an effect observable already 240 µs after the change of isotopes. Depending on the buffer gas pressure, space charge effects thus propagated through the cooler 4 to 10 times as fast as the ions themselves.

Abbreviations

AMS	Accelerator Mass Spectrometry
BM	Bending Magnet
CDF	Cumulative Distribution Function
ESA	Electrostatic Analyser
ILIAMS	Ion-Laser InterAction Mass Spectrometry
MBS	Multi-Beam Switcher
MCP	MicroChannel Plate
PDF	Probability Density Function
PEEK	Polyether Ether Ketone
RTD	Residence Time Distribution
SNICS	Source of Negative Ions by Caesium Sputtering
SR	Slew Rate
SRS	Stanford Research Systems
TOF	Time of Flight
VERA	Vienna Environmental Research Accelerator

Contents

1 Introduction & Motivation

The Vienna Environmental Research Accelerator (VERA) is a state-of-the-art facility for Accelerator Mass Spectrometry (AMS), a method for detecting and quantifying radioisotopes of very low abundance in sample materials, with radioisotope-to-stable-isotope ratios down to 10^{-16} (Kutschera et al., 2023). The isotopes of interest are typically long-lived radionuclides, which can be used for a variety of applications such as chronological dating, e.g. with isotopes produced by cosmic rays in the atmosphere (like ^{14}C or ^{36}Cl), or tracing of environmental processes, e.g. with artificially produced isotopes that are leaked into the environment, like ^{129}I or ^{90}Sr. For more applications of AMS, cf. (Kutschera, 2013). In Figure 1, an overview of the VERA facility is shown.

VERA is distinct from other AMS laboratories due to the unique Ion-Laser InterAction Mass Spectrometry (ILIAMS) setup, which allows access to isotopes typically not available for low- to medium energy accelerators such as the 3 MV tandem at VERA. It was developed around ten years ago, and its characterization and development still is at the centre of research activities at VERA. This thesis aims to describe the process of building and integrating a new multi-beam switcher into the ILIAMS beamline, as well as using it to measure ion residence times, and for the first time directly observe space charge effects inside the ILIAMS cooler. The following sections go into detail about AMS in general, ILIAMS specifically, as well as the physical basics behind the simulations and measurements presented in this work.

1.1 Accelerator mass spectrometry (AMS)

The typical procedure for AMS is to create an ion beam out of a sample, often through a sputtering and extraction process, followed by magnetic and electrostatic mass separation. A large electrostatic accelerator, producing voltages in the order of MV, is then used to break up molecules in the ion beam and bring the ions to high energies, at which the separation of isobars (other particles of nearly the same mass) is possible, see section 1.2. A typically used ion source is the "Source of Negative Ions by Caesium Sputtering" (SNICS), of which two are in operation at the VERA lab. For the mass separation, magnetic and electric fields are used, in which ions of different momentum and energy, respectively, are deflected differently, allowing for a tunable mass spectrometry system.

The isotopes of interest are so low in abundance, that they have to be counted by

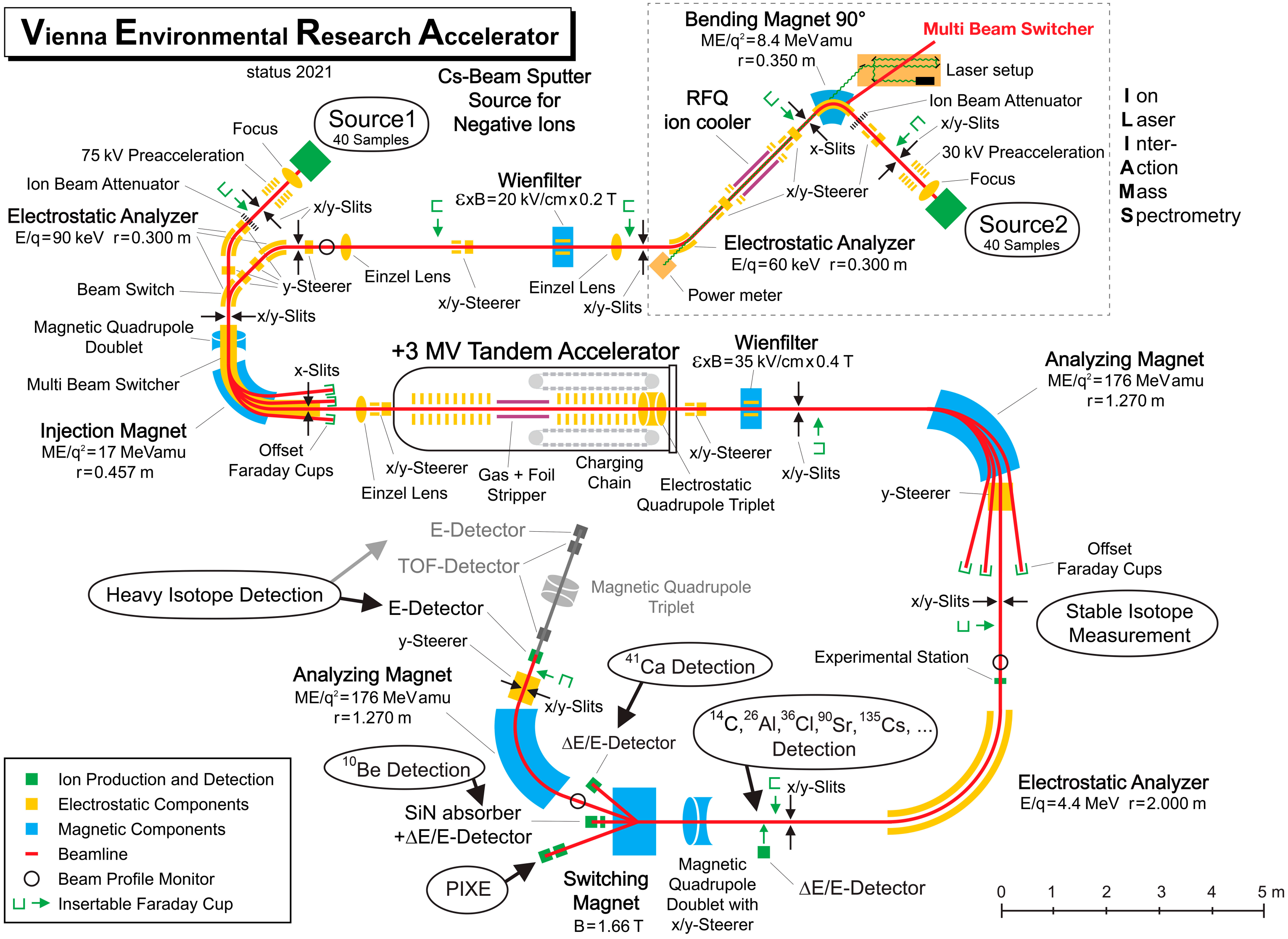

Figure 1: Overview of the VERA setup, including the new multi-beam switcher in the top right corner.

detectors after the accelerator. To cancel out unknown variables in chemical preparation, target handling and the measurement itself, one also has to measure a stable reference isotope of known abundance, leading to an isotope ratio as the final AMS measurement result. This affords the ability to measure at least nA ion currents from a stable beam, most commonly employing a Faraday cup.

1.1.1 Bending magnet

Inside a bending magnet (BM) with flux density B, moving charged particles follow a circular path with radius r, because the Lorentz force acts as a centripetal force:

$$\begin{aligned} F_\mathsf{L} &= F_\mathsf{Z} \\ q \cdot v \cdot B &= \frac{m \cdot v^2}{r} \\ \Rightarrow \quad \rho_\mathsf{m} := r \cdot B &= \frac{m \cdot v}{q} = \frac{\sqrt{2mE_\mathsf{kin}}}{q} \end{aligned} \tag{1}$$

The expression ρ_m is called magnetic rigidity and is to be met by the BM. Ions of the same velocity, mass and charge are thus deflected in the same way, which is why a BM is considered a filter for momentum over charge (Steier, 2000). While the desired radius r is usually fixed, the flux density B can be varied in an electromagnet, with the current I being proportional to B.

A dipole magnet typically consists of two coils of wires wrapped around two ends of a yoke, separated by an air gap of thickness g. Inside this gap, a homogeneous magnetic field is created by a current I running through the $N/2$ windings of each coil. The length within the yoke that the magnetic field has to permeate through to get from one pole to the other is called the iron path l. The magnetic flux density B can be calculated by the following formula:

$$B = \frac{\mu_0 \cdot \mu_r \cdot N \cdot I}{\mu_r \cdot g + l} \tag{2}$$

The magnet used in this thesis is made by Danfysik and has the properties $g = 50\,\mathsf{mm}$, $r = 350\,\mathsf{mm}$, $B_\mathsf{max} = 1.23\,\mathsf{T}$ and is shown in Figure 2. The shape of the magnet and yoke affects the homogeneity of the field (Hinterberger, 2008), in this case, an H-shaped magnet is used: the yoke is closed on both sides, with pole shoes extending from the top and bottom inner sides of the yoke. The iron length l was measured to be about 778 mm for this particular magnet, and a relative magnetic permeability of $\mu_r = 5000$ can be assumed for the iron yoke and pole shoes (Nave, 2017).

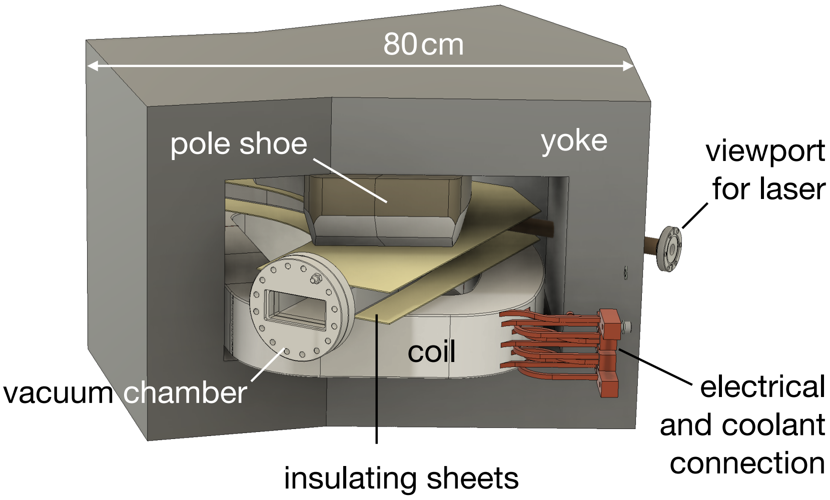

Figure 2: 3D render of the magnet used in this thesis. The top coil is hidden for better visualisation.

1.1.2 Electrostatic analyser

An energy filter can be realised by an electrostatic analyser (ESA), which creates an electric field gradient where ions experience a Coulomb force perpendicular to their flight direction, again acting as a centripetal force:

$$\begin{aligned} F_\mathsf{C} &= F_\mathsf{Z} \\ q \cdot \mathcal{E} &= \frac{m \cdot v^2}{r} \\ \Rightarrow \quad \rho_\mathsf{e} := r \cdot \mathcal{E} &= \frac{m \cdot v^2}{q} = \frac{2E_\mathsf{kin}}{q} \end{aligned} \tag{3}$$

Combining both ESA and BM after each other leads to a mass filter (or rather, mass-by-charge), as fixed energy and momentum result in a fixed velocity as well as mass.

1.1.3 Wien filter

A magnetic and electric field can be set up perpendicular to each other, with an electric field created by two parallel plates with distance d and potential difference U, and a magnetic flux density B created by an electromagnet. The Coulomb and Lorentz forces acting on ions following a straight path cancel out, leading to a velocity- or Wien filter:

$$\begin{aligned} F_C &= F_L \\ q \cdot \mathcal{E} &= q \cdot v \cdot B \\ \Rightarrow v &= \frac{\mathcal{E}}{B} = \frac{U}{B \cdot d} \end{aligned} \tag{4}$$

By combining a Wien filter with an ESA or a BM, a mass spectrometer can be designed.

1.1.4 Multi-beam switcher

In a multi-beam switcher (MBS, also called bouncer magnet), an enhancement to a BM, the magnet chamber is set to a potential U relative to the beamline, which accelerates the ions to $E_{\text{kin}} + qU$, modifying the rigidity as compared to equation (1):

$$\rho_{\text{mbs}} = r \cdot B = \frac{\sqrt{2m(E_{\text{kin}} + qU)}}{q} \tag{5}$$

For a positive qU, an ion with the same mass would need a higher magnetic field to be kept on the same path as with $qU = 0$. Thus, an extra acceleration acts in the same way as a reduction in magnetic field. The current through the magnet coils is only loosely proportional to B, because of hysteresis in the iron yoke of the BM. Fast switching of B and thus ρ_{m} is therefore limited in accuracy and time, which can be alleviated by using a variable acceleration in the magnet chamber. This can be illustrated by e.g. a Cl^- ion beam consisting of the isotopes ^{35}Cl and ^{37}Cl, with a kinetic energy of 30 keV, see Figure 3.

When the magnetic flux density is adjusted to $B \approx 4334\,\text{G}$, only $^{37}\text{Cl}^-$ can pass the BM at 90° deflection (see equation (1)). By now applying a voltage of $U \approx 1714\,\text{V}$ to the magnet chamber, the ion beam is accelerated towards the chamber and has a higher velocity in the magnetic field, allowing only the 2 amu lighter isotope of $^{35}\text{Cl}^-$

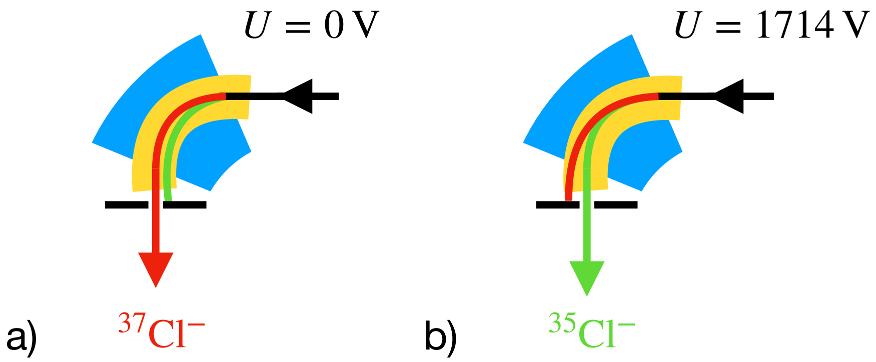

Figure 3: Illustration of multi-beam switching between $^{35}\text{Cl}^-$ and $^{37}\text{Cl}^-$ at 30 keV kinetic energy. In both cases, the magnet shown in blue is set to $B = 4334\,\text{G}$ and has a nominal bending radius of 350 mm. In the left panel, the MBS shown in yellow is at ground potential, and $^{37}\text{Cl}^-$ is injected through the slits at the magnet exit, while the lighter $^{35}\text{Cl}^-$ has a smaller trajectory radius (see equation (1)) and hits the slits. In the right panel 3b, a voltage of 1714 V is applied to the MBS electrode, which accelerates the ions towards the chamber, resulting in larger trajectory radii and the $^{35}\text{Cl}^-$ ions going through the slits.

to pass. This MBS mode is hereafter called “2 amu down”.

If the magnet with ρ_m is set to let through m_magnet, and a switch to mass m_wanted is desired, one can obtain the needed voltage U by equating $\rho_\mathrm{m}(m_\mathrm{magnet}) = \rho_\mathrm{mbs}(m_\mathrm{wanted})$, as in equations (1) and (5). Solving for U gives:

$$U = \frac{E_\mathrm{kin}}{q} \cdot \left(\frac{m_\mathrm{magnet}}{m_\mathrm{wanted}} - 1 \right) \tag{6}$$

To obtain the maximum switching capability of the MBS Δm_max depending on a maximum voltage U_max, one can solve this equation for $m_\mathrm{wanted} - m_\mathrm{magnet}$ and truncate to the next lower atomic mass:

$$\Delta m_\mathrm{max} = \mp \left\lfloor \left| m_\mathrm{magnet} \cdot \frac{E_\mathrm{kin}}{E_\mathrm{kin} \pm qU_\mathrm{max}} - 1 \right| \right\rfloor \tag{7}$$

This equation is plotted in Figure 4, where the values $U_\mathrm{max} = 5$ and 10 kV, and

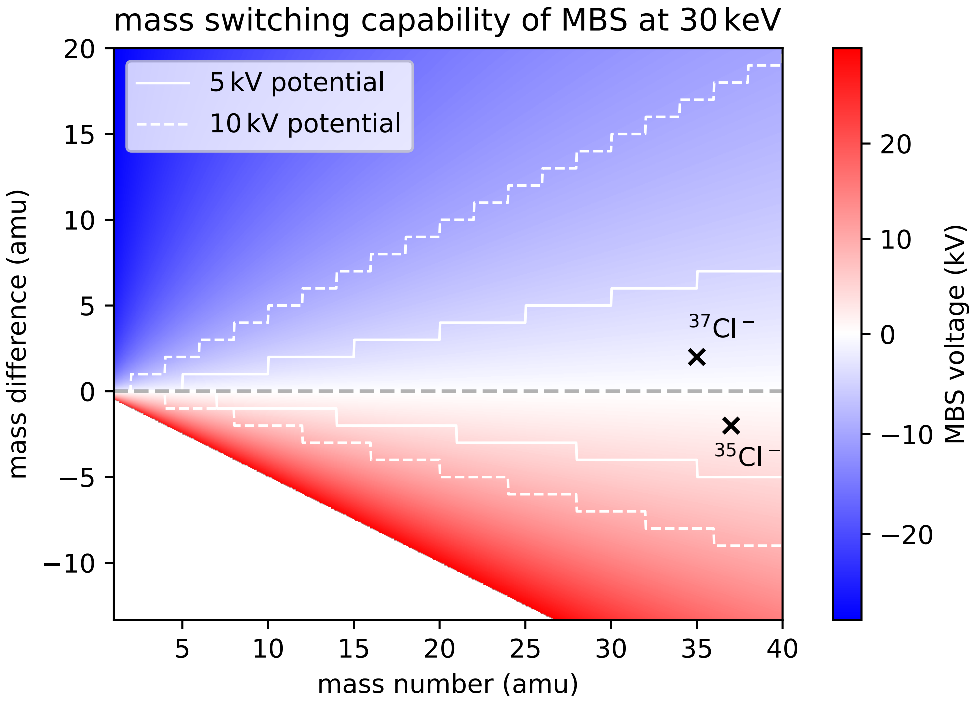

Figure 4: Theoretical switching capability of an MBS with a 30 keV anion beam at a potential of up to 5 and 10 kV, respectively. The x-axis shows the mass number m_magnet to which the BM is set, and the y-axis shows the mass difference Δm that is to be switched by the MBS. The colours show the voltage needed for a particular combination of m_magnet and Δm calculated with equation (6). Equipotential lines at 5 and 10 kV, truncated to integer atomic mass, show the range of an MBS with the respective maximum rated voltages, calculated with equation (7). Markers indicate the voltage needed to switch between ^{35}Cl$^-$ and ^{37}Cl$^-$, either “2 amu up” or down (the final isotope exiting the MBS is shown).

$q = -e$ were used for reference. The magnet chamber voltage is typically provided by a switching power supply, so it can be adjusted very fast and accurately (some models offer slew rates of 100 V/µs and accuracies better than 1 V), allowing for the beam to be switched at µs intervals.

In AMS measurements, an MBS is typically used to quickly switch between the rare and stable isotopes, a technique called bouncing. The desired value of the measurement is the ratio between radio- and stable isotope, so the count rate and ion current, respectively, have to be measured. The current coming from the sputtering target typically decreases over time, so it is favourable to bounce within fractions of a second between the two isotopes, increasing the precision of the measured value.

1.2 Ion-Laser InterAction Mass Spectrometry (ILIAMS)

As outlined in subsection 1.1, magnetic and electric fields in conjunction can separate ions by their mass-to-charge ratio. This means that isobars, which are isotopes or molecules with the same number of nucleons, can be mistaken as the isotope of interest. To separate these isobars, several techniques are typically used in AMS, including the use of high acceleration voltages (several MV), gas-filled magnets, gas ionization chambers with segmented anodes to measure energy loss spectra, and more (Martschini et al., 2021). These methods are particularly efficient at high acceleration voltages, bigger than the 3 MV acceleration achievable by the tandem accelerator at VERA. Another method of isobar suppression was thus developed: Ion-Laser InterAction Mass Spectrometry (ILIAMS) (Martschini et al., 2019). Its working principle is to neutralise the isobar by gas reactions in combination with photodetachment by a laser and consists of a section of the low-energy beamline called the ion cooler, in which the ion beam is slowed down to almost thermal energies.

The ion cooler essentially is a 1 m-long RF quadrupole with DC guiding electrodes, filled with Helium buffer gas, and sitting between electrostatic deceleration and acceleration lenses. Additionally, a laser is aligned collinearly with the ion beam inside the cooler, to enable laser photodetachment during the ion residence time in the cooler.

The ions have around 30 keV when they reach the injection lens, which uses electric fields to slow down the beam to around 50 eV. At this point, an aperture of 3 mm diameter acts as an entrance to the cooler, where collisions with the Helium buffer gas slow the ions further down to thermal energies. Space charge effects and the DC guiding electrodes slowly lead the ions towards the extraction lens, with ion residence times in the order of milliseconds.

Laser photodetachment is a process in which a bound electron is highly excited by a photon, leading to the neutralization of the isobaric anions and thus their suppression in the ion beam. In order to leave the isotope of interest unaffected, this requires that its photodetachment energy is higher than the isobar's, so that a laser energy can be chosen between the two values. The photodetachment efficiency or suppression factor f_{supp} is determined by the photon flux ϕ, the photodetachment cross section σ and the interaction time t (Liu et al., 2005):

$$f_{\text{supp}} = \frac{N_0}{N(t)} = e^{\sigma\phi t} \tag{8}$$

At typical values of $\phi \approx 5 \times 10^{20}\,\text{cm}^{-2}\text{s}^{-1}$ and $\sigma \approx 10^{-17}\,\text{cm}^2$ (Martschini et al., 2021), the ion residence time in the cooler should be in the ms regime for efficiencies of several orders of magnitude.

One should note that this only governs the isobar suppression efficiency due to laser photodetachment. Adding a reactive gas such as O_2 to the He buffer gas can lead to additional isobar suppression (Litherland et al., 2007). The efficiency of this is also higher at longer residence times. There is an ion cooler installed in the AEL-AMS facility at uOttawa, which solemnly relies on this principle, cf. (Flannigan, 2024). Furthermore, developments towards an ILIAMS-like system for isobar suppression are underway at CologneAMS (Schiffer et al., 2022).

1.3 Residence Time Distribution (RTD)

As equation (8) shows, the ion residence time in the cooler is of importance for its isobar suppression capability. Moreover, to further understand the physics inside the cooler, it is a useful property to measure.

In chemistry, more specifically in reaction engineering, the notion of the residence time distribution (RTD) is well known and established (Levenspiel, 1998). In a chemical reaction vessel, several chemicals are mixed to produce a desired product. The efficiency of the chemical reaction is dependent on the residence time of the reactants inside the reaction vessel, so the RTD is important to know. Several theoretical models of reaction vessels exist, for which the RTD can be calculated analytically. An RTD measurement of an actual vessel can then quantify how well it can be approximated by a particular theoretical model (Danckwerts, 1953).

In Figure 5, both a probability density function and cumulative distribution function are plotted as examples of an RTD, based on the Erlang distribution. The latter is the analytical RTD solution for a cascade of continuous stirred-tank reactors, a common chemical reactor model (Nauman, 2003). The Erlang distribution is based on the Gamma distribution, but the shape parameter a can only take integer values:

$$f(x,a) = \frac{x^{a-1} \cdot e^{-x}}{(a-1)!} \overset{a=2}{=} xe^{-x} \tag{9}$$

In the example shown in Figure 5, the distribution is shifted to the right by 0.33 s, to give a mean residence time of $\bar{t} = 3\,\mathrm{s}$.

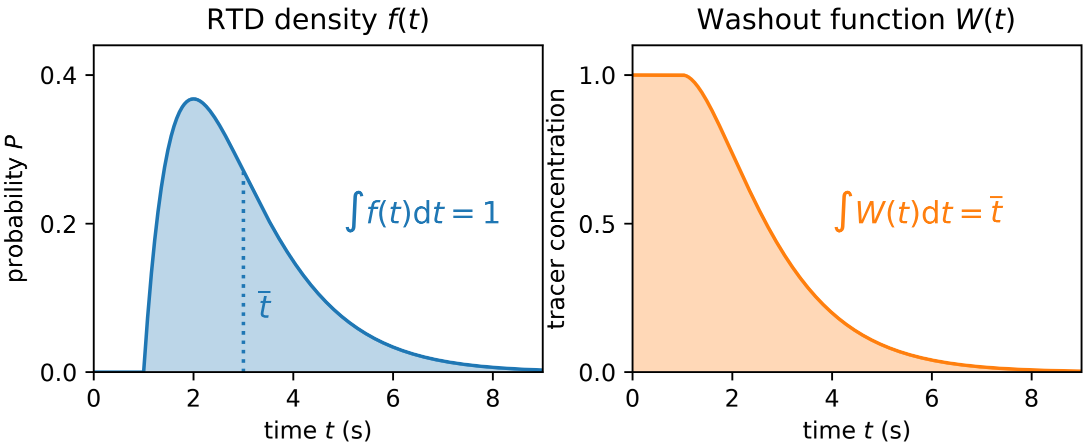

Figure 5: Residence time distribution based on the Erlang distribution with $a = 2$. On the left, the PDF $f(t)$ is shown, and on the right the washout function $W(t) = 1 - \int f(t)\mathrm{d}t$. Note that the distributions were shifted to the right by 0.33 s.

Even if no reaction gas is used in the ion cooler, the basic prerequisites for the description by residence time theory apply: A steady state, homogeneous flow system with a single in- and outlet, with unidirectional flow Q across it. The only limitation might be that in contrast to reaction vessels, particles might get lost inside the cooler, which means $Q_{\text{out}} < Q_{\text{in}}$. However, the transmission through the cooler can be optimised up to 80 % (Martschini et al., 2021), with losses attributed mostly to suboptimal injection, and not necessarily to losses inside the cooler, so residence time theory still represents a reasonable approximation (Nauman, 2008).

Consider the ion cooler as a reaction vessel with a steady flow of a particular ion species through in- and outlet. At $t = 0$, a tracer with a delta distribution (i.e. a short ion pulse) is sent into the inlet, possibly mixing with the ions inside the cooler, and leaving through the output, where the tracer species' ion beam current is measured over time. One can integrate the measured current over time (and divide it by an individual ion's charge e) to obtain the amount of tracer species N used for this so-called pulse experiment. Normalizing the measured curve to $N \cdot e$ yields the residence time distribution density $f(t)$, which for each time t represents the fraction of ions with a residence time of t (Nauman, 2003). As any probability density function (PDF), it has a mean $\bar{t}$ and variance σ_t^2, and its integral is normalised to one: $\int f(t)\mathrm{d}t = 1$.

Now consider another experiment, in which the ion species is switched at $t = 0$ from the tracer to the other species. In this so-called step-off experiment, the tracer species' current usually decreases monotonically, and again one can integrate the measured ion beam current to obtain N, which in this case corresponds to the number of tracer ions inside the cooler at $t = 0$. Normalizing the measured curve to the initial ion beam current I_0, one yields the washout function $W(t)$, which represents the fraction of ions that have a residence time longer or equal to t. One can relate the washout function to the RTD density: $F(t) := 1 - W(t) = \int_0^t f(\tau)\mathrm{d}\tau$, if $W(t)$ is monotonically decreasing, which makes $F(t)$ the cumulative distribution function (CDF) of the RTD. $F(t)$ can also be measured by a step experiment when the tracer influx is started at $t = 0$ instead of stopped, which is called a step-on experiment. The mean residence time can be easily calculated as the first moment of the PDF (Nauman, 2008), and is related to the cooler inventory N:

$$\bar{t} = \int_0^\infty t \cdot f(t)\,\mathrm{d}t = \int_0^\infty W(t)\,\mathrm{d}t = \frac{N \cdot e}{I_0} \tag{10}$$

The variance σ_t^2 is in turn the second moment of the PDF around the mean, cf. (Nauman, 2008):

$$\sigma_t^2 = \int_0^\infty (t - \bar{t})^2 \cdot f(t)\,\mathrm{d}t = -\bar{t}^2 + 2 \cdot \int_0^\infty t \cdot W(t)\,\mathrm{d}t \tag{11}$$

It is favourable to calculate $\bar{t}$ from a step experiment, as it provides a more direct representation of the CDF (Nauman, 2003). Calculating $f(t)$ from a step experiment is then only a matter of taking the derivative of $W(t)$ or $F(t)$ with respect to time (Nauman, 2008):

$$f(t) = \frac{\mathrm{d}F(t)}{\mathrm{d}t} = -\frac{\mathrm{d}W(t)}{\mathrm{d}t} \tag{12}$$

If one is only interested in the mean residence time (and not the exact shape of the RTD), then the equilibrium requirement ($Q_{\mathsf{out}} = Q_{\mathsf{in}} = \text{const.}$) is already satisfied by a constant inflow of tracer ion species for $t < 0$, i.e. before changing to the other ion species. As long as the inflow is shut off abruptly at $t = 0$, one can integrate the outgoing ion beam current to obtain N and $\bar{t}$ via formula (10), regarding the condition the cooler was in up until $t = 0$. The actual residence time distribution would remain unknown though, but there's a way to get a measure for the distribution of residence times around the mean.

For this, one can note that $\bar{t}$, as calculated with formula (10), is actually the equilibrium mean residence time, because it represents the mean residence time with an equilibrium situation in the cooler. It only takes into account the area under this washout function, not its shape. If the washout function changes its shape, for example due to a space charge effect, but the mean value remains unchanged, one can define a weighted mean residence time to quantify this effect:

$$\bar{t}_{\mathrm{w}} = \frac{\int_{t_0}^{\infty} t \cdot W(t)\,\mathrm{d}t}{\int_{t_0}^{\infty} W(t)\,\mathrm{d}t} = \frac{\int_{t_0}^{\infty} t \cdot W(t)\,\mathrm{d}t}{(\bar{t} - t_0) \cdot I_0} \tag{13}$$

The lower bound to the integral t_0 could be chosen as 0 or another significant starting time, depending on the experiment. There is a similarity to the variance of the distribution, cf. equation (11), but in contrast to σ_t^2, the weighted mean residence time $\bar{t}_{\mathrm{w}}$ is normalised to the equilibrium mean residence time $\bar{t}$, and the integral starts from t_0, as compared to $t = 0$ for the variance.

2 Ion beam optics

In accelerator physics, the propagation of ion beams can be described similarly to that of light. As the same equations as in geometric light optics can be used, the application to accelerators is called ion beam optics.

In ion beam optics, it is often necessary or helpful to define a direction of propagation. This direction is commonly called z, with two orthogonal directions x and y. VERA uses a left-hand system, so when looking in the z-direction pretending to be the ion beam, the x direction is to the right and y to the top. The movement of a point mass can then be described using three positional parameters x, y and z, and three velocities v_x, v_y and v_z. To make it simpler, the relative position (offset) and velocity (energy spread) along z are often discarded, and the cylindrical symmetry of many ion optical devices further reduces the relevant parameters to two: x and v_x. Instead of the velocity, the angle with the z axis, $x' = \arctan(v_x/v_z)$ is commonly used, which is given in mrad. As the values of x' are usually very small, the small angle approximation $\tan(x') \approx x'$ can be applied, leading to $x' \approx v_x/v_z$. In total, one gets:

$$\vec{x} = \begin{pmatrix} x \\ x' \end{pmatrix} \tag{14}$$

x is the distance of a particle to the optical axis, while x' represents the velocity orthogonal to z. With this formalism, ion optical elements can be described as linear operations or matrices applied to the beam vector. The following matrices are used in subsequent calculations and are taken from (Hinterberger, 2008).

2.1 Matrix formalism

The drift section is the simplest element in matrix formalism, which applies to ions drifting without the influence of any electromagnetic field. The only value that changes for the ion is the position, namely: $x_1 = x_0 + \tan(x') \cdot l$, for a drift of length l, leading to:

$$\begin{pmatrix} 1 & l \\ 0 & 1 \end{pmatrix} \tag{15}$$

One of the simplest ion optical elements is a lens, that can be used for focusing a beam. A theoretical idealisation is the thin lens, which doesn't have any thickness, and is described by the following matrix:

$$\begin{pmatrix} 1 & 0 \\ -\frac{1}{f} & 1 \end{pmatrix} \tag{16}$$

The physical analogon is an Einzel lens, which is made by a succession of a grounded aperture, an aperture on a potential, and another grounded aperture. The voltage between the apertures and their distance determines the focal length f.

For injection into the ion cooler, the ion beam has to be slowed down electrostatically, which is done by a succession of apertures with increasing negative potential. It is essentially a succession of Einzel lenses, however, the distance between the apertures shouldn't be neglected as in the thin lens approximation. The tube lens is a better-fitting model, taking into account the length L and potential ratio $N = E_2/E_1$ in non-relativistic approximation:

$$T = \begin{pmatrix} \frac{3-\sqrt{N}}{2} & \frac{2L}{1+\sqrt{N}} \\ -\frac{3(N-1)(\sqrt{N}-1)}{8NL} & \frac{3\sqrt{N}-1}{2N} \end{pmatrix} \tag{17}$$

A homogeneous bending magnet with a nominal radius of ρ_0 and bending angle of α acts as a rotation in x and a drift section in y:

$$M_x = \begin{pmatrix} \cos\alpha & \rho_0 \sin\alpha \\ -\frac{\sin\alpha}{\rho_0} & \cos\alpha \end{pmatrix}, \quad M_y = \begin{pmatrix} 1 & \rho_0\alpha \\ 0 & 1 \end{pmatrix} \tag{18}$$

The pole shoes of a magnet are typically shaped so that their edge is at an angle β to the z plane of an incident beam. In the case of the magnet considered here, $\beta = 30°$. This so-called shimming angle has a focusing effect in y direction (Steier, 2000), and results in additional matrices:

$$E_x = \begin{pmatrix} 1 & 0 \\ \frac{\tan\beta}{\rho_0} & 1 \end{pmatrix}, \quad E_y = \begin{pmatrix} 1 & 0 \\ -\frac{\tan\beta_{\text{eff}}}{\rho_0} & 1 \end{pmatrix}, \tag{19}$$

with $\tan\beta_{\text{eff}} = \tan\beta - \frac{g(1+\sin^2\beta)}{\rho_0\cos^3\beta}K$. This effective edge angle is due to the y profile of a magnet edge, and its focusing strength is scaled by the empirical K value. For the common, so-called “Rogowski” edge profile shown in Figure 6, $K \approx 0.7$. The whole magnet is described by: $E \cdot M \cdot E$.

The cross-section of the pole shoes used in the magnet considered in this thesis shows a similar profile as Rogowski, however, an empirical approximation of the K value is

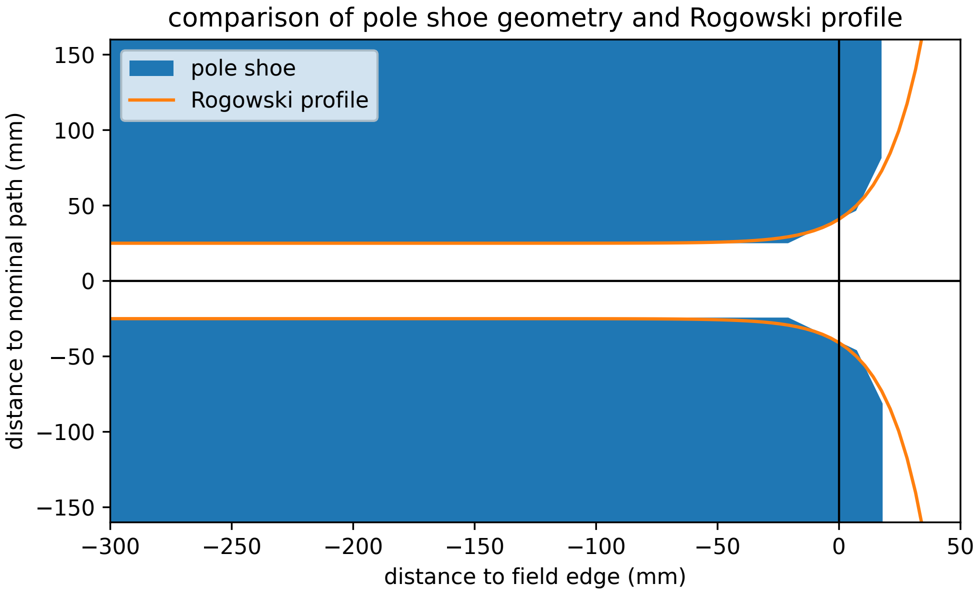

Figure 6: Profile of the bending magnet used in this thesis, shown along with the theoretical Rogowski profile, aligned at $x = 0$, cf. (Rogowski, 1923 and 1926) and (Lux, 1998).

shown in section 5.1.4.

The field edge shown in Figure 6 doesn't coincide with the so-called nominal magnet edge. The latter is defined such that a quarter circle of radius ρ_0 reaches from the nominal magnet edge at the entrance to the one on the exit. If one imagines the exiting beamline extending into the magnet, the nominal magnet edge at the entrance is at a distance of ρ_0 from this extension, in the perpendicular direction, and is sometimes itself called ρ_0.

A quarter circle with the nominal radius ρ_0 doesn't necessarily represent the actual flight path of the ions. As the magnetic fringe field reaches further than the nominal magnet edge ρ_0, the flight path starts to bend earlier. This effect is sometimes called "Enge effect", and is represented by another radius $\rho_{\text{enge}} > \rho_0$ (Wollnik, 1987). For the magnet used here with $\rho_0 = 350\,\text{mm}$, the manufacturer gives $\rho_{\text{enge}} = 365.2\,\text{mm}$ (Danfysik A/S, 2015).

While this radius better describes the flight path, it doesn't represent the ion optical effects described by the matrices (18) and (19). The radius ρ_{opt} that best describes the ion optical effect of the fringe field is close to, but lower than ρ_0, and has to be found empirically.

The edge focusing described by matrices (19) means that the magnet is acting as a focusing lens. A common rule of thumb for symmetric imaging of the waist by a BM is the following: Starting with a waist at $2\,\rho_0$ before the magnet, one yields a waist

$2\,\rho_0$ after the magnet, and not for different waist distances.

2.2 Phase space ellipse

An ion beam can commonly be characterised by the shape it takes in the six-dimensional phase space with coordinates (x, y, z, x', y', z'). For simplicity, one can neglect energy deviations z', as energy filters are commonly employed in accelerators. For any position z along the beamline, one can thus draw a representation of the beam in the two-dimensional x, x'- and y, y' phase spaces. In the following section, only x and x' are used, but the descriptions can be equivalently applied to the y direction.

An ion beam with a Gaussian profile occupies an elliptically shaped volume in this two-dimensional phase space, with the previously mentioned matrices acting as shearing transformations. Namely, a drift space acts as a shear in $+x$ direction, while a thin focusing lens can act as a shear in either $\pm x'$ direction.

An ellipse centred on a bivariate Gaussian distribution can be classified by how much of all values it inscribes, e.g. an ellipse where the half axes each correspond to one of the two standard deviations of the Gaussian distribution ($a = \sigma_1$, $b = \sigma_2$) would be called the 1σ-ellipse, containing 39.15 % of all values.

2.3 Parametric equation

The ellipse is used in this thesis in two places - ion beam phase space and bivariate Gaussian distributions. In the later sections, phase space measurements are fitted with the latter, and the 1σ-ellipse of the distribution is assumed to be the 1σ-ellipse of the phase space.

Bivariate Gaussian distributions can be parametrised easily as a tilted ellipse, which is shown here. The conversion between the tilted ellipse and the sheared ellipse needed for phase space is covered on page 101 in the Appendix.

One can express a tilted ellipse as an affine transformation of a unit circle: $\vec{x} = \vec{f_0} + \vec{f_1}\cos(t) + \vec{f_2}\sin(t)$, which is visualised in Figure 7. Using the standard 2D rotation matrix, one can define:

$$\vec{f_1} = a \cdot \begin{pmatrix} \cos\theta \\ \sin\theta \end{pmatrix}, \quad \vec{f_2} = b \cdot \begin{pmatrix} -\sin\theta \\ \cos\theta \end{pmatrix} \tag{20}$$

$$x(t) = a\cos\theta\cos t - b\sin\theta\sin t \tag{21}$$

$$x'(t) = a\sin\theta\cos t + b\cos\theta\sin t \tag{22}$$

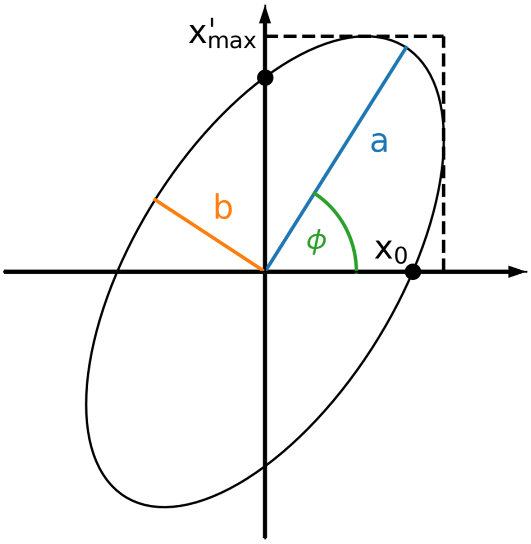

Figure 7: An affine transformation turns a unit circle into a tilted ellipse. The vectors $\vec{f}_1$ and $\vec{f}_2$ would point from the ellipse origin to its circumference along a and b, respectively.

The points x_0 and x'_{max} are of significance in the context of phase space ellipses. Although it is easy to parametrise the ellipse as tilted, it is not physically accurate concerning the propagation of an ion beam. If one imagines the phase space of a diverging beam at the waist, it is easy to see that it can be represented by an upright ellipse. As the beam diverges, imagine what happens to the point x_0 - its x'-coordinate is zero, so it does not diverge and stays exactly where it is. Also, the point x'_{max} with the maximum divergence changes only in x-direction - the divergence stays the same. Looking at the ellipse as a whole, it is sheared horizontally. The values x_0 and x'_{max} stay the same, a fact that is further explored in the following section. Formulas to calculate them can be found on page 101 in the Appendix.

The fact that x_0 and x'_{max} stay the same under linear transformations makes them useful characteristics of a phase space ellipse. If the ellipse is upright, i.e. at the waist, x_0 corresponds to σ_x, and x'_{max} to $\sigma_{x'}$. Instead of providing sigma values for a phase space, which doesn't give any information on the waist position, one can give x_0, x_{max}, and ϕ or d_{waist}.

The phase ellipse can also be expressed using the Courant-Snyder (CS) or Twiss parameters, namely α, β, and γ, which is common in particle beam dynamics. A conversion between sigma and CS notation is shown on page 103 in the Appendix.

2.4 Emittance

The emittance ϵ of a particle beam is related to the area it occupies in phase space. It is commonly defined as the area of an ellipse that contains a certain percentage of particles (Edwards & Syphers, 2008). Here, that percentage is chosen to be 39.35 %, which for a bivariate Gaussian distribution corresponds to a 1σ-wide ellipse. This is also called 1σ- or RMS emittance, or simply ϵ (Conte & Mackay, 2008).

The area is commonly calculated by the product of the semi-axes, or by the product of x_0 and x'_{max} (or vice versa) (Banford, 1966):

$$\epsilon_{1\sigma} = \frac{A}{\pi} = a \cdot b = x_0 \cdot x'_{\mathsf{max}} = x_{\mathsf{max}} \cdot x'_0 \tag{23}$$

Finding the values x_0, x'_0, x_{max} and x'_{max} given a and b is discussed on page 101 in the Appendix. As the values x_0 and x'_{max} don't change under a shear transformation, the emittance is thus conserved. Physically, this means that the ion beam emittance stays the same for linear beam transformations, such as an ion beam drift or dipole magnet, but not for an acceleration stage.

A note on the unit of the emittance: In formula (23), the ellipse area (in units of mm · mrad) is divided by π. This means that the value of π is moved into the unit of the emittance, i.e. mm · mrad · π, as is commonly done (Conte & Mackay, 2008).

2.5 Bivariate Gaussian distribution

The phase space of an ion beam can be approximated as a bivariate Gaussian distribution, which assumes a Gaussian distribution of the beam intensity in x and x' for the x and y plane, respectively; An example is shown in Figure 8. The following function $g(x, x')$ represents the distribution's PDF, cf. (Nawri, 2019):

$$\begin{aligned} g(x,x') &= g_0 + g_{\mathsf{max}} \cdot e^{-(a\cdot(x-x_0)^2 + 2\cdot b\cdot(x-x_0)\cdot(x'-x'_0) + c\cdot(x'-x'_0)^2)} \\ a &= \frac{\cos(\theta)^2}{2\sigma_x^2} + \frac{\sin(\theta)^2}{2\sigma_{x'}^2} \\ b &= -\frac{\sin(2\theta)}{4\sigma_x^2} + \frac{\sin(2\theta)}{4\sigma_{x'}^2} \\ c &= \frac{\sin(\theta)^2}{2\sigma_x^2} + \frac{\cos(\theta)^2}{2\sigma_{x'}^2} \end{aligned} \tag{24}$$

In its interpretation as a PDF, the minimum value should be $g_0 = 0$ and $g(x, x')$ is normalised so that $\int_{-\infty}^{\infty} g(x, x') \mathrm{d}x \mathrm{d}x' = \frac{1}{g_{\mathsf{max}}}$.

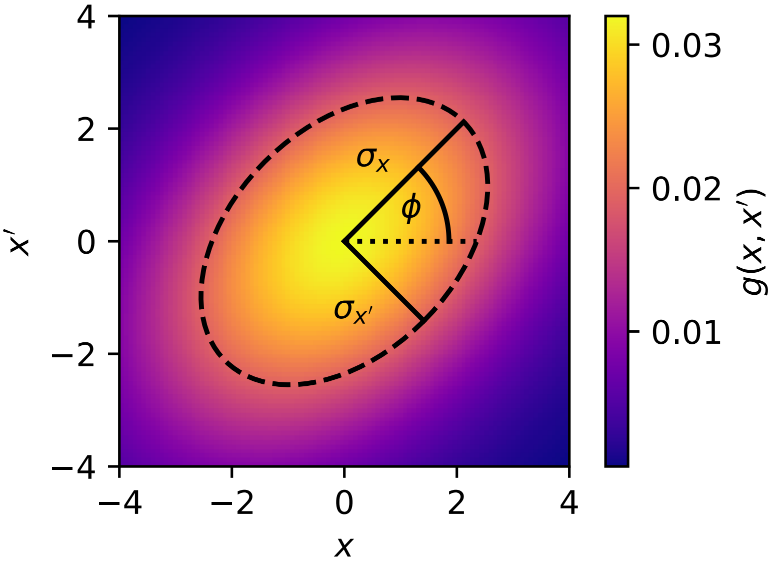

Figure 8: A bivariate Gaussian distribution, with the three key parameters being $\sigma_x = 3$, $\sigma_{x'} = 2$ and $\phi = 45°$. As a dotted line, the 1σ-ellipse is shown, and the intensity is normalised so that the integral over the entire space is one. The x and x' coordinates are shown dimensionless, but in the case of a phase space measurement would typically have the dimensions mm and mrad, respectively.

The values σ_x and $\sigma_{x'}$ represent the standard deviations from the mean in x and x' direction. The 1σ ellipse lies on these values, and thus the standard deviations correspond to the values a and b using the ellipse parametrisation in section 2.3.

3 Planning of the multi-beam switcher setup

The focus of this study lies on the bending magnet of the ILIAMS setup, seen in the top right corner of the VERA overview in Figure 1, and also shown in Figure 9.

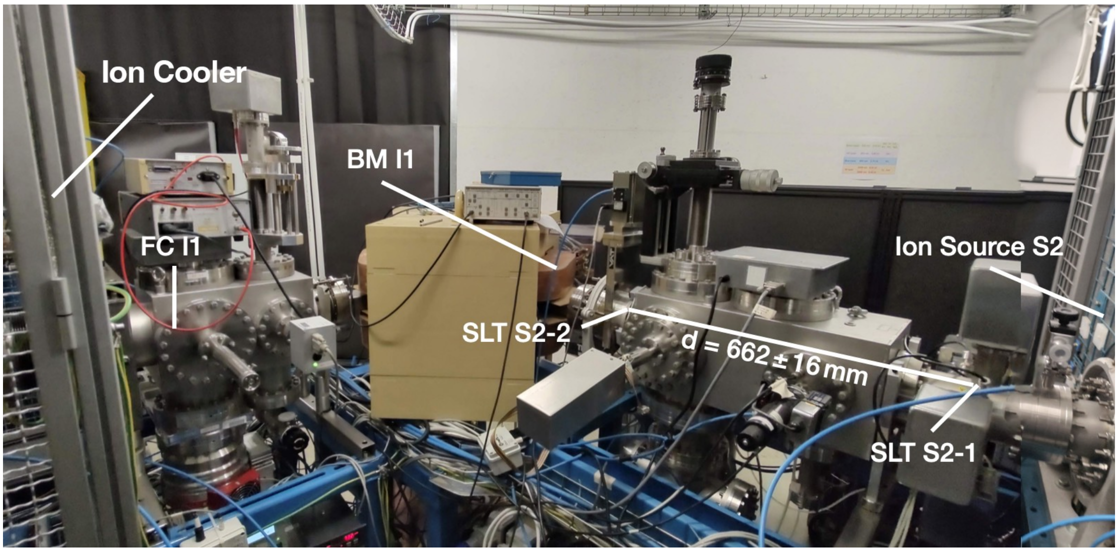

Figure 9: Picture of the injector beamline in front of ILIAMS. Note the indicated distance between the slitpairs `SLT S2-1` and `SLT S2-2`: The x slit distance is 646 mm and thus shorter than the y slit distance of 678 mm, as indicated by the uncertainty.

As compared to the accelerator injection magnet seen on the left of the VERA overview in Figure 1, it used to not have multi-beam switching capabilities. This functionality would be useful for the operation of the ILIAMS isobar separation setup because sequential injection of different masses is necessary to sensitively measure isotopic ratios. As the current coming from the ion source must not necessarily be very stable, frequent switching between isotopes is desired for AMS measurements, where a radioisotope-to-stable-isotope ratio is measured. For ILIAMS, the switching speed was previously on the order of several to hundreds of seconds, while for the other ion source at VERA, it can be less than a millisecond. As explained in section 1.1, changing the magnetic field takes some time, so a better way to do it fast is with the electric field of a multi-beam switcher, increasing the precision of the measurement.

Also, it is possible to further characterise the cooler with an MBS. By sequentially injecting two different isotopes of similar mass, their residence time in the cooler can be measured under steady-state conditions, which relates to the cooler function and physics. These measurements are presented in section 7.

Creating the electric field needed for bouncing is simply done by applying a voltage to the vacuum chamber inside the magnet, after electrically insulating it from the rest of the beamline. Thus, the magnet chamber acts as an electrode and a potential gradient towards the magnet chamber is seen by the ions and they are accelerated, leading to a different bending radius. Despite the simplicity of this principle, there were several difficulties in modifying an existing magnet in such a way.

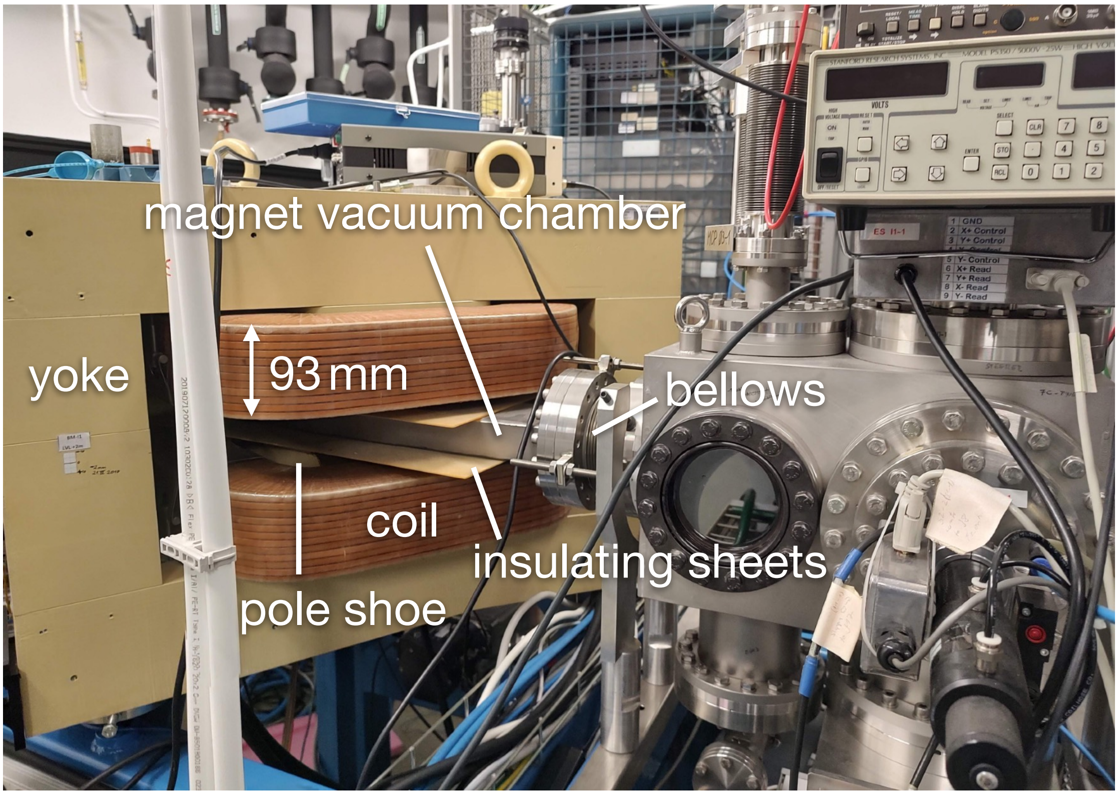

Figure 10: Essential parts of the bending magnet, as seen from the exit side.

First, the magnet chamber has a rectangular cross-section, as seen in Figure 10. Compared to a cylindrical profile, this allows for a smaller gap between the pole shoes of 50 mm and thus a higher field at the same coil current, and is not problematic for a normally grounded chamber. However, the ion optical characteristics of an electrode of this shape at the field boundary are not optimal, as there is no cylindrical symmetry. A solution to this is to attach a cylindrical protrusion to the ends of the chamber, that reaches either into the chamber or into the bellows directly attached to it. The shape of this electrode was determined by ion optical simulations using the software SIMION 8.1 (Manura & Dahl, 2011), which are covered in section 5.

A constraint to the design of these electrodes was the available space before and after the magnet. There were two bellows directly attached to the magnet, which occupy a length of $l = 85\,\mathrm{mm}$ each including the CF100 flanges. Before and after them are a vacuum gate valve and a slitpair, respectively, which means that the protrusion could only have a length of l, if it extended towards the outside of the magnet chamber (which it does, simulations concluded).

Also, the insulator between the magnet chamber and the grounded beamline had to fit in the 85 mm gap along with the bellows. Commercially available ceramic insulators with CF100 flanges are of greater length, so the only viable option was to manufacture an insulator with a CF-like interface to directly attach between the magnet chamber and bellows with rubber seals, ideally holding a vacuum of $\sim 10^{-7}$ mbar. An adequate material is polyether ether ketone (PEEK), as it is easy to process, highly durable and frequently used in high vacuum applications (Direct Plastics, 2013) (Sammartano et al., 2020). A length of some cm allows for enough insulation, the challenge was whether the vacuum seal would hold, which, as it turned out, was fulfilled by a finely sanded surface and well-manufactured CF knife-edge which presses into the rubber seal.

The 85 mm length constraint only holds if the magnet and source are not moved to allow for more space. This was considered, as there might have been an ion optical advantage to change the length of the drift sections between source and magnet, as well as magnet and cooler, as suggested by (Moreau, 2016) and (Wasserburger, 2018). As can be seen in Figure 1, directly next to the magnet is the laser table for ILIAMS, which is close to the wall of the room and can thus only be moved by some decimeters for safety reasons, so the amount of change in drift space that could be achieved is less than one meter. To decide on whether to move the assembly, the ion optics of the accelerator between the ion source and ILIAMS cooler were simulated as part of this thesis. To accurately assess the actual situation, phase space measurements of the beam coming from the source had to be done, which are described in the following section.

4 Phase space measurements of the ion beam

To get realistic ion beam data to use in simulations, the phase space of the ion beam out of the second ion source (S2) needed to be characterised. Phase space measurements of this beamline were performed before (Wasserburger, 2018), which are shown in section 4.2. However, to get a more systematic picture, several phase space measurements of different ion beams from the ion source were conducted in addition. This was done using two x/y slitpairs and a Faraday cup, a method also described in (Hinterberger, 2008). In the following short section, an overview of the method and specifics of the VERA setup is given. Figures and formulas show the process for the x direction, but they apply analogously for the y direction.

4.1 Method

The setup used to measure the ion beam's phase space is shown in Figure 11. Two slits in series are moved independently, to map out parts of the beam one after the other. For each combination of slit positions, the beam current is measured with a Faraday cup behind the second slit. This current can then be plotted in a 2D graph, with the x coordinate corresponding to the position of slit 1, the x' coordinate proportional to the position of slit 2 relative to slit 1, and the current as z data. The following equations are used to express the coordinates, using s_1 and s_2 for the position of the slits, and

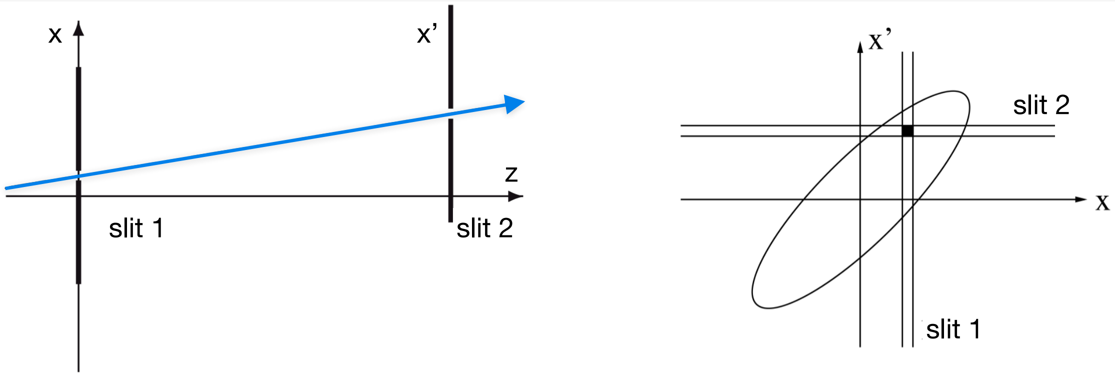

Figure 11: The two-slit setup that was used for phase space measurements. The absolute position of slit 1 is used as the x coordinate. The position of slit 2 relative to slit 1 is proportional to the x' coordinate. The beam current at (x, x') is measured with a Faraday cup behind slit 2. This process also applies to the y direction. From (Hinterberger, 2008) with slight modifications.

d for their distance:

$$x = s_1 \tag{25}$$

$$x' \approx \tan(\alpha) = \frac{s_2 - s_1}{d} \tag{26}$$

The x' coordinate normally corresponds to the angle rather than the positional deviation, however for the small angles in the order of some mrad, which are used here, $\tan(\alpha) \approx \alpha$. The coordinate x is often expressed in mm, while x' is expressed in mrad.

Once the data is collected, one can plot the intensity values as a heatmap in an x - x' coordinate system. Assuming a Gaussian distribution of the ion beam's phase space, the data can be fitted using a bivariate Gaussian distribution as shown in section 2.5. The fit values directly correspond to the parameters of the 1σ ellipse, which will be used subsequently to characterise the phase space, as shown in section 2.5.

In Figure 12, the calculation of the waist position relative to the measurement point is shown. The further away the waist is from the measurement point, the more the ellipse is sheared to the right. Thus, the important points are the maximum deflection angle x'_{max} and its corresponding distance to the optical axis $x(x'_{\text{max}})$. The distance between the beam waist and the measurement point is thus

$$d = \frac{x(x'_{\text{max}})}{\tan(x'_{\text{max}})} \tag{27}$$

Details on how to calculate this value analytically from the fit parameters a and b (half axes of the 1σ ellipse) are given on page 102 in the Appendix.

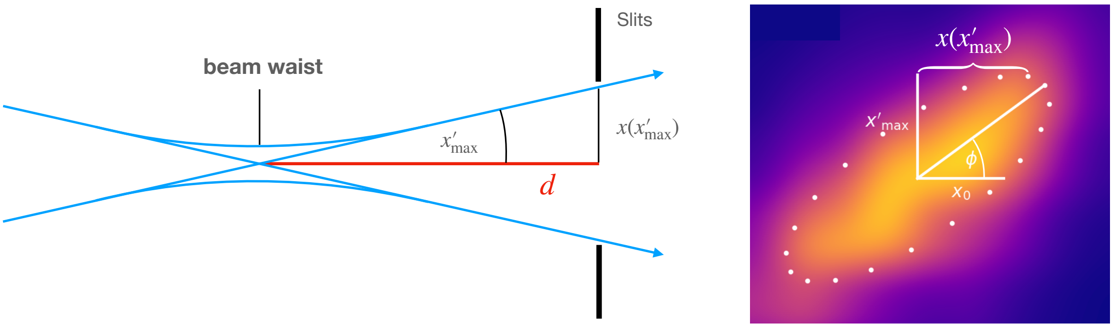

Figure 12: Calculating the beam waist position d from measured phase space data. The value x'_{max} refers to the maximum deflection angle (height of the ellipse), and $x(x'_{\text{max}})$ to the corresponding distance to the optical axis. If the phase space was measured at the waist position, the latter would be zero, i.e. the ellipse would be upright, thus $d = 0$. In the phase space diagram on the bottom right, note that the value $x(x'_{\text{max}})$ does not coincide with the point where the half-axis meets the ellipse.

4.2 Previous phase space measurements

The results of a phase space measurement of a carbon beam before the magnet, conducted by (Wasserburger, 2018), are shown in Figure 13. The measurement method is similar to the one previously described, however, only one edge of each slit was used to cut off the beam. Thus, the measured signal had to be numerically derived to gain the phase space distribution. This can lead to considerable uncertainty and is not favourable. As a consequence, the colourbar scale shown in Figure 13 is in arbitrary units. The beam current varied between 5.6 μA and 12 μA during the measurement, which leads to an additional uncertainty.

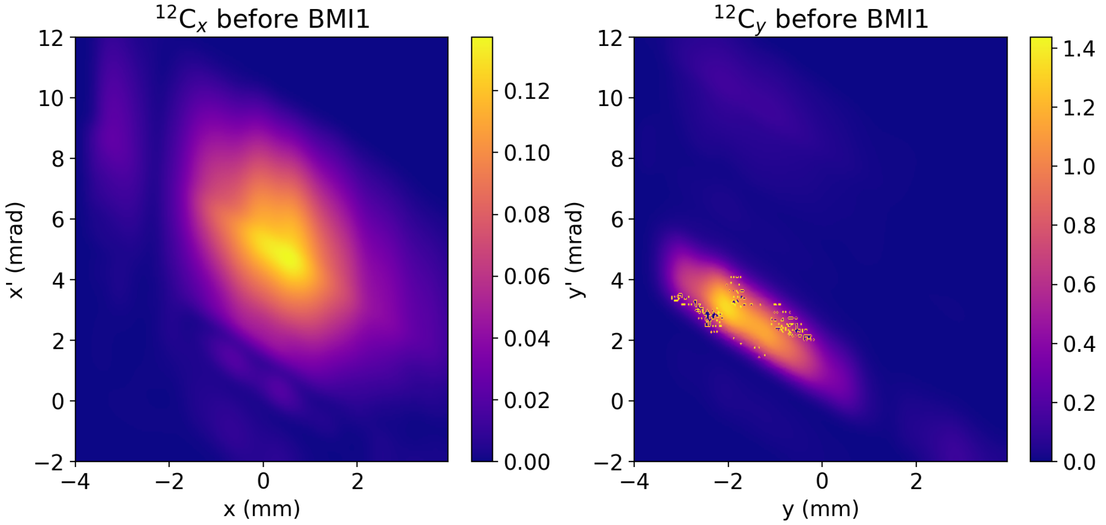

Figure 13: Phase space measurement of a carbon beam before the magnet, adapted from (Wasserburger, 2018). The white spots in the right plot are artefacts in the source publication. The measured data was interpolated by Wasserburger to give a smooth appearance.

The same measurement was repeated with caesium and hafnium beams, leading to similar results. Also, a measurement of the phase space after the magnet was conducted, however for two different targets and isotopes for each direction, see Figure 14. While a Hf beam was used for the y direction, there would be a considerable beam spread in x direction due to the various isotopes of Hf. Thus, a gold beam was used for the x direction, as it consists only of $^{197}\mathrm{Au}^-$ at that mass range. Although hafnium and gold have similar masses, the phase space could be element-specific, so the x and y measurements in Figure 14 are not necessarily compatible. The beam currents were measured to be around 0.7 μA at either start of the measurement.

Due to the inaccuracy of the measurement method, the possibility of dependence on the beam current, and to check other dependencies, it was decided to measure the phase space at S2 again.

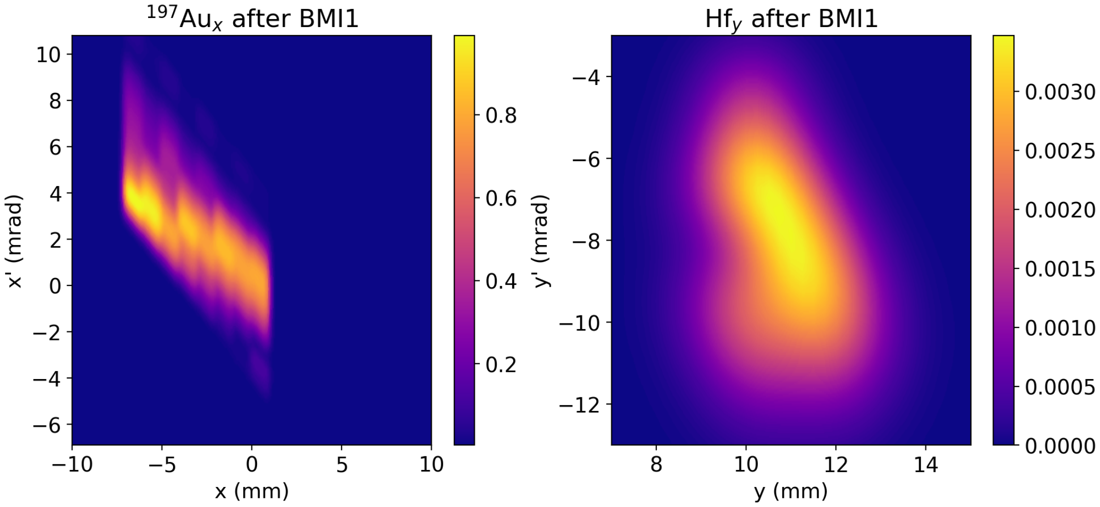

Figure 14: Phase space measurement of gold and hafnium beams after the magnet, adapted from (Wasserburger, 2018).

4.3 Application at VERA

To measure the phase space in front of the bending magnet `BM I-1`, slitpairs `SLT S2-1` and `SLT S2-2` were used in combination with Faraday cup `FC I1`. The setup can be seen in Figure 9.

The distance between the two slitpairs was measured as $d_x = 646\,\text{mm}$ and $d_y = 678\,\text{mm}$. For phase space measurements, the slit apertures (or widths of the slits) have to be sufficiently small so that the resulting image is detailed enough, but also large enough so that the current is still measurable after the magnet. For the first slit, that distance was determined to be 1.8 mm, and for the second slit as 0.6 mm. The first slit aperture width and position can't be controlled automatically, they have to be moved in a manual process. The speed is only about 0.4 mm/s. This is why only about 9 positions of `SLT S2-1` were used and justifies the bigger slit distance. However, two scripts were written to more directly control the slit distance and position, respectively, which are included on page 97 in the Appendix.

The slitpair `SLT S2-2` on the other hand can be controlled directly by entering desired values (or using the `scan` script), and thus more measurement points were used in combination with a smaller slit distance. Scanning the second slit for every desired position of `SLT S2-1` and measuring the current in `FC I1` gives the data for a phase space plot. This was commonly done with 48 measurement points for x' for every one of nine x positions, namely $-4, -3, \ldots, 4\,\text{mm}$.

The distance between the first slit `SLT S2-1`, i.e. the measurement point, and the nominal magnet edge is $3\,\rho_0 = 1050\,\mathrm{mm}$. Thus, one would expect ideal waist imaging by the magnet, if the beam waist is 350 mm after `SLT S2-1`.

In section 4.5, the results of these phase space measurements are shown.

4.4 Chemical target preparation

For the phase space measurements and for the measurement of ion residence times shown in section 7, targets had to be prepared chemically to sputter them in the SNICS. In comparison to AMS measurements, where one has to be very careful about cross-contamination and cleanliness, there was no actual AMS measurement or isotope counting to be done. However, in order not to cross-contaminate the lab, ion source or working materials, the lab rules for cross-contamination were obeyed.

For the carbon beam, this was done by taking a preprocessed graphite powder and pressing it into an aluminium cathode for sputtering.

In trial measurements of the phase space, a mixture of CaF_2 and PbF_2 was pressed into cathodes for creating and measuring a F^- and CaF_2^- beam, respectively. For the measurements presented in section 4.5, only PbF_2 was used.

For creating a Cl^- beam, the compound AgCl was synthesised from NaCl and $AgNO_3$ by the following reaction (Brumby, 2008):

$$\mathrm{AgNO_3 + NaCl \longrightarrow AgCl\downarrow + NaNO_3} \tag{28}$$

A 10:3 mixture (by weight) was dissolved in deionised water, centrifuged and the precipitated crystals were removed. The process was repeated two times to increase the precipitation yield. After a baking step of 3 h at 80 °C the crystals were crushed and pressed into cathodes. As AgCl decomposes under illumination, the exposure of the crystal to light had to be minimised.

4.5 Results of phase space measurements

The phase space measurement results are discussed here in detail. A more concise summary and conclusions can be found in the following section 4.6.

During trial measurements, the phase space from several targets at different currents was measured. However, the instability of the source current from any target over several hours was a major problem. Changing the order of first measuring x and then

y phase space did not lead to different results, however. In both cases, the y phase space was lower in intensity and emittance than for x, which could result from an inaccurate aperture width of the x and y slit, either for the first or second pair, which should be investigated further.

Another idea to overcome the source instabilities was to note the current draw of the source high voltage (HVS-CR) for the individual measurement runs and in some cases even for individual front slit positions within one measurement. Normalizing the measured current from the Faraday cup to the high-voltage current led to more reproducible results. Still, there were large variations of the phase space between different samples and source parameters, so a more systematic approach was adopted.

To correlate the effects of long sputtering with the resulting phase space measurements, some samples were measured both before and after being constantly sputtered for 5 h. The measurement schedule is shown in Table 1, and the target wheel after sputtering is shown in Figure 15. The measurement of one phase space (e.g. xx') took 30 minutes, leading to a total sample sputtering age of 7 h for the long-sputtered measurement runs.

Table 1: Measurement schedule for all targets, to correlate results with different measurement times. The order is from top to bottom, left to right. In the cells, the individual total output current (directly out of the source) is given.

			after 5 h sputtering			
	run 1 (μA)	run 2 (μA)	run 3 (μA)	run 4 (μA)	run 5 (μA)	run 6 (μA)
C target 1	50	14	50	15		
C target 2	50	14	50	15		
C target 3	50	14				
Old C target	50	14				
PbF_2 target 1					66	15
PbF_2 target 2					40	
PbF_2 target 3					15	

The results of several phase space measurements are shown in the subsequent figures, starting at Figure 16. The first measurement is that of $^{12}C^-$ out of a graphite target at moderately high beam current (around 50 μA directly out of source), taken during the first hour of sputtering. In Figure 16, the phase space measurement in x and y-direction is shown. This plot is also comparable to measurements at high beam current of three other carbon targets, two fresh and one old C target, which had not been sputtered a lot, shown in Figure 60 in the Appendix.

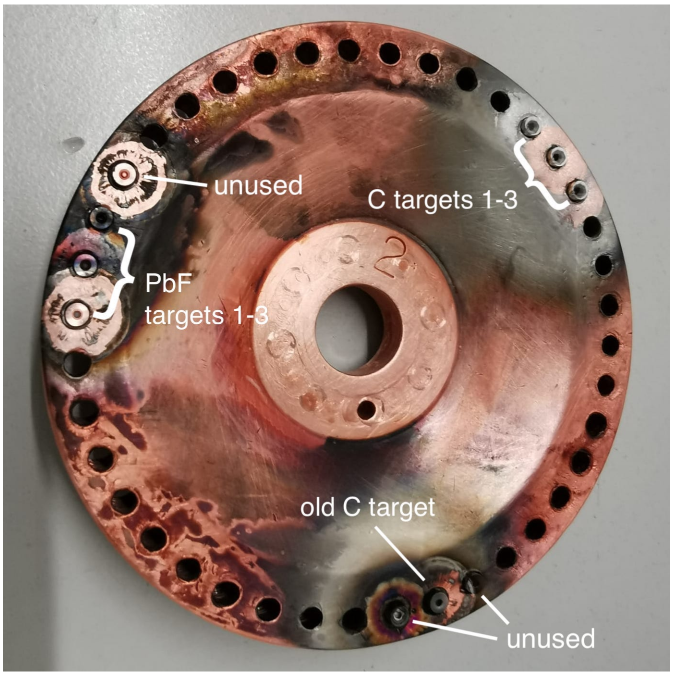

Figure 15: Target wheel after sputtering. Target numbering is anti-clockwise. The C targets were sputtered a lot (> 6 h), which can be seen as there are craters on the inner rim; A quite centred sputtering can be seen. The PbF_2 targets were not sputtered so much, and show a quite smooth target surface, except for the "unused" PbF_2 target, which is sputtered empty. The unused targets were used to tune the source parameters and as parking cathodes.

The current scale in the phase space plots can only be used for relative comparison because parts of the beam might be measured multiple times, as the slit distance is 1.8 mm but the measurement points are only 1 mm apart. This is a trade-off between precision and accuracy, but as the total current (before the magnet) is known, the more precise method used here is preferred.

One can approximate the phase space using the simple ellipse model discussed in section 2.3. The data is fitted using a bivariate Gaussian distribution, where the free parameters are mean position x and angle x', their variances σ_x and $\sigma_{x'}$ and the angle of the ellipse ϕ, measured counterclockwise from the x-axis. From the fitted data, the 1-σ ellipse, a simpler representation of the measured phase space, can be calculated. It contains 39.35 % of either the x- or y component of the beam and is indicated as the dotted line in Figure 16. Also shown is the emittance ϵ, representing the ellipse area and the position of the beam waist relative to the measurement point. The sign of the waist position is chosen such that a positive sign represents a waist downstream from the measurement point. From an ion optical standpoint, one would want the waist to be around $2\,\rho_0$ in front of the magnet entrance, i.e. at 350 mm after the measurement point.

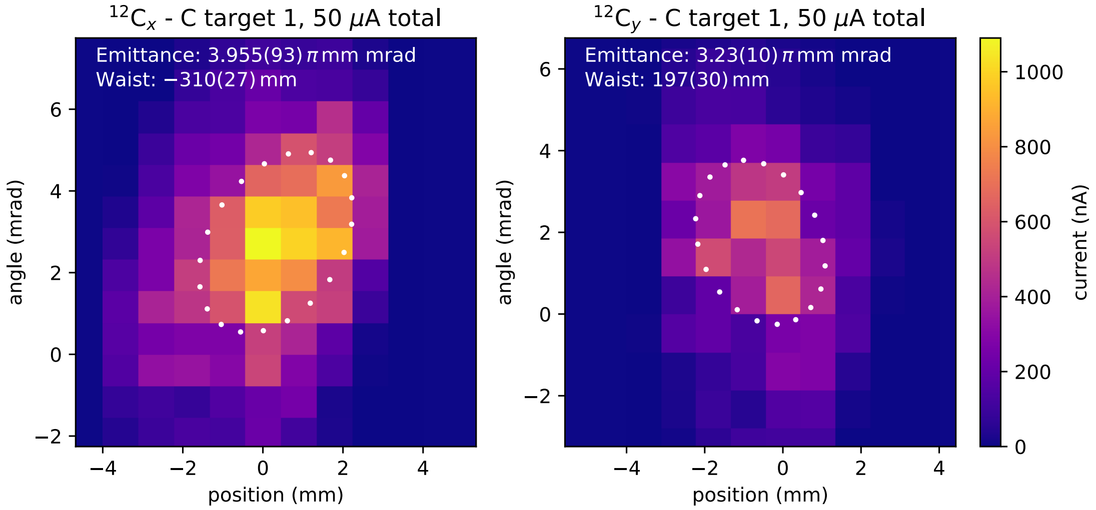

Figure 16: Phase space measurement of a high current $^{12}C^-$ beam coming from a fresh graphite target. The left plot shows the phase space in x direction, the right in y. A positive sign in the waist position indicates a waist downstream from the first slit position. Note that while the maximum current and emittance are comparable for x and y, the waist position of the beam has a different sign - the beam is thus highly astigmatic.

All other parameters important for ion optics, such as x_0 and x'_{max}, are given in figures 60 and following in the Appendix.

In Figure 16, the beam phase space is quantitatively similar in x and y direction, concerning the x and x' size of the ellipse and the emittance. Qualitatively however, they differ heavily, as the x waist is 310(27) mm before the measurement point, while the y waist is 197(30) mm **after** the measurement point. The beam is thus astigmatic, which is unusual as the setup before the measurement point has cylindrical symmetry.

The absolute value of x and x' is not relevant, as the beam can be steered using an x/y steerer in front of the BM and one after it.

Figure 17 shows the phase space measurement of a $^{12}C^-$ beam from a graphite target at a low current of about 14 µA. The emittance and peak beam current are lower than those of the high current measurement, but most obvious is the reduction in astigmatism. The waist position is still not aligned between the x and y direction, but now the difference is only 13 cm and the 1σ ellipses are almost upright, meaning the waist is near the measurement point. Again, this measurement was conducted on three different targets (two fresh and one old C), with similar results.

As a last test for carbon beams, the targets were measured after being sputtered for $\sim$ 6 hours at around 50 µA. In Figure 18, a high current beam of $\sim$ 50 µA shows a different behaviour than the beam from a fresh target. Now, the astigmatism is almost

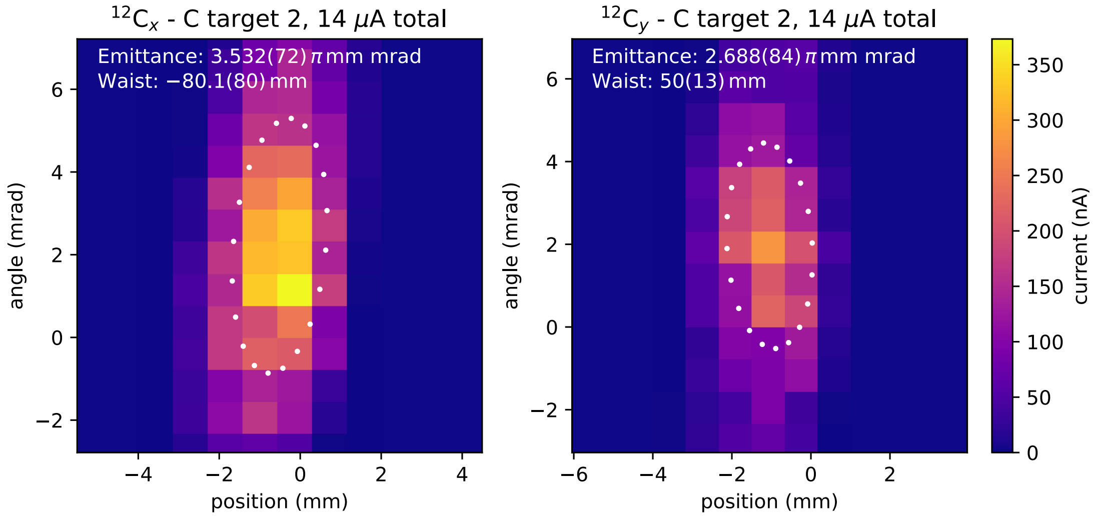

Figure 17: Phase space measurement of a low current ^{12}C$^-$ beam coming from a fresh graphite target. The left plot shows the phase space in x direction, the right in y. While the maximum current and emittance are somewhat comparable for x and y, the waist position of the beam has a different sign - the beam is thus slightly astigmatic.

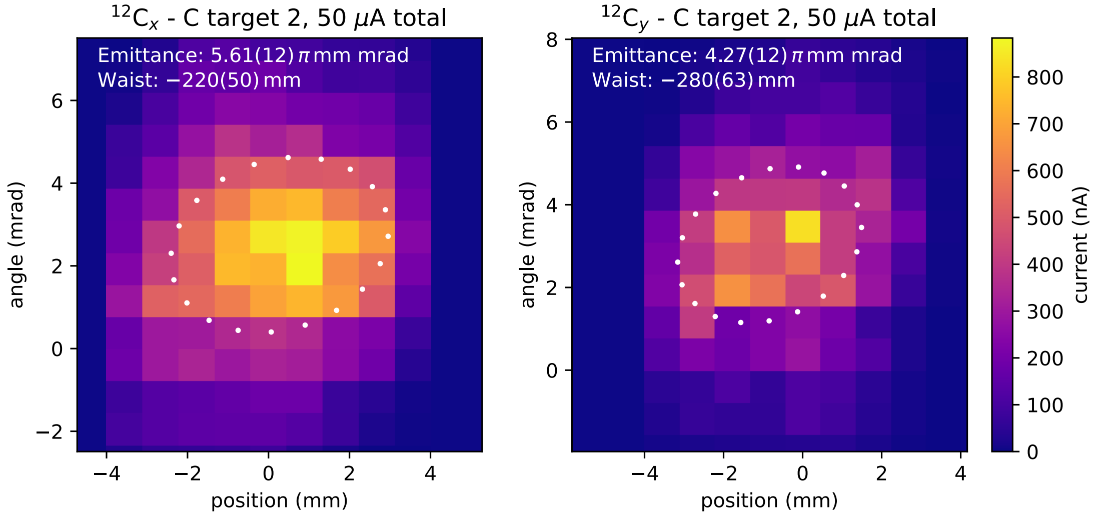

Figure 18: Phase space measurement of a high current ^{12}C$^-$ beam coming from a graphite target sputtered for ∼ 6 hours. The left plot shows the phase space in x direction, the right in y. The beam waist position in x and y direction align within an uncertainty of ±3 cm.

gone, and the x and y waists align up to ±3 cm. The waist position is $\sim$ 25 cm in front of the measurement position.

As measurements of fluorides are very frequent in the ILIAMS setup (Martschini et al., 2021), the behaviour of a $^{19}F^-$ beam from a PbF_2 target was also studied. The phase space of a high current beam of 66 µA is shown in Figure 19. It has a similar emittance as the carbon beam, which is expected at the same current. The beam is not astigmatic, as compared to $^{12}C^-$, and shows a waist around 90 cm before the slit position. This is the furthest away from the ideal waist position of 350 mm after the slit.

At lower currents of 15 µA, as shown in Figure 20, the waist moves away from the source towards the slitpairs, and the emittance decreases.

The measurements presented here show that the waist is in all cases further upstream than the ideal waist position of 350 mm. This mismatch could principally be solved by a focusing lens, which is installed between the source and the slitpair `SLT S2-1`.

4.6 Conclusions from phase space measurements

In general, the position of the beam waist is of importance, as the ion cooler injection aperture has a diameter of only 3 mm. To increase transmission into the cooler, most of the beam should fit through the aperture, ideally when a beam waist coincides with the aperture position. This in turn can only be achieved if the beam waist in x and y direction is aligned.

It was observed that the phase space for both $^{12}C^-$ and $^{19}F^-$ beams depends highly on the beam current and sputtering time of the target. For carbon, the fresh targets (especially at high beam current) give an astigmatic beam waist, i.e. the waist position in x and y directions is up to half a meter apart. After sputtering the carbon targets for several hours, this astigmatism was strongly reduced, and a behaviour more consistent with the fluorine beams was observed: For high currents, the beam waist is hundreds of millimetres upstream from the first slit position. By lowering the current, the waist moves closer towards the slit, at 15 µA it is some centimetres before the slit position.

Reasons for the change in phase space can include target cratering and caesium deposition on the target surface. The astigmatic behaviour of the beam however is unusual, as the geometry of the source and extraction is cylindrically symmetric. The sample wheel was centred before the measurement using optical inspection, but an eccentricity of the wheel could still be an explanation. However, as the astigmatism changes behaviour with time, this is unlikely to be the cause.

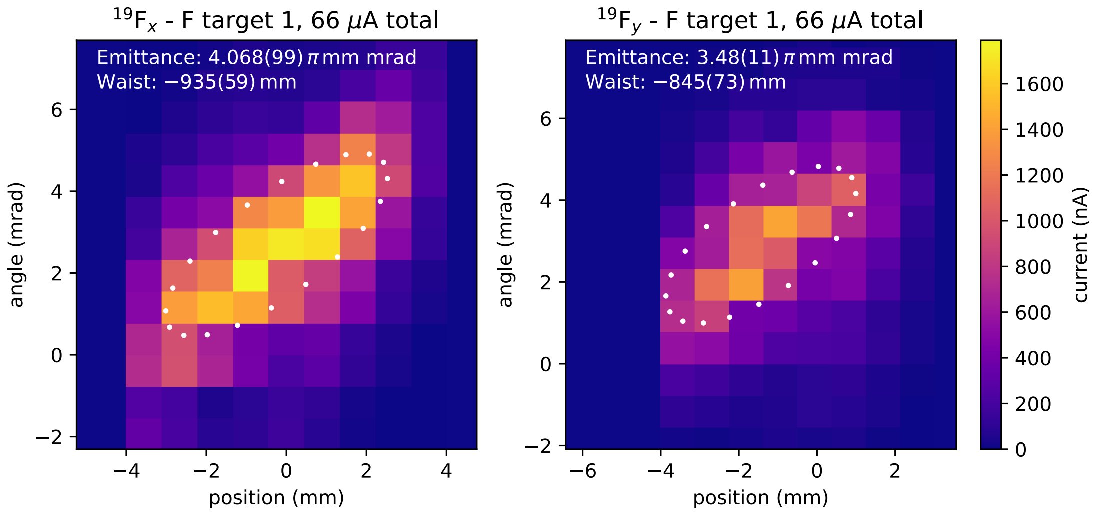

Figure 19: Phase space measurement of a high current $^{19}F^-$ beam coming from a fresh PbF_2 target. The left plot shows the phase space in x direction, the right in y. In comparison to $^{12}C^-$, the emittance is considerably larger, which is expected for fluorine. The beam waists align within an uncertainty of ± 5 cm.

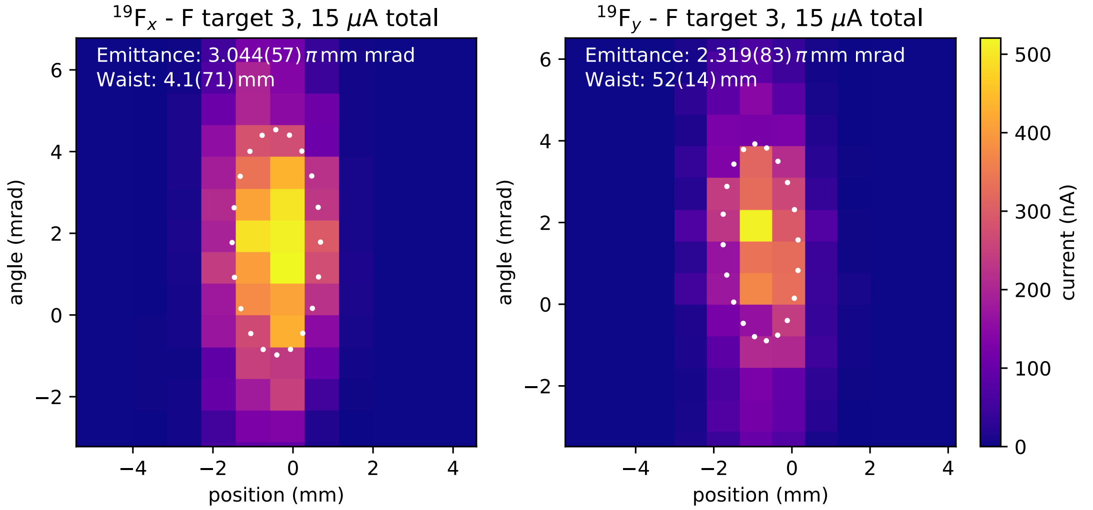

Figure 20: Phase space measurement of a low current $^{19}F^-$ beam coming from a fresh PbF_2 target. The left plot shows the phase space in x direction, the right in y. The emittance is comparable to the low current $^{12}C^-$ beam. The beam waists align within an uncertainty of ± 3 cm.

The movement of the waist position could principally be compensated by adjusting the voltage of the focusing lens directly behind the source. A negative voltage, to focus the diverging beam of negative ions, would be needed. This compensation however works only simultaneously for the x and y directions, so for the highly astigmatic beams from fresh carbon targets (and possibly for other elements), only a quadrupole focussing lens would be able to correct the waist position, which could increase the transmission into the cooler. This method is further explored in section 5.3.3.

5 Ion beam simulation

To aid in the design of the MBS, and to find solutions for losses during injection of ions into the cooler, ion beam simulations of the cooler injection beamline were conducted. They were based on the phase space measurements discussed in the previous section.

5.1 Simulation methods

Different simulation methods were employed for studying the ion optics of the cooler injection beamline, including SIMION, matrix calculation and a COMSOL simulation of the magnetic field.

SIMION 8.1.1.32 is a simulation software for ion optics, in which the path of ions moving through electric and magnetic fields can be calculated (Manura & Dahl, 2011). One can define the geometry of lenses, magnetic pole shoes etc. which are then converted by the program into voxelated potential arrays (PAs). SIMION can solve the Laplace equation inside the PAs and calculate ion trajectories numerically, based on initial ion parameters given to the software. A Python code was written to generate ions in the `.ION` format required by SIMION, based on the phase space measurements presented in the previous section.

5.1.1 General setup of SIMION simulation

The general area of interest is the ILIAMS injection beamline, extending from the ion source to the cooler, which can be seen in Figure 21.

While the positions and shapes of additional electrodes were changed between simulations, the general setup did not: The simulated flight path extends from the position of the first slitpair `SLT S2-1` to the cooler injection aperture, with an x/y steerer, the bending magnet with the insulated chamber, an x/y slitpair and the injection lens in-between. The ion starting point is the measurement point of the phase space, allowing for realistic ion beams in the simulation. The transmission is always given as the number of ions that enter the cooler entrance aperture, compared to the number at the start. It is comparable to the transmission from the Faraday cup `FC I1` into the cooler, which is not measurable, as only the current behind the cooler can be measured, not the one entering it. This is an important remark, as the transmission defined here tells one how much current is already lost at the cooler injection, which is either due to a too big ion beam, or mismatched ion optics in front of the cooler.

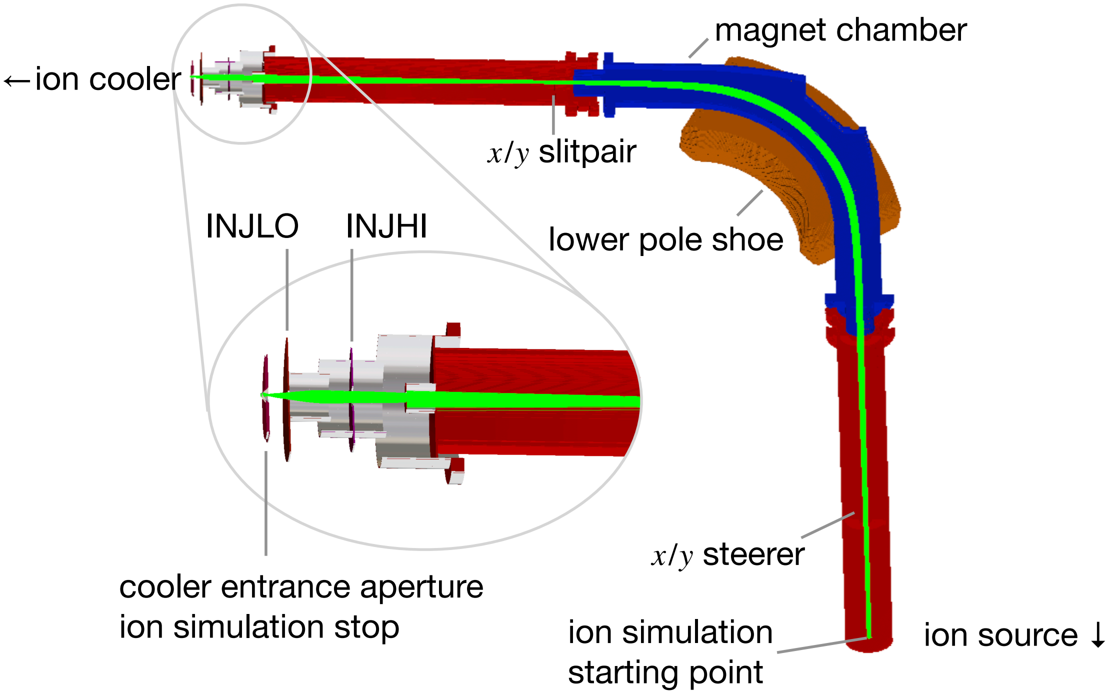

Figure 21: SIMION simulation overview of the ILIAMS injection beamline, created with SIMION 8.1.3.9 early access.

The simulation should thus be capable of identifying and analyzing ion optical flaws in the cooler injection beamline.

The magnetic flux density of the BM was first calculated using Formula (1). SIMION assumes a constant magnetic flux density at the boundaries of the pole shoes, which translates to roughly the same value inside the BM. However, as the pole shoes don't contain the whole curved flight path, and as fringe effects exist, the flux density can vary from the theoretical value. It was optimised for transmission into the cooler to a precision of 0.05 G. Similarly, the magnet chamber voltage was calculated first by equation (6), but then scanned for optimal transmission, with a precision of 1 V. The final values are shown in Table 2.

Table 2: Flux densities and MBS potentials used in the SIMION simulations. For the lower row, the MBS is set to "1 amu down", which is defined in section 1.1.4.

ion mass in amu	12	19
BM flux density (G) (for $U_{\text{MBS}} = 0\,\text{V}$)	−2439.15	−3069.20
BM flux density (G)	−2538.75	−3149.00
MBS voltage (V)	2500	1579

The cooler injection lenses are named (in beam direction) INJHI, INJLO and INJ.AP, as can be seen in Figure 21. Typical voltages, relative to the cooler potential, are

5000 V, 1270 V and 60 V, respectively. These values were also scanned to find optimal transmission into the cooler. The optimal values found lie on the upper boundary of what is possible with the installed power supplies, and amount to 10 000 V and 1310 V for INJHI and INJLO, respectively. INJ.AP was kept constant, as it corresponds to the cooler injection energy. One could argue that it would be more realistic to apply the commonly used values, but in an AMS measurement, these voltages are also scanned for the highest transmission, so the same approach was adopted for the simulations.

This simulation differs from previous ones by (Moreau, 2016) or (Wasserburger, 2018), in that the cooler itself was not simulated, because the main focus here is the injection into the cooler.

For defining the ions, two methods were used: First, a statistical distribution of ions according to the fitted phase space measurements could be generated. For this so-called "random method", the fit parameters σ_x, $\sigma_{x'}$ and ϕ_x were used to define a bivariate Gaussian distribution of the x component (and analogously for y), as described in section 2.5. To get relevant statistics, around 10000 ions were generated this way, which slowed down the simulation speed significantly, as compared to the next method.

Another method of defining ions ("1σ method"), based on the same phase space fit data, was thus devised. The idea is the following: Ions that are on the 1σ ellipse stay there, which can be illustrated when looking at Figure 7 and imagining a drift movement of the ion beam. The ion with parameter x_0 just flies parallel to the optical axis, which means it will keep its position on the ellipse indefinitely. On the other hand, the ion with parameter x'_{max} will keep its high x' value and stay on top of the ellipse, even though it will shift to the right along with the ellipse. Likewise, all ions on the ellipse are sheared clockwise, meaning it is sufficient to define ions along the 1σ ellipse as a proxy for the whole beam.

The only problem is that the coordinates of the ions in the x and y directions will be correlated, which is not necessarily the case in reality. This has the effect that when looking at a cross-section of the beam, the ions lie on an ellipse as well (not the phase ellipse, but rather a beam profile). This ellipse will be rotated or sheared as well under linear beam transformations, which is not representative of the actual beam profile evolution. However, the real beam profile can be obtained by just taking the width of the beam profile (meaning x_{max} and y_{max}) and defining a new ellipse with $\phi = 0$.

For most simulations conducted for this thesis, the 1σ method with 20 ions along the phase ellipses was used, which was a good trade-off between accuracy and simulation speed. The transmission was then calculated by a Monte Carlo integration, which is described in section 5.2.1.

The x/y slitpair after the magnet chamber was only used once to investigate any ion optical effect it might have, which is discussed later.

5.1.2 Batch-running using Python

For batch running simulations, i.e. repeating simulations with different parameters, SIMION gives the possibility to do that inside a Lua script. However, the desired calculations after the simulation (like calculating the transmission by a Monte Carlo integration, see section 5.2.1) were more complex than the Lua scripts invoked by SIMION could handle. Thus, a method for batch-running simulations by a Python script was devised. This is essentially done by invoking the command-line version of SIMION in Python:

```
%simion.exe --nogui fly --adjustable l1=0 --particles=12C.ion wb.iob
```

Here, the SIMION command `fly` is called for the workbench `wb.iob`, along with a voltage for the first injection lens `l1`, as well as the file containing the particle definitions. This allows for sequential variation of these and similar parameters in a `for` loop, and thus batch-running SIMION simulations.

A special version of PAs, called fast adjust PAs, can as well be refined, i.e. given a different potential, from the command line, via:

```
%simion.exe --nogui fastadj Polschuh.PA0 1=3500
```

This sets the magnetic flux density at the pole shoe boundary to 3500 G, and can also be included in the `for` loop for batch running at different potentials.

5.1.3 Matrix calculation

A Python code to calculate simple matrix operations on vectorised beam parameters (cf. section 2) was written to compare to the SIMION simulations. Only first-order effects are considered, so it is expected to see a deviation for the magnetic fringe field.

5.1.4 COMSOL simulated magnetic field

To give a third estimate of the ion optical effect of the magnet, its magnetic field was simulated with the software COMSOL Multiphysics® 6.0 (COMSOL AB, 2021). The software employs the finite element method to solve physical equations for a defined geometry as well as boundary conditions. To do so, the current through the coils was simulated, and the effect of pole shoes, yoke and magnet vacuum chamber was included.

First, the 3D geometry had to be simplified, so that only a few vertices are left per part. However, the simplified parts are still accurate within some millimetres of the original parts. The resulting `.stl` files were then imported into COMSOL, where the conductor properties like coil windings (144 for each coil), conducting cross-section ($32.2373\,\mathrm{mm}^2$) and conductivity (copper: $6 \times 10^7\,\mathrm{S/m}$) were specified (Danfysik A/S, 2015) (aviva metals, 2023).

Next, a current of 43.3426 A was sent through the conductors, creating a magnetic field of 3128 G within the pole shoes, considering only the y direction of the field, as other directions are negligible for this application. This value can be verified using equation (2) and the data of the dipole magnet shown in section 3, which yields the same number for B.

A plot of the geometry and the resulting magnetic field is shown in Figure 22. The resulting magnetic flux density was exported as a `.csv` file and consequently imported into SIMION. As the maximum field and the current are proportional (disregarding hysteresis), the resulting field can be scaled with a multiplicative factor to achieve the desired field.

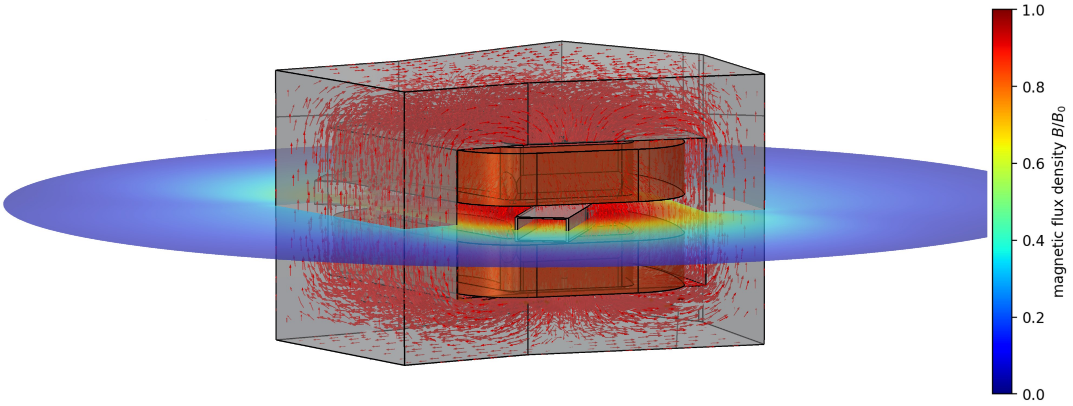

Figure 22: COMSOL simulation of the dipole magnet. Shown are the elements that contribute to the magnetic field: coils, yoke, pole shoes and vacuum chamber. The arrows in the yoke and between the coils indicate the strength and direction of the magnetic field. The colorbar indicates the magnetic flux density norm, relative to the maximum field. A perpendicular projection of the flux density is also shown in Figure 33.

The import into SIMION requires some preprocessing, as the function `field_array` accepts only files of a certain size and expects a certain header, which is well described in a SIMION user forum thread (Schillaci et al., 2017). The `.csv` file from COMSOL had to be cut into two perpendicular parts along the beamline, overlapping inside the BM, allowing for a smaller overall size yet 1 mm resolution.

5.2 Evaluation of simulation

During the `fly` command execution, every ion's three-dimensional position $\vec{x}$ and velocity $\vec{v}$ are recorded and stored in a `.csv` file. This was defined in the workbench's corresponding Lua script. In a simple version of the script, only $\vec{x}$ and $\vec{v}$ at the very beginning and end of the wanted trajectory are recorded, which is done by defining two planes perpendicular to the trajectory (the z-direction) at the respective positions, via the `testplanelib.lua` library in SIMION. This allows for a very simple analysis of transmission by counting the ions that reached the aperture at the end.

In a more advanced version of the Lua script, the parameters $\vec{x}$ and $\vec{v}$ are recorded on many z-planes along the whole flight, allowing for each ion's path to be tracked. This allows for investigation of the beam envelope, which is considered here as the evolution of x_{max} and y_{max} of the beam in z direction.

5.2.1 Transmission calculation

In the case of the random method of ion generation, the number of ions reaching the aperture was counted and used for the transmission calculation.

For the 1σ method, the ellipse parameters of the ions at the cooler injection aperture position were used to define a bivariate Gaussian distribution. This probability density function was then integrated over the whole area of the aperture. A numerical Monte Carlo integration was used to find the volume under the PDF within the aperture. Essentially, points on the aperture plane were created randomly according to the PDF, and the transmission is then calculated by the number of points that are located within a centred circle of 3 mm diameter, reflecting the size of the aperture. This procedure is in a way similar to the first method but allows for a more granular resolution of the transmission: As the Monte Carlo Simulation can easily be done with millions of points, the calculated value is more precise than when only counting 10000 ions (which is already quite time-consuming in the SIMION simulation).

However, this method works best only if all or most of the 20 ions' positions are recorded on the aperture plane. If not, the least-squares fit of an ellipse is possibly erroneous, and the random method with 10000 ions should be used. Also, if there is a loss of ions due to an aperture before the injection aperture, the beam is collimated. This can not be recreated by the 1σ method, where all ions lie closer to the optical axis. So for highly divergent beams, also the random method should be used.

In the case of the simulations using the COMSOL calculated field, a high divergence beam was used and the ellipse fits were not as reliable as the random method. Thus, the latter was used for all COMSOL simulations and other simulations that were directly compared to those.

5.2.2 Beam envelope

The envelope of a beam can be defined as the evolution of the 1σ width along the flight path, namely x_{max} and y_{max}. This is easily obtained as the coordinate-wise maximum deviation of all particles of the 1σ ellipse from the mean position of particles within one z plane. The envelope can then be plotted for the whole trajectory, with the bent section flattened out.

5.3 Results of simulations

First, the results of design variations of the protrusion electrode are shown, after which the ion optics of the ILIAMS injection system as a whole are discussed. In general, multiple measurements of the phase space (see section 4.5) were used for the simulation, to account for the different beams used in operation. The most used ones were a low current fluorine beam (see Figure 20), and high current carbon beams, namely the fresh (see figures 16) and long sputtered targets (Figure 18). The reason for choosing them was that the high-current carbon beams were found to have the lowest transmission in simulations, while the low-current fluorine beam had the highest transmission. This way, the effects of both low and high transmission beams could be studied.

5.3.1 Protrusion electrode design

Several parameters of the electrode design were investigated to find optimal transmission through the cooler aperture. The idea behind this electrode is to create a cylindrically symmetric electric field transient between the magnet chamber and the rest of the beamline. The former has a rectangular cross-section, which is likely to produce unwanted ion optical effects. Thus, a protruding cylinder attached to the magnet chamber and extending away from it was conceived. The final design of the MBS entrance electrode is shown in Figure 23.

The first question is whether a protruding electrode is actually needed to get acceptable transmission. In Figure 24, the transmission at different lengths of the cylindrical

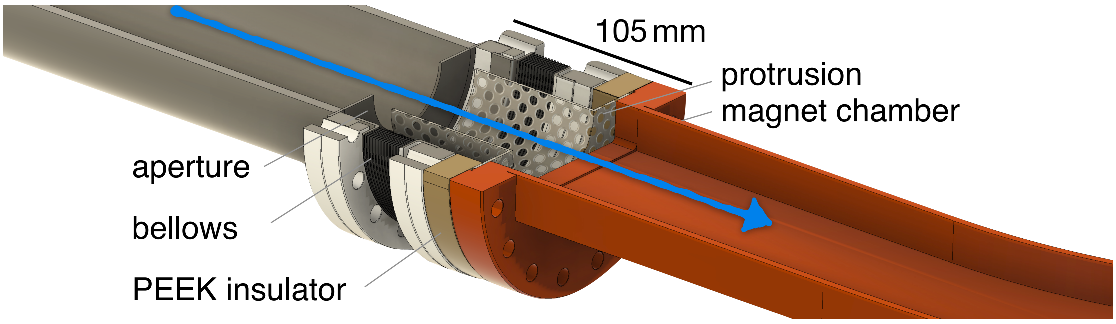

Figure 23: 3D render of the planned MBS entrance electrode.

electrode extending from the rectangular magnet chamber is shown. The MBS was used to bend the wanted mass “1 amu down”, as explained in section 1.1. As dotted lines, the nominal transmission, i.e. without using the MBS, just the magnet, is plotted as a benchmark value. At length zero, meaning that no electrode is installed at all, the transmission is significantly reduced by up to 50 % as compared to the nominal value, which justifies the need for a cylindrical electrode. As the length is extended, the transmission approaches the nominal value. An electrode longer than 70 mm would not have fit into the empty space of the beamline, but at that length, the relative transmission is $> 98.3\,\%$ of the nominal value. This was deemed high enough, so 70 mm was chosen as the final length.

Still, the protrusion could reach in the other direction (into the magnet chamber), but this would also lead to a non-cylindrical field transient. A simulation of this showed similar transmission results as when using no protrusion, so this idea was discarded.

The other protrusion parameter, its diameter, was also varied to find good transmission. Changing the diameter from 70 to 40 mm resulted in a transmission reduction between only .1 and 4 %, depending on the phase space used for the simulation. The value chosen was 60 mm, to allow enough space between the protrusion and the surrounding bellows.

One additional part to consider is an aperture for the front protrusion, so that stray ions can’t enter the tubular space between protrusion and bellows and hit the insulator. This could lead to a charge buildup on the inner insulator surface, which could in turn induce undesired steering effects and eventually lead to the breakdown of electrical insulation. Thus, an aperture to geometrically shield the tubular space is needed. Its placement and hole diameter were varied to yield optimal transmission, but only marginal transmission variations were observed. The final diameter chosen for this design is 50 mm, which is small enough to shield the insulator, and big enough to let at least $10\,\sigma$ of a centred beam through. The aperture is located between the

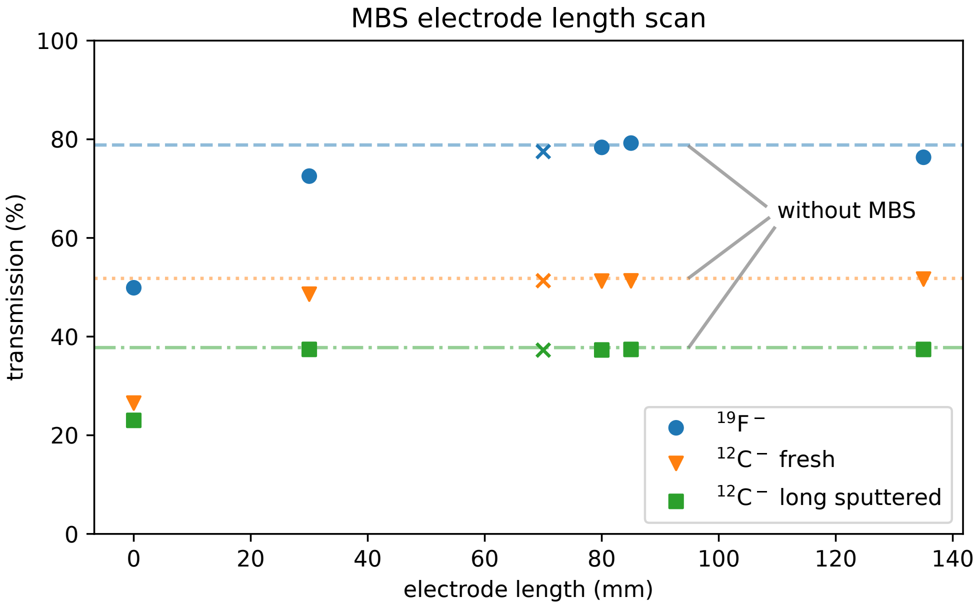

Figure 24: Transmission through the cooler injection aperture for different MBS electrode lengths and phase spaces. The dotted lines show a benchmark, the achieved transmission without using the MBS. As the electrode length increases, the transmission with MBS approaches the benchmark value. The final value used for construction is marked with an x. The flux densities and chamber voltages used for the simulation are given in Table 2.

CF flanges of the vacuum gate valve and bellows, so its distance to the protrusion electrode is 15 mm. This defines the region of the electric field gradient, in which the ion beam accelerates towards the magnet chamber. It is big enough to account for manufacturing margins.

As the bellows sit between the electrode and aperture, these parts are not necessarily concentric. A simulation of a ±5 mm off-centring resulted only in a minor relative transmission reduction of $< 0.2\,\%$, so the effect is negligible.

Finally, the effect of the x/y slitpair directly behind the exit bellows was investigated, as it could have an ion optical effect. However, even at a distance of 1.8 mm, which is smaller than normally used, the relative transmission reduction is $< 0.3\,\%$.[1]

To illustrate the electric potential difference created by the entry and exit electrodes, and show the path of the ions flying through them, Figure 25 shows a potential energy view of the magnet chamber entrance and exit.

---

[1] This slitpair was removed from the beamline during MBS construction, however, it could be reinstalled with no ion optical effect on the MBS operation.

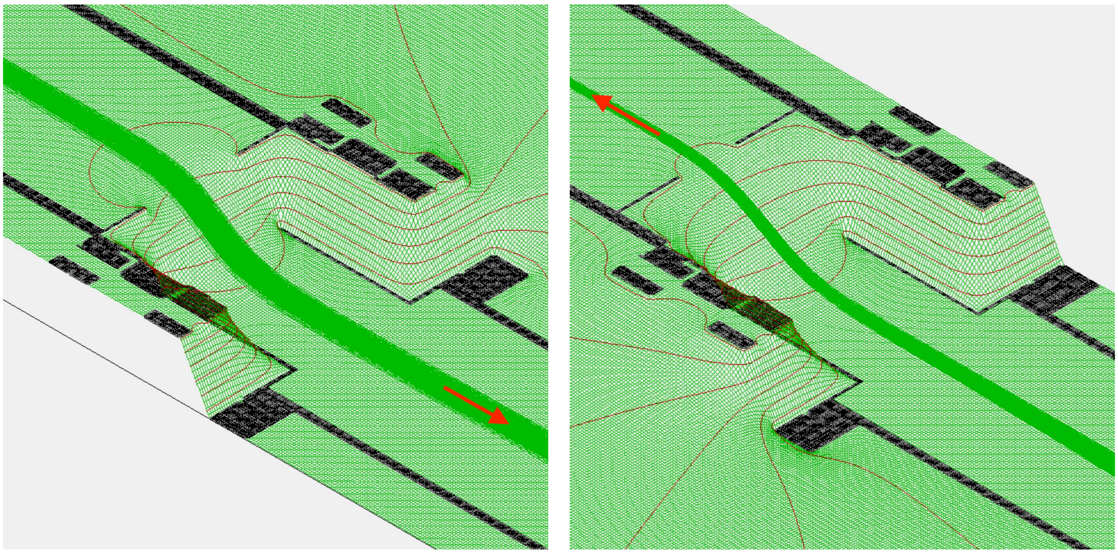

(a) entry electrode (b) exit electrode

Figure 25: Potential energy view of entrance and exit electrodes. In Figure a), $^{12}C^-$ ions enter from the left and get accelerated towards the chamber by a 1000 V potential difference. In Figure b), the ions enter from the right side and get decelerated upon exit of the magnet chamber. The leftmost equipotential line represents 1 % of the full potential. It penetrates not as far into the exit beamline, as the x/y slitpairs are set to 35 mm distance in this example, compared to the 50 mm aperture in front of the entry electrode.

5.3.2 Transmission comparison of SIMION and COMSOL simulations

A comparison of the transmission as simulated purely by SIMION and using the COMSOL-calculated field was conducted. To do so, ion beams with $x_0 = 1.5$ mm and $x'_{\text{max}} = 4$ mrad (and analogously for y) were started at different positions before the magnet, and the transmission was counted using 10000 ions. To steer the beam for optimal transmission, an optical inspection (by eye) of the trajectories plotted in SIMION and the subsequent shifting of parameters was done. Interestingly, for COMSOL the ion beam pointed a little in the negative y direction after the magnet, which was countered by starting the ions 2.75 mm further in y. As the COMSOL simulation space was kept very tight in y direction due to file size limitations, there was some ion loss (up to 5 %) at long waist distances, as ions started further away from the magnet reach a higher y position, and exit the space where the B field was simulated. This effect is artificial, thus the transmission for the simulations with the COMSOL-calculated field is counted relative to the number of ions exiting the magnet (instead of all simulated ions).

In Figure 26, the transmission of different ion beams is shown depending on their waist position before the magnet edge. As can be seen, the transmission values are loosely correlated, with the COMSOL-calculated values mostly above the SIMION results.

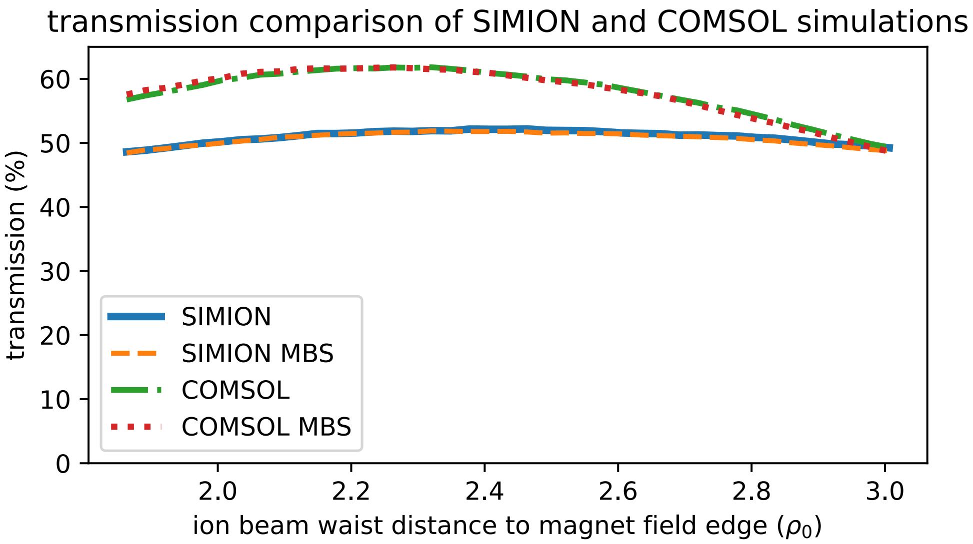

Figure 26: Transmission comparison for ion beams with different waist positions before the magnet edge, shown in units of $\rho_0 = 350$ mm. The flux density and voltage values used are given in Table 2. The beam values were $x_0 = 1.5$ mm and $x'_{\text{max}} = 4$ mrad (and analogously for y). The maximum in transmission lies at 2.4 ρ_0 and 2.3 ρ_0 for SIMION and COMSOL simulations, respectively. The first slit position is 3 ρ_0 before the magnet edge.

However, a difference of up to 10 % in transmission can be observed, which could result from different ion optics due to the calculated magnetic field. This is further investigated in sections 5.3.4 and 5.3.5.

The simulations were performed with and without the use of the MBS in “1 amu down” mode. The transmission with and without the MBS varies only slightly, signifying well-designed protruding electrodes.

The optimal transmission in Figure 26 is reached at a waist distance to the nominal magnet edge of 2.4 ρ_0 and 2.3 ρ_0 for SIMION and COMSOL simulations, respectively. This corresponds to a waist position after the first slit of 210 mm and 245 mm, respectively. The rule of 2 ρ_0/2 ρ_0 object/image waist can be partly verified, in that a waist almost 2 ρ_0 in front of the magnet yields an optimal transmission. The symmetric imaging is further explored in section 5.3.4.

In Figure 27, the particle trajectories along the magnet exit beamline are plotted. A shift and broadening of the image waist away from the magnet can be observed for shorter distances, which is expected as the object waist approaches the magnet. A waist closer to the cooler entrance aperture is to some extent beneficial for injection, as a smaller beam can fit more easily through the aperture, which was also shown in (Wasserburger, 2018).

However, as the waist of the ion beam in front of the magnet moves closer, i.e. at

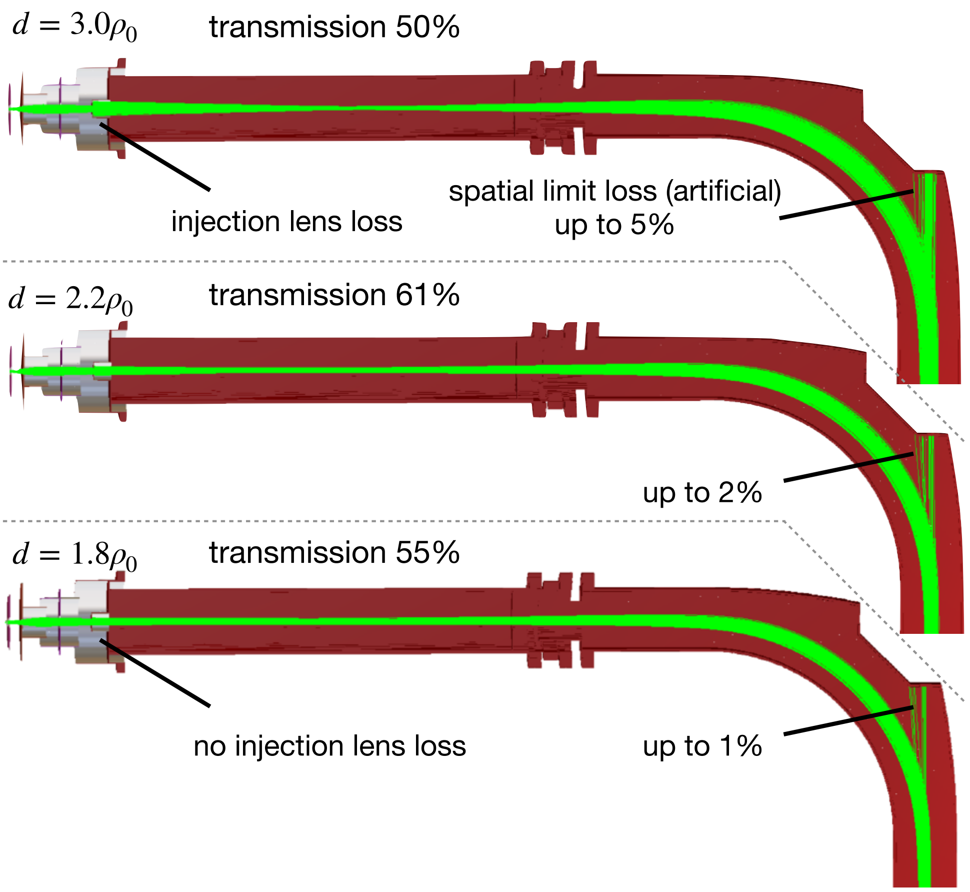

Figure 27: Ion trajectories of the COMSOL simulation at different starting points before the magnet edge ρ_0. For the longest distance, there is an artificial ion loss due to spatial limitations of up to 5 %, which is reduced to 1 % for shorter distances.

$d = 1.8\,\rho_0$, an asymmetric waist imaging is probable. Thus, the x and y waists don't align anymore, and the transmission into the cooler is lowered.

Finally, the phase measurements presented in section 4.5 were used to compare SIMION and COMSOL simulation methods, switching from one mass higher as shown in Table 2. The result is shown in Figure 28, where a strong dependence of the transmission for different input beams can be seen. The MBS doesn't affect the transmission greatly, which again is a positive indicator of the viability of this design. However, the COMSOL simulations show lower transmission values, the lower the SIMION transmission is - this disagreement in simulation methods can be interpreted as an uncertainty in the result. The main point is that for the high transmission values that are achieved in experiments, both simulation methods agree.

The low transmission of the ^{19}F$^-$ high current beam can be explained by the phase space measurement: In Figure 19, the beam is shown to have a high emittance of

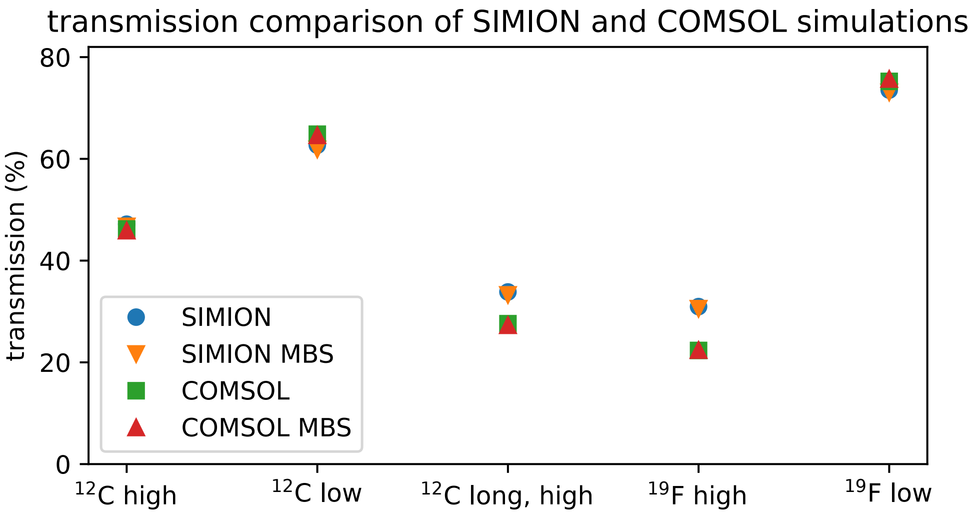

Figure 28: Transmission comparison for ion beams based on the phase space measurements shown in Figure 16 to 20. The BM and MBS values used are shown in Table 2. The transmission values for MBS and non-MBS are close together and sometimes obscure each other. This means that the variations in phase space are much larger than any difference introduced by the MBS.

around 4 and 3.5 π mm mrad for x and y, respectively, combined with a long waist distance to the magnet, around 0.9 m before the first slit. This corresponds to a distance of around 5.6 ρ_0 to the magnet edge, which is quite far considering Figure 26.

The long waist distance and high emittance lead to a large beam width at the cooler injection aperture, and thus a low transmission. In contrast, simulated ion beams with lower emittance and shorter waist distance have a higher transmission.

5.3.3 Using an octagonal steerer as an electrostatic quadrupole

As the phase space measurements presented in section 4.5 revealed that great variations in the beam shape are expected for even the same target (in particular the astigmatic beam focus), an idea to deal with this was to use the existing x/y steerer in front of the magnet as an electrostatic quadrupole, as shown in Figure 29. The steerer consists of an octagonal cylinder azimuthally split into eight electrodes, which can in principle be controlled individually, see (Moreau, 2016).

This would allow one to independently focus the beam in the x and y direction, depending on the source output of each sputtering target. Two bipolar power supplies could be connected to the x and y steerer plates, and using a DC voltage offset for each supply could maintain the present steering functionality. The beam could be optimised for transmission through the cooler using the `automax` algorithm (Steier,

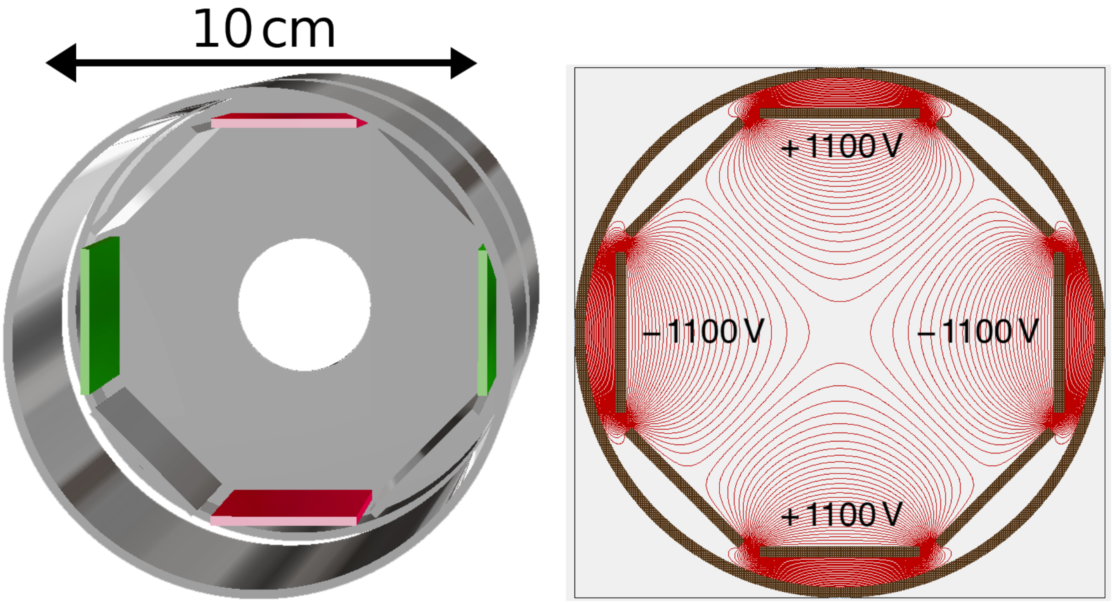

(a) 3D view of the electrostatic steerer (b) equipotential lines of quadrupole field, steps of 36 V

Figure 29: SIMION simulation of the electrostatic steerer, which was built by (Moreau, 2016). The quadrupole configuration shown here, with opposing voltages on the green and red electrodes, was simulated to be ideal for a high current $^{12}C^{-}$ beam, as shown in Figure 30.

2000), independently varying the steerer electrode voltage to focus the beam in both transverse axes, while offset voltages would be used to align the beam in both axes.

The effectiveness of this was explored in a SIMION simulation, where high current $^{12}C^{-}$ and $^{19}F^{-}$ beams were used with similar parameters as the measurements shown in figures 16 and 19, respectively. The results are shown in Figure 30, where the transmission is again defined as the percentage of the 2D Gaussian beam shape reaching the cooler injection aperture.

A variation of the quadrupole voltage over some kV shows, that an increase in transmission from 40 % to 61 % in the case of $^{12}C^{-}$, and from 76 % to 83 % for $^{19}F^{-}$ could be achieved, with moderate voltages of ±1100 V and ±820 V, respectively. For independently optimized x and y voltages, the transmission could be even higher.

5.3.4 Beam envelope

To investigate the difference in transmission shown in section 5.3.2, the beam envelope of the three simulation methods was plotted. An ideal beam with a z-aligned initial waist in x and y was chosen. As a rule of thumb, the distance between the magnetic field boundary and the image/object point is $2\rho_0$, which is where the beam waist should lie. This leads to relatively good transmission into the cooler, as seen in Figure 26.

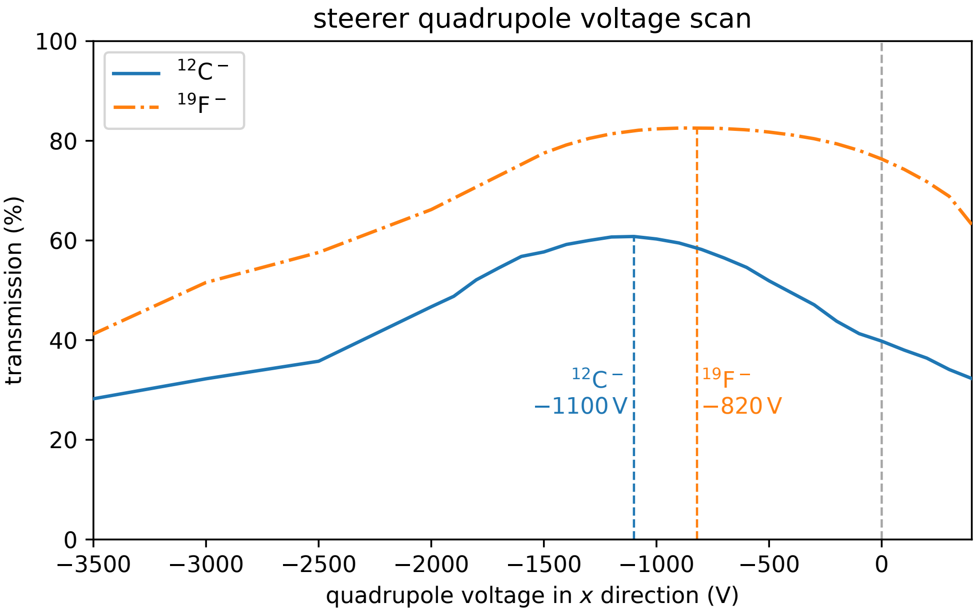

Figure 30: Transmission results from a SIMION simulation of high current $^{12}\mathrm{C}^-$ and $^{19}\mathrm{F}^-$ beams while varying the steerer quadrupole voltage. With no quadrupole voltage, the transmission is around 40 % and 76 %, which can be increased to 61 % and 83 %, respectively.

Through the Matrix calculation method, this was further found to be dependent on the beam shape. For example, if an ion beam of $x_0 = 1.5$ mm and $x'_{\text{max}} = 4$ mrad was started at 1.949 ρ_0 before the magnet edge, it showed an image waist behind the magnet at that same distance (symmetrical imaging). However, for larger and less divergent beams, this distance decreased slightly. Also, the K factor (described in section 2), which describes the edge focusing in y direction, is empirical and not yet known, so first an arbitrary choice of $K = 0.70$ was made, based on the Rogowski-like magnet edge shape.

It is important to note beforehand, that symmetric waist imaging is not of the most importance, but rather the transmission into the cooler. As shown before in Figure 27, a waist closer to the injection lens is favourable, as it generally increases the transmission. The following investigation was made to compare different simulation methods and validate their quality.

A first comparison can be made when looking at the beam envelope, which is here defined as the 1σ width of the beam along the nominal flight path. An example using the above-mentioned parameters is shown in Figure 31, where all three simulation methods are shown.

One can see that all simulation methods yield different results for the waist position after the magnet, in contrast to the common starting point. Generally, the x waist is

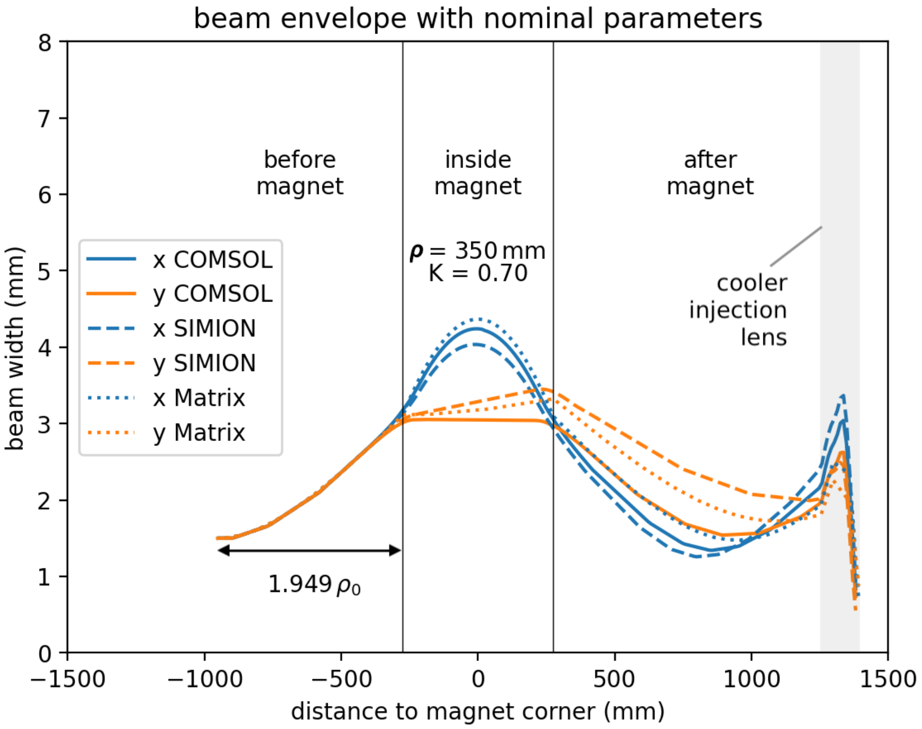

Figure 31: 1σ beam envelope of an ideal beam ideal beam of $x_0 = 1.5\,\text{mm}$ and $x'_{\text{max}} = 4\,\text{mm}$ at the waist 1.949 ρ_0 before the magnet edge. The three calculation methods are shown, with nominal values for $\rho = 350\,\text{mm}$ and $K = 0.7$ (Rogowski shape).

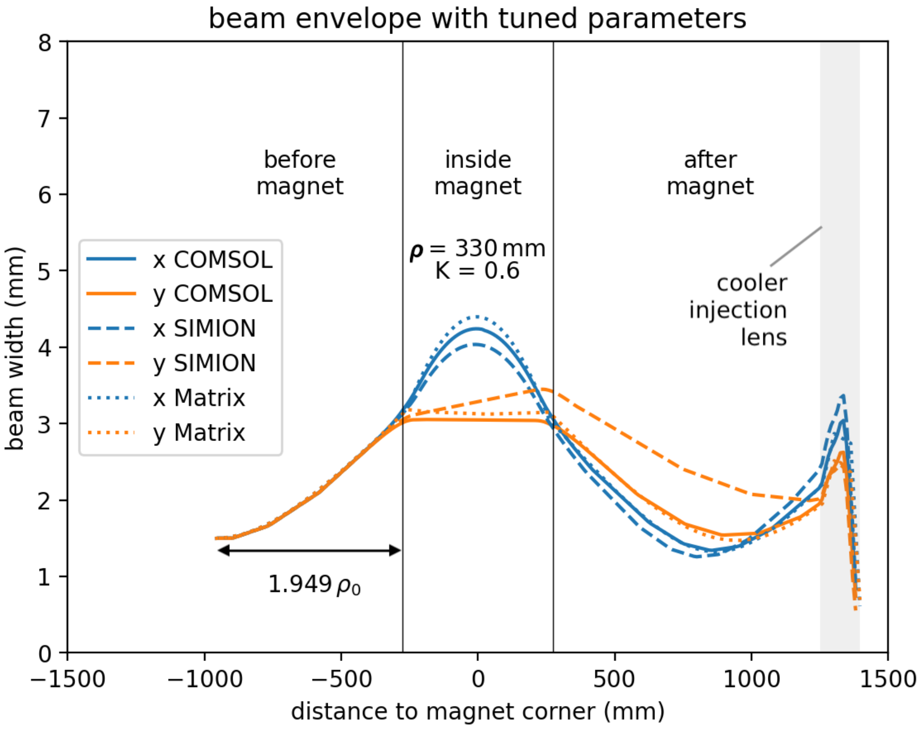

Figure 32: 1σ beam envelope of an ideal beam of $x_0 = 1.5\,\text{mm}$ and $x'_{\text{max}} = 4\,\text{mm}$ at the waist 1.949 ρ_0 before the magnet edge, with Matrix parameters tuned to fit the COMSOL simulation.

closer to the magnet for all methods, and the y waist is farther away. The simulation using the COMSOL-calculated field has the x and y waist the closest together. The SIMION simulation gives very different waists for x and y directions, and the Matrix calculation sits in between.

This is the first indication that the simulation using the COMSOL-calculated field is the most accurate one. The BM was built for stigmatic imaging, which could best be reproduced with the COMSOL field. Thus, these simulations were used as a benchmark, and followingly, values for the Matrix calculation were tuned to fit the COMSOL-based simulation.

The parameter ρ of the Matrix calculation was chosen to be ρ_0, however, this does not need to reflect the value at which the Matrix calculation method best represents the actual ion optics. An attempt to optimise ρ can be made by tuning it, along with K, to make the Matrix calculation agree with the COMSOL simulation. As ρ influences the beam in both x and y, it is tuned first to fit the COMSOL envelope in x, after which K is varied to find a corresponding y envelope.

The result is shown in Figure 32, where Matrix and COMSOL envelopes align, except for the section inside the magnet, where the Matrix calculated beam is wider. The parameters used are $K = 0.6$, which is still close to the Rogowski value of 0.7, and $\rho_{\text{opt}} = 330\,\text{mm}$.

The datasheet for the BM gives yet another radius for the trajectory, this time accounting for the “Enge effect”. This is referring to the effect of the magnetic fringe field on the beam trajectory (Wollnik, 1987). The trajectory radius considering the fringe field is given by the manufacturer as $\rho_{\text{enge}} = 365.2\,\text{mm}$. This radius is used to align the BM with the beamline and gives the best estimate for the actual flight path of ions. This doesn't mean that it should be used in Matrix calculations, where rather ρ_0 or the radius optimised to COMSOL ρ_{opt} gives a good approximation of the actual beam envelope and waist.

Figure 33 shows a 2D representation of the COMSOL-simulated magnetic field, with a normalised flux density on the colour axis. Overlayed are the results of simulated trajectories using the three different methods, where ρ_{enge} was used for Matrix calculation. This radius showed the best match with the trajectories from the other simulation methods.

One can see that the trajectory varies across the simulation methods, which is mostly because they start being deflected before the 350 mm nominal magnet edge at different points. One can define two different parameters to describe the trajectory: The radius

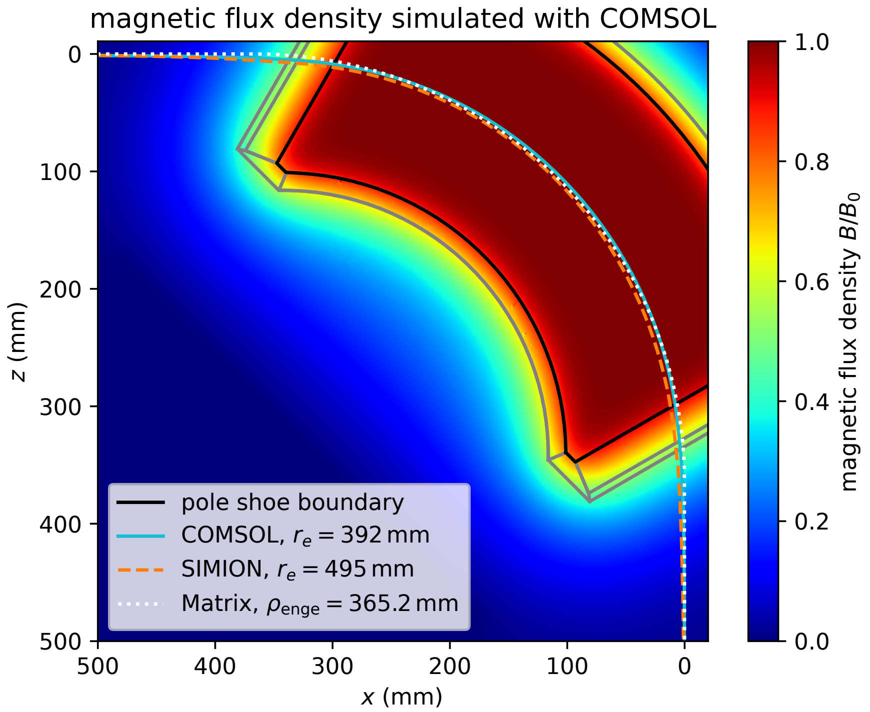

Figure 33: Path of the ion beam within the magnet, including the COMSOL-simulated field. Three different ion simulations are shown: COMSOL, SIMION, and Matrix calculation with fringe-field corrected radius ρ_{enge}. The radius r_e given for the other methods shows the position where the x deflection from a straight trajectory is greater than 1 mm. Also drawn are the boundaries of the pole shoe, to illustrate the magnetic field geometry.

of the trajectory inside the magnet can be called r_i (inner or actual radius). To obtain it, a circle was fitted to the inner part of the trajectory. The second parameter is called r_e (effective radius), and is defined as the point where the deflection from a straight trajectory is more than 1 mm. They are shown in Table 3.

Table 3: Inner (r_i) and effective (r_e) radii of the trajectories in the bending magnet, as calculated by three different methods. For the matrix calculation, only the inner radius is used, and the effective radius given here is ρ_{enge}, which was used to illustrate the actual flight path in Figure 33.

	r_i in mm	r_e in mm
COMSOL	342.6(10)	392(10)
SIMION	338.0(10)	495(10)
Matrix	330	365.2

The inner radius of both SIMION and COMSOL trajectories is around 340 mm, which is comparable to, but higher than $\rho_{\mathrm{opt}} = 330\,\mathrm{mm}$ obtained from the parameter tuning using the envelope.

The effective radius is larger for both simulations, showing that the magnetic fringe field affects the simulated trajectory well before entering the magnet. For SIMION, r_e is particularly large, meaning that the magnetic fringe field reaches far outside the magnet for the SIMION simulation. Neither Matrix nor COMSOL methods show this strong behaviour, and it is further explored in the following section.

The evaluation above shows that the inner radius of the trajectory, i.e. the actual radius of the flight path inside the magnet, is comparable to ρ_{opt}. This verifies the previous strategy of tuning the Matrix parameters until the beam envelope fits the COMSOL-based simulation. In Figure 33, it can be seen that the COMSOL and Matrix trajectories match better than the SIMION trajectory does to any of the two.

This further demonstrates that the COMSOL-calculated field is more accurate, as it not only shows the most stigmatic imaging but also the ion trajectory inside the magnet fits best to ρ_{enge}.

5.3.5 Magnetic fringe field

The large effective radii, especially for SIMION, indicate that the effect of the magnetic field reaches farther out than the nominal field edge. This can be further illustrated by looking at the magnetic flux density along a line perpendicular to the pole shoe boundary, called ζ. In Figure 34, the magnetic field is plotted over the distance from the nominal magnet edge, normalised to half pole gap units $g/2 = 25\,\text{mm}$.

Also shown is the effective magnet boundary $\zeta^\star$, which satisfies the following condition, where $-\zeta_0$ is a point along ζ inside the magnet where the flux density is maximal, i.e. $B = B_0$ (Wollnik, 1987):

$$\int_{-\zeta_0}^{\zeta^\star} 1 - B(\rho)\mathrm{d}\rho = \int_{\zeta_\star}^{\infty} B(\rho)\mathrm{d}\rho \tag{29}$$

The two integrals are illustrated in Figure 34 as the orange areas. As can be seen, $\zeta^\star_{\text{SIMION}} = 0.92\,g/2 = 23\,\text{mm}$ is larger than $\zeta^\star_{\text{COMSOL}} = 0.60\,g/2 = 15\,\text{mm}$, which adds a quantitative statement to the fact that the SIMION calculated magnetic field has a longer fringing field tail than the COMSOL simulated one. As previously explained, more trust can be laid in the COMSOL-based simulation.

The low precision of the magnetic potential array in SIMION 8.1 was considered as a possible explanation for the longer fringe field. The magnetic PA occupies a lot of memory, so efforts were made to reduce the precision to a minimum acceptable level. The grid unit size was first set to 0.5 mm, but an increase to 1 mm showed only very little effect on the transmission, so the bigger value was kept. Also, the size of the PA was considered to be of influence, as there is a built-in Dirichlet boundary condition of no field at the outer edge of the PA. However, varying the extent of the entrance and exit size between 400 and 1000 mm again showed little change.

Another idea to increase the PA precision with minimal memory requirements was to use the "fractional grid units" feature, also applied by (Pitters, 2015). While this feature is available in SIMION 8.1 for programmatically defined geometries, the pole shoe was imported as an `.stl` file. For the `.stl` import functionality, only SIMION 8.2 and above provide the feature of fractional grid units, or "surface enhancement". The pole shoe geometry is quite complex and it was thus not possible to define it programmatically in the available time.

Besides these efforts, SIMION uses the approximation of a constant magnetic flux density on the pole shoe surface, as explained by the software's author (Manura, 2022). The effect is probably more noticeable than any refinement made by surface enhancements, so the COMSOL-simulated field represents the best solution.

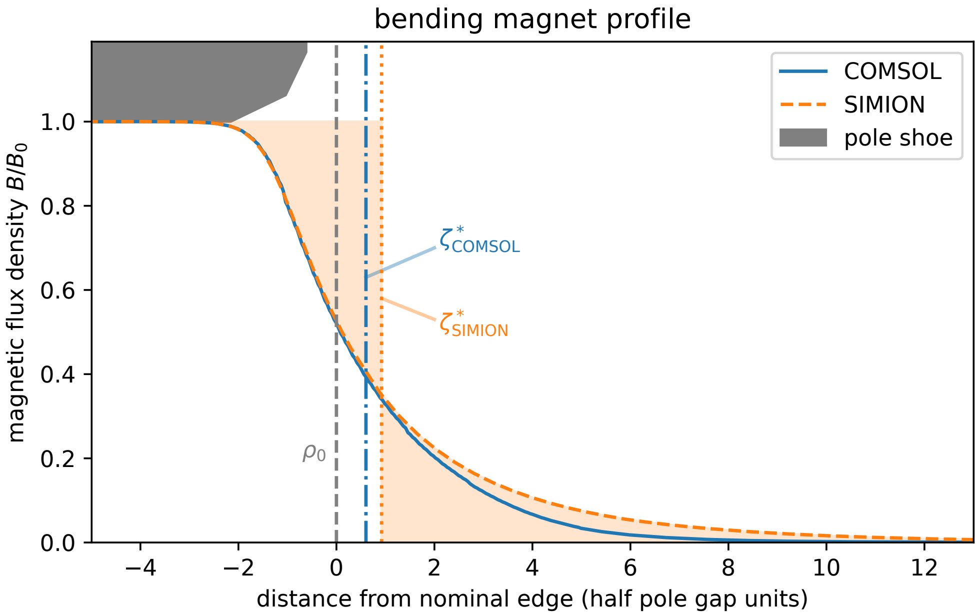

Figure 34: Normalised magnetic fringe field, calculated with COMSOL and SIMION. On the x-axis, the distance to the nominal field edge along the ζ-axis (perpendicular to the pole shoe boundary) is shown in units of half the pole distance $g/2 = 25$ mm. Also shown is the shape of the magnet pole shoe, which indicates the geometry. The effective magnet boundary ζ^* is also shown for both simulations, which is (in the case of SIMION) the point where the two orange integrals are equal.

5.4 Conclusions from simulations

As some construction on the beamline was necessary for this project, one idea was to move the ion source as well, if that provided some ion optical benefit to the cooler injection beamline. However, through the phase space measurements and subsequent simulations, it was found that the waist position of the beam varies widely depending on the ion source and target parameters, so there would be no benefit from one single source position; instead, an electrostatic quadrupole lens was devised. The ion source doesn't need to be moved, resulting in a quite constrained space for the MBS electrodes and insulators, which is dealt with in the following section.

Different simulation methods were used in this chapter. Mainly, through SIMION simulations, the shape of the protrusion and shielding electrodes was determined, allowing for only slightly reduced transmission into the cooler. SIMION was also used to determine the beam envelope along the ion trajectory, proving that the waist position before and after the magnet is not fixed at one point for all measured phase spaces.

Furthermore, matrix calculations and COMSOL simulations were used to validate these results and provide a measure of uncertainty, especially for the falloff of the magnetic field around the magnet. As presented in the previous sections, the COMSOL calculated field better represents the actual field. It should thus lead to more realistic results of the simulation. As shown in Figures 26 and 28, the transmission into the cooler obtained by the two simulation methods differ by some amount. Especially for low transmission values around 30 %, the COMSOL-calculated field shows up to 10 % lower transmission than the SIMION simulation. The effect is not as pronounced for higher absolute transmission values.

The use of the existing x/y steerer in front of the magnet as an electrostatic quadrupole seems promising, as a transmission increase from 40 % to 61 % of a $^{12}\mathrm{C}^{-}$ ion beam based on phase space measurements could be achieved in simulations. As the phase space of a single target changes with time, the quadrupole would need to be retuned every once in a while.

6 Construction of the MBS

After finalizing the design by simulation, evaluation and iteration, the parts for the MBS had to be manufactured and integrated into the beamline. Technical drawings of the two MBS electrode/insulator stacks were created from CAD files of the magnet, which are shown on page 126 in the Appendix.

6.1 Part manufacturing

The PEEK insulators between the magnet chamber and the grounded beamline were cut from a PEEK cylinder of 150 mm diameter, with a height of around 24 mm each. The biggest concern was to prevent arc discharge through the air, which has a smaller dielectric strength than PEEK or Nylon, at around 3 kV/mm, depending on the source (Lehr & Ron, 2017) (Kögler, 2014). The physical distance between the two potentials ($U < 5\,\text{kV}$) thus is big enough to prevent arc discharge, with a margin of >1 order of magnitude.

The two cylindrical disks were turned on a lathe to have a ConFlat® flange-like knife-edge so that a rubber seal could be used for holding the vacuum. Following this step, the surfaces were sanded very fine to furthermore ensure a proper seal. After drilling CF100-like holes, the corresponding 5/16" 24 UNF screw threads were cut from 8 mm nylon tubes. A vacuum test with a Tribodyn® turbopump was done, see Figure 35. A pressure of $< 10^{-5}$ mbar was quickly reached and maintained, with the pump continuously running.

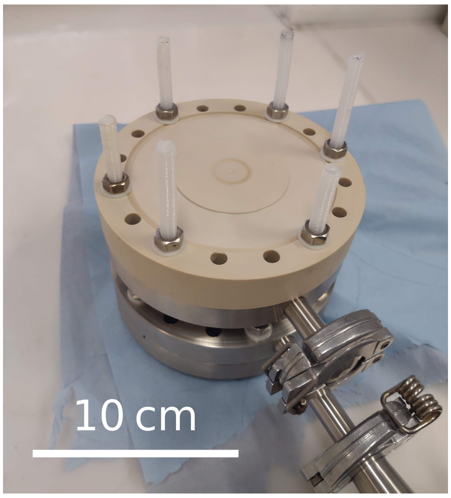

Figure 35: PEEK insulator screwed to a vacuum test flange with six out of 16 nylon screws, holding a vacuum of $< 10^{-5}$ mbar. The central hole for the ion beam is not yet drilled.

Also, using a Helium leak detector, there were no leaks found at 6×10^{-3} mbar (upper boundary), with a constantly decreasing pumping flow rate of $< 10^{-8}$ mbar l/s.

Having screwed the nylon screws into the bellows threads and out again, some oil residue was found in the grooves. Thus, the screws were cleaned in acetone in an ultrasound bath for 15 min, to prevent leakage current through oil residue over the screw surface. An option for the screws would be to clamp the bellows and magnet chamber flanges together, with the PEEK insulator in between. The clamp jaws would need to be electrically insulated, but an easier construction and de-construction would thus be possible. However, the acrylic sheets for HV insulation would need to be remade. This is considered an option in the future, especially if concerns about the insulating property of the nylon screws increase.

Finally, the central hole was cut with a hole saw of 100 mm diameter.

The electrically grounded aperture in front of the MBS as well as the protrusion holders were cut from 1.5 mm thick steel sheets using a CNC mill. The protrusion was made by rolling 1 mm perforated steel sheet and spot welding it to the protrusion holders.

For the electrodes to work, they need to be properly in contact with the respective parts of the beamline. Soldering, welding or screwing the pieces to the beamline wasn't possible, because possible residuals would pose a threat to the turbopumps in operation next to the magnet, and because there was not enough space: If the protrusion had been attached to the magnet chamber, the bellows wouldn't fit between it and the other side of the beamline. Thus, the whole stack had to be inserted into the empty beamline section as one piece, with the question of how electrical contact is ensured dealt with afterwards.

It was tackled by using the vacuum seals: Rubber gaskets were not only used as a seal between the insulator and beamline but also to press the protrusion to the magnet chamber, as can be seen in Figure 36. The flat, toroidal protrusion holder was made to fit right inside the knife-edge of the CF100 flange of the magnet chamber. The nylon screws thus press the bellows and magnet chamber together, sealing off both sides of each insulator.

The grounded aperture on the entry side was conceived for the same sealing mechanism. However, its outer diameter was accidentally cut too small, such that it fits right inside the rubber gasket (smaller than the CF 100 knife-edge enclosure). The screws between the bellows and gate valve thus don't press the aperture directly onto the flange surface. Nevertheless, with the bellows attached to a blind flange and the aperture in-between,

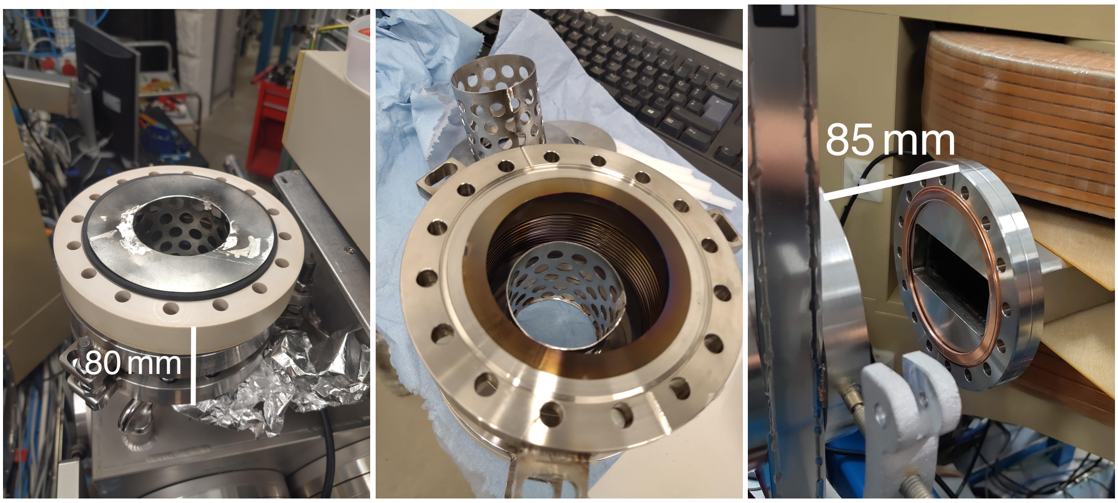

(a) View from the magnet side (b) View from the far side of magnet (c) Empty beamline section

Figure 36: The sandwiched stack consisting of the protruding electrode, insulator, and bellows, for the part installed on the exit side. One can imagine the stack in Subfigure a) rotated 90° clockwise and inserted into the empty beamline section in Subfigure c). The rubber gasket thus presses the protrusion to the magnet chamber.

an electrical continuity test resulted positively, and it was determined that the radial pressure from the gasket would suffice to press the electrode towards the flange surface.

Inserting the insulators and electrodes into the beamline was challenging due to the small space before and after the magnet chamber. As seen in Figure 36, the sandwich of electrode-insulator-bellows-(electrode) had to be inserted into the beamline in one piece, with the nylon screws being inserted only afterwards. After a failed vacuum test, the rubber gaskets and apertures between the sandwiches were readjusted using long pins, after which the vacuum readily went towards 2×10^{-8} mbar. This was deemed low enough for normal cooler operation.

To protect lab workers from the high voltage on the magnet vacuum chamber, acrylic sheets were used to construct a cage around the exposed parts of the assembly, see Figure 37. The viewport for looking into the ion source is insulated by a ceramic break, with an acrylic sheet between the two metallic ends. This allows for accessing the viewport even while the MBS is in operation.

Also, the vacuum port where the laser is shone into the beamline is insulated by a PEEK ring, with a metal tube optically protecting the space between the laser box and the vacuum system.

The bipolar, four-quadrant switching power amplifier 10/40A-HS by Trek, Inc. was bought for this project. It is capable of amplifying an input signal of up to $\pm 10\,\mathrm{V}$ by a factor of 10^3, featuring a slew rate of $> 900\,\mathrm{V/\mu s}$. This value is sufficient for

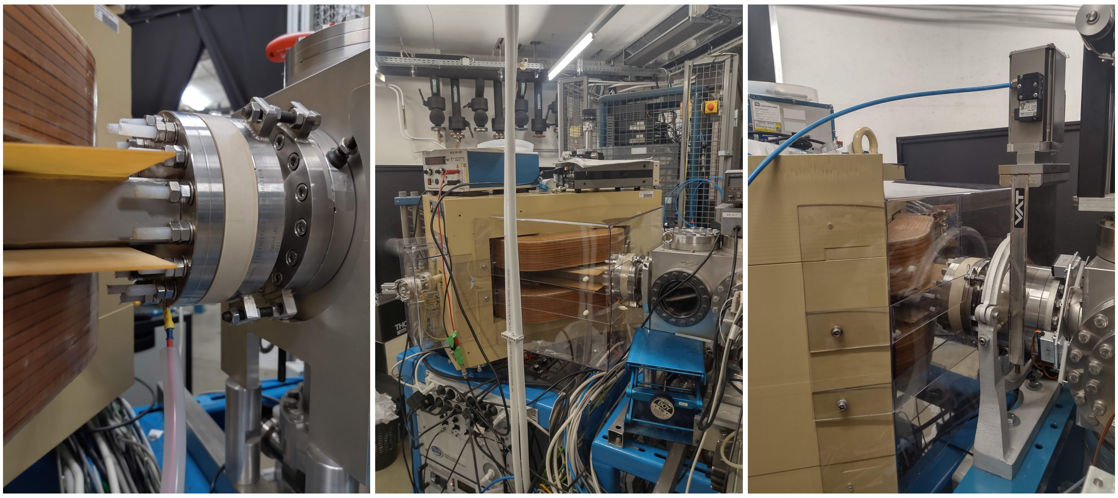

(a) Final insulator assembly (b) Exit side of MBS (c) Entry side of MBS

Figure 37: Photos of the final MBS installation, with acrylic HV insulation. In Subfigure a), the double-insulated high-voltage cable connecting the power supply with the magnet chamber can be seen.

switching the beam to higher and lower masses within µs, see also Figure 4. The power amplifier output was connected to the magnet chamber with a high-voltage-insulated cable connected to a washer. Two nuts were screwed on one of the nylon screws pressing the washer to the magnet chamber flange.

6.2 Performance test

A first test of the power supply performance was used to determine the actual slew rate. The magnet chamber acts as a capacitive load, so the slew rate is expected to decrease when the power supply is connected to it.

After setting the internal resistance of the power supply to a value that leads to a critically damped response, a voltage of 5 kV was applied to the magnet chamber (see Figure 38). The slope of the observed voltage rise amounts to 134 V/µs, which corresponds to about 15 % of the maximum slew rate (SR) of the power supply. During this step-on, a maximal current draw of 66 mA was measured at the amplifier current monitor. The capacitance of the magnet chamber can thus be calculated as $I/\mathrm{SR} =$ 493 pF, which explains the low value of the achievable slew rate. However, for switching between $^{35}\mathrm{Cl}^-$ and $^{37}\mathrm{Cl}^-$, which requires around 1620 V, a time of only 12 µs is needed. The ion residence time in the cooler is on the order of ms, so the MBS is fast enough that a change in the injected mass can be considered instantaneous.

At last, the transmission of $^{35}\mathrm{Cl}^-$ through the ion cooler was measured, depending on the MBS voltage. To do this, the MBS was set to a given voltage, and the BM field strength was varied until $^{35}\mathrm{Cl}^-$ transmission through the cooler was maximised. The procedure for this was a quick `scan` of the BM current, followed by a run of `automax` for the BM, steerer voltages and `InjHI` lens. The result is shown in Figure 39, in

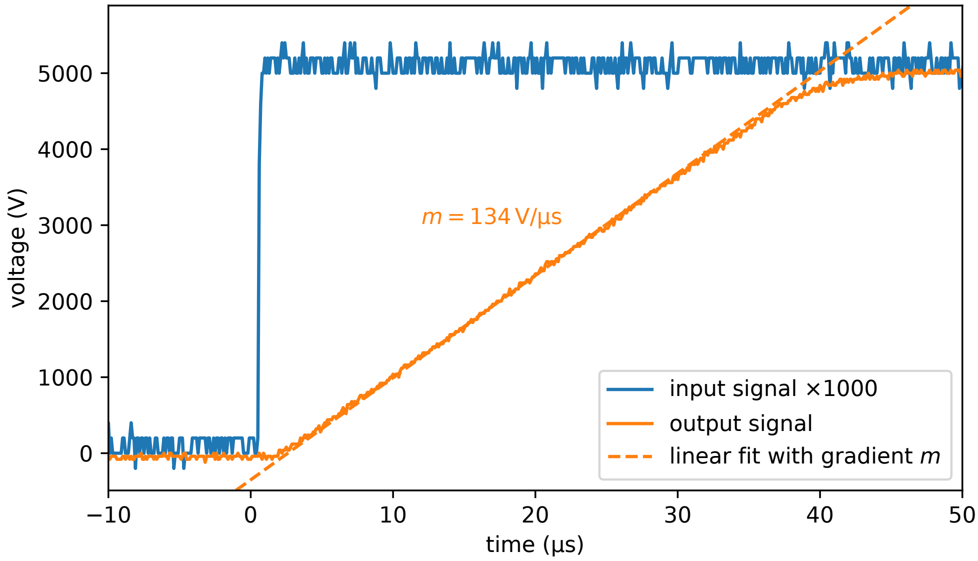

Figure 38: Monitoring the magnet chamber voltage (orange curve) while applying a voltage of 5 kV to it (blue signal). The slope m of the orange curve corresponds to a slew rate of 134 V/µs.

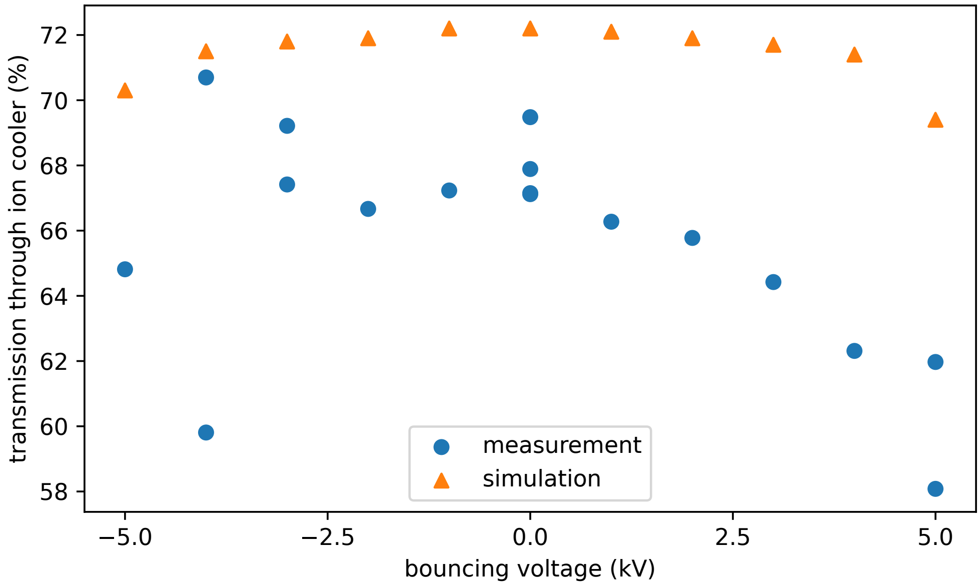

Figure 39: Transmission of a $^{35}\mathrm{Cl}^-$ beam through the ILIAMS cooler, depending on the MBS voltage. For comparison, results of a simulation of an $^{19}\mathrm{F}^-$ beam, based on the phase space shown in Figure 20, are shown. The latter only gives the transmission of the ions into the cooler aperture, not through the cooler. In both cases, a decreased transmission is observable for stronger MBS influence.

combination with the results of a simulation of an $^{19}\mathrm{F}^-$ beam based on the phase space shown in Figure 20.

Both curves show a decrease in transmission for bouncing voltages further from 0. The simulation shows systematically 5 % higher transmission values than the measurement. This can be neglected, as the phase space of the simulated ion beam of $^{19}\mathrm{F}^-$ is only to some extent comparable to the measured $^{35}\mathrm{Cl}^-$ beam. The relative decrease in transmission of both measurement and simulation is compatible. Furthermore, this signifies good electrical contact between the cylindrical protrusions and the magnet chamber.

7 Ion residence time measurements

The residence time of ions in the ILIAMS cooler has been studied before (Moreau, 2016), but only in situations which didn't chiefly involve the effects of space charge. The previous experiments provided some insight into the physical processes in the cooler, which is outlined below.

7.1 Previous measurements

As no MBS was present for the measurements, an electrostatic steerer was used to deflect the ion beam away from the cooler injection. This provided a sharp time signal for the residence time measurement, but only for starting or stopping the injection of ions. Thus, one could only look at the loading of ions into an empty cooler, or the unloading of ions until the cooler was empty.

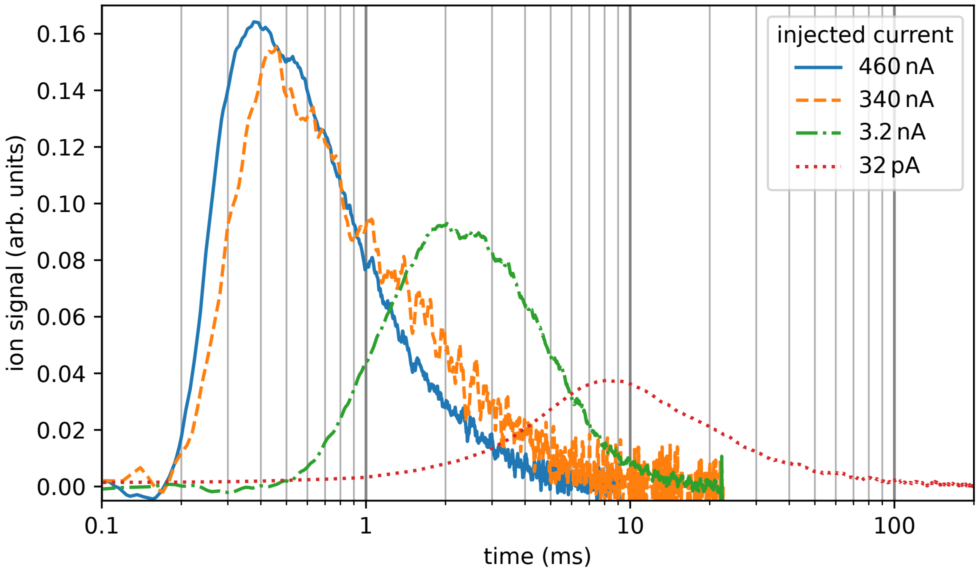

Figure 40: Measurements of the ion residence time of a $^{63}Cu^{-}$ beam in the cooler during **unloading** at different injection currents, adapted from (Moreau, 2016). The x-axis shows the time in ms, and the y-axis shows the smoothed and differentiated ion signal behind the cooler, resembling a residence time distribution. For high currents, the residence time is in the order of several hundred µs, for lower currents it can reach tens of ms. Also, a pronounced tail towards longer times is evident.

The residence time in the cooler is strongly dependent on the injection current, as is shown in Figure 40. At low currents in the pA range, the residence time is in the order of some ms. At higher currents up to hundreds of nA, the time is much shorter at hundreds of µs, which is assumed to be due to space charge effects in the cooler.

The higher the current, the more ions per time unit are injected into the cooler, which would exert a stronger Coulomb force on ions inside the cooler towards the extraction lens. This leads to shorter residence times, while in turn, the lower currents provide less space charge and thus longer residence times.

Furthermore, dependencies of the ion residence time on cooler parameters were observed: longer residence times at higher gas pressures and lower guiding field strength.

The pronounced tail towards longer residence times is likely an effect created by the measurement method of unloading the cooler. Because the cooler injection was stopped at the measurement start, space charge effects were less prominent the more time passed, possibly leading to a long tail in residence times.

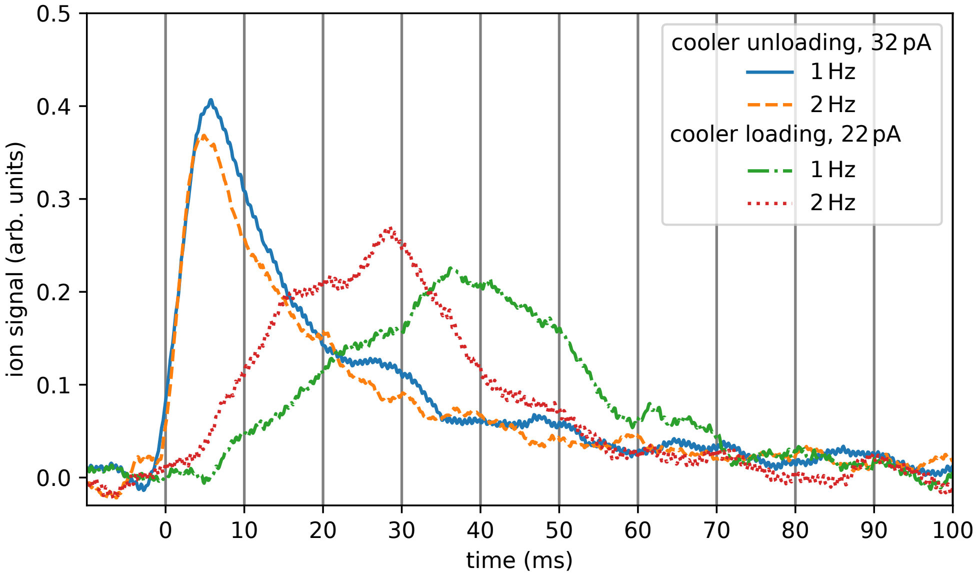

Figure 41: Comparison of residence times of $^{63}\text{Cu}^{-}$ for cooler loading and unloading at different repetition frequencies, adapted from (Moreau, 2016). In addition to the longer residence times at lower currents, unexpected behaviour can be observed for cooler loading when changing the frequency of the repetitive loading and unloading.

Another interesting effect of this measurement method was observed at cooler loading and is shown in Figure 41. All the measurements were done repetitively to average out noise in the data. When changing the repetition frequency from 1 to 2 Hz, the residence times shifted to around 25 % lower values. This is only observed during the loading of the cooler, which leads to the assumption that this is an effect of the non-equilibrium nature of the observed cooler state. A possible relation to residual ions in the cooler is unlikely, however, there is the possibility that the charging of surfaces inside the cooler is the explanation (Martschini et al., 2017).

7.2 Test setup

To evaluate the ion residence time in the cooler under equilibrium conditions and observe space charge effects, the newly built multi-beam switcher was used to switch between different stable isotopes of the same atom. For the current to be at least comparable, they needed to be similar in abundance and a possibility was the use of ^{35}Cl and ^{37}Cl as they have natural abundances of around 76 and 24 % respectively, leading to a 3:1 ratio of the injected currents (Soti et al., 2019). The MBS should be able to switch between the two isotopes within 12 µs, considering the switching voltage of 1620 V calculated in section 1.1 and the power supply's effective slew rate of 134 V/µs. Compared to residence times of several hundred µs, this is sufficiently fast.

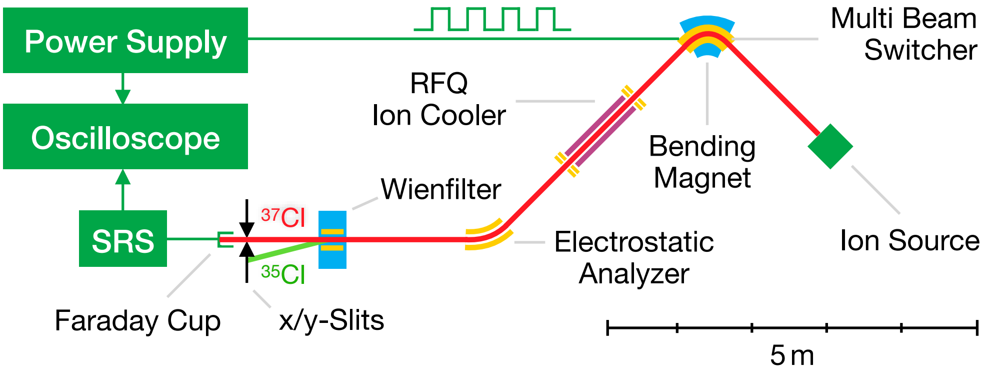

Figure 42: Test setup for measuring the equilibrium ion residence time in the ILIAMS cooler. A function generator sends a square wave to the power supply, which in turn controls the MBS voltage. After the cooler, an ESA selects the energy of 30 keV, and a Wien filter is used to select either ^{35}Cl$^-$ or ^{37}Cl$^-$ ions, based on their speed. After an x/y-slitpair, the beam current is detected by a Faraday cup and an SRS current amplifier, and displayed on an oscilloscope, with the trigger signal coming from the power supply voltage monitor.

A scheme of the test setup is shown in Figure 42. Behind the Wien filter, an x slit can separate the ^{35}Cl$^-$ and ^{37}Cl$^-$ beams and a Faraday cup is used to measure the ion beam current down to a level of hundreds of pA. The ion drift time outside the cooler (between MBS and cooler entrance as well as cooler exit and Faraday cup) was calculated to be around 17.4 µs, which is accounted for in the results.

The measurements were done in two fashions (cf. section 1.3 for theoretical details): Using a step-like change of the injected ion beam, and via a pulsed injection of the tracer ion beam. For example, in the case that ^{37}Cl$^-$ was used as the tracer beam (with the Wien filter set to let through ^{37}Cl$^-$), both a negative and positive step change was measured (from ^{37}Cl$^-$ to ^{35}Cl$^-$ and vice-versa), as well as a pulsed injection of ^{37}Cl$^-$ into a ^{35}Cl$^-$-filled cooler.

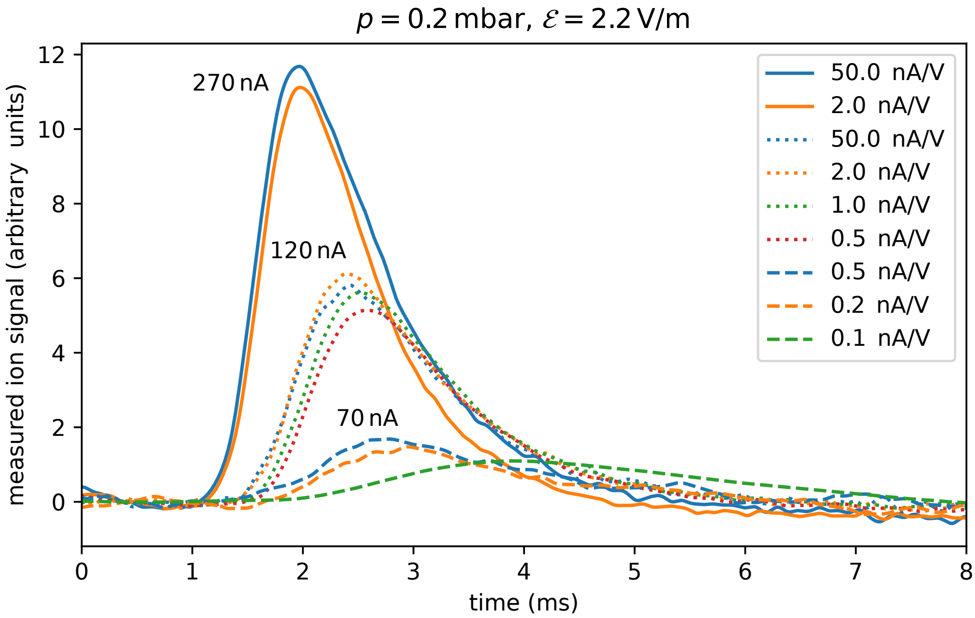

Figure 43: Comparison of current amplification settings of the SRS preamp. At different beam currents, the setting was changed and the signal was compared. The lowest reliable setting is 0.2 nA/V, as for lower settings, the integration time is probably too high, leading to a deformed signal.

To set the Wien filter to let through e.g. $^{35}\text{Cl}^-$, a plate voltage was chosen and the magnetic field strength was continually changed until the highest transmission was reached. The x-slit after the filter had an opening of 1 mm, which reduced the current without filter to only about 90 %. At the chosen values for the Wien filter (for $^{35}\text{Cl}^-$: $\mathcal{E} = 658\,\text{V/cm}$ and $B = 1618\,\text{G}$), the $^{35}\text{Cl}^-$ and $^{37}\text{Cl}^-$ beams were calculated to have a separation of 17 mm from centre to centre, which is far enough apart for the 1 mm slit width.

To enable the measurement of relatively low currents of $\sim 1\,\text{nA}$, an attenuator was used before the BM to reduce the beam current by a factor of 35.

The signal from the Faraday cup was fed into a low-noise current preamplifier, a Stanford Research Systems (SRS) SR570, set to the “high bandwidth” gain mode. A 6 dB lowpass filter with a cutoff frequency of 10 kHz was applied (and in some cases, where a lower noise background was present, 30 kHz). Depending on the ion beam current, the sensitivity was varied between 50 nA/V and 0.2 nA/V, which was the lowest setting at which a reasonable time resolution could be achieved. This is documented in Figure 43, where different settings were compared at different ion beam currents, and the 0.1 nA/V setting can be ruled out, probably due to a too-long internal time integration of the SRS.

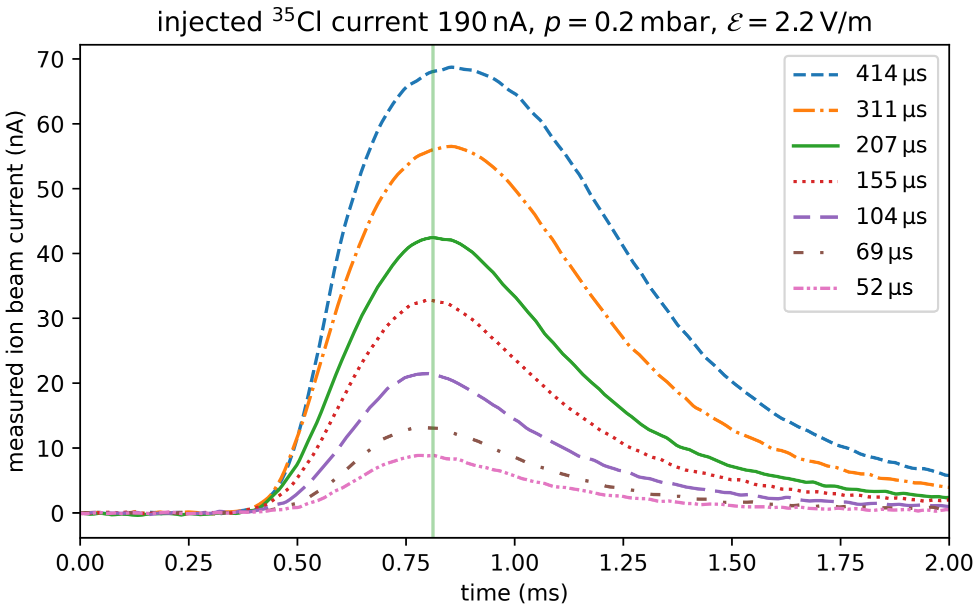

Figure 44: Comparison of pulsed injections of ^{35}Cl$^-$ with varying pulse width into a cooler filled with ^{37}Cl$^-$. For longer pulses, a higher current, broadened peak and shift towards longer times are observed. The solid vertical line shows the peak time of the chosen 207 µs pulse width.

Figure 44 shows the dependence of the pulsed injection on the pulse width. Longer pulses result in a broadened shape, but a higher overall signal, so a reasonable tradeoff is achieved at 207 µs, with the peak position marked with a solid vertical line. With this pulse width, the detected ion beam current is still sufficient for the measurement of different intensities and cooler parameters, but the peak shape is still preserved to a large extent.

The measurements were acquired by an oscilloscope, with the MBS voltage change slope acting as a trigger. As the signal was still noisy even after the bandpass of the preamp, several measurements were performed and averaged. Two raw measurements are shown in Figure 45, for the step change and peak method respectively, using ^{37}Cl$^-$ as a tracer. An average over 11 measurements is overlayed as well.

For certain cooler settings, especially at low beam currents, a 50 Hz "phantom signal" was visible. In the case of Subfigure 45b, the Wien filter is set to ^{37}Cl$^-$, but one gets an additional signal overlaying the actual expected pulse signal of ^{37}Cl$^-$. This phantom signal could be identified as artificial, because it doesn't change its repetition frequency of 50 Hz when changing the injection frequency of the ^{37}Cl$^-$ pulse, so on the oscilloscope it appears to move along the time axis at different speeds. A possible explanation is a voltage fluctuation in one power supply, which has been observed before. It could lead to a stray partial beam of ^{35}Cl$^-$ with an energy around $1 - 35/37 \approx$

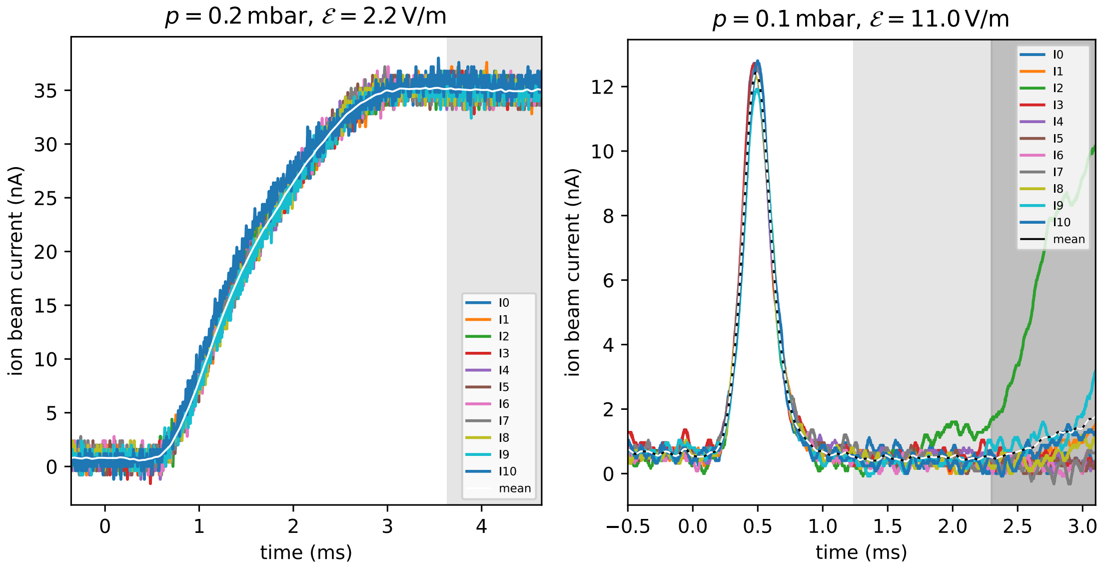

(a) Step change experiment

(b) Pulse experiment

Figure 45: Raw data from measurements with a $^{37}\mathrm{Cl}^-$-beam of 55 nA as a tracer, using the two principles: step change and pulse. Light grey areas indicate the initial/minimum values, to which the signal was normalised. The dark grey area was discarded as it does not represent a $^{37}\mathrm{Cl}^-$ signal, but a stray $^{35}\mathrm{Cl}^-$ beam of different energy, probably due to a voltage fluctuation. Overlayed in white and black/white, respectively, is an average of the 11 single measurements. All residence time measurements are shown in Figure 67 and following in the Appendix.

5 % lower than 30 keV after the cooler, which would be able to pass the Wien filter set to $^{37}\mathrm{Cl}^-$ at 30 keV.

During measurements, this had to be taken into account by adjusting the injection frequency, so that the phantom signal didn't constantly overlap with the true signal, and waiting for times where it was negligible in the region of interest. The rising slope on the right end of Figure 45 is such an example, and for evaluation, the data is cut off at 2.4 ms in this particular example, and likewise in other cases (cf. Figure 67 and following in the Appendix for an overview of all measurements and cut-off ranges).

7.3 Results

In the following section, the measurement results are visualised and analysed. Mean residence times are calculated and shown, they are to be seen as equilibrium mean residence times, i.e. referring to an equilibrium situation in the cooler, unless stated otherwise (i.e. for weighted mean average times).

The "buffer gas pressure reading" given in the following section is the pressure reading at the gas inlet valve, which corresponds to a buffer gas pressure around five times lower inside the cooler (Gaggl, 2021).

7.3.1 Step experiments

In Figure 46, the results from a step change experiment with varying cooler injection currents of $^{35}\mathrm{Cl}^-$ and $^{37}\mathrm{Cl}^-$ are shown, with an arbitrary scaling factor to be able to show them in one plot. For lower currents, the newly injected species is detected with more time delay and spread out over a longer period. Important to note is the fact that the blue 200 nA curve represents a different situation in the cooler than the

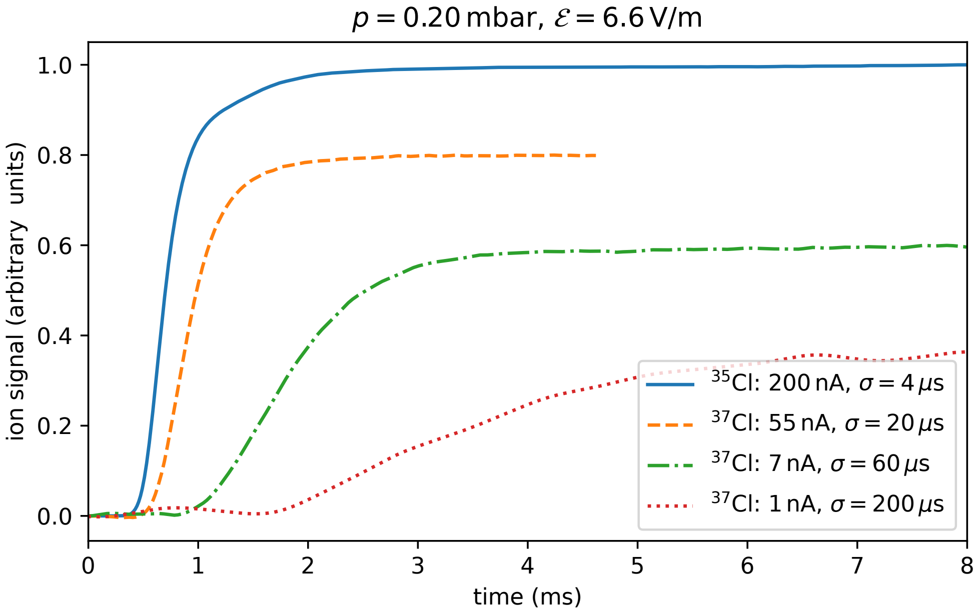

Figure 46: Measured step-on experiment with both $^{35}\mathrm{Cl}^-$ and $^{37}\mathrm{Cl}^-$ as tracers at different currents. A moving weighted average with a window width of σ (given in the legend) was applied to further smooth out the averaged data. One has to note that the different tracers $^{35}\mathrm{Cl}^-$ and $^{37}\mathrm{Cl}^-$ correspond to different situations in the cooler: For the former, the cooler was previously filled with the lesser-current $^{37}\mathrm{Cl}^-$ (which have a shorter residence time, cf. (Moreau, 2016)), so there is less ion density in the cooler. For the latter, the reverse case is true, with the $^{37}\mathrm{Cl}^-$ ions entering a more densely filled cooler.

rest: For the former, the higher-current $^{35}Cl^-$ beam was injected into a less-densely $^{37}Cl^-$-filled cooler. The newly injected ions thus can propagate through the cooler more easily, possibly leading to a shorter residence time than in an equilibrium state (i.e., equal-current injection of ion species).

The other curves in Figure 46 represent the reverse case, where the less-current $^{37}Cl^-$ ions enter a more densely filled cooler, possibly leading to initially longer residence times, until the system equilibrates. To evaluate this effect, the step-on experiments are later compared to step-off experiments, which should show the opposite behaviour.

To compare the obtained curves with the previously done measurements by (Moreau, 2016), the signal has to be derived as described in section 1.3. As a preparatory step, the curves in Figure 46 are already shown with a moving weighted average applied to them, as this smoothes out the derivative significantly, and was also done by (Moreau, 2016).

Figure 47 shows these derived curves, arbitrarily scaled for visualisation. In theory, these curves should match a pulse experiment with the same parameters, as the observed quantity is the RTD in both cases. However, the pulse experiments exhibited a shift towards longer residence times, and are not shown here, but in a later section.

From the measured step-change experiments, a mean residence time can be calculated

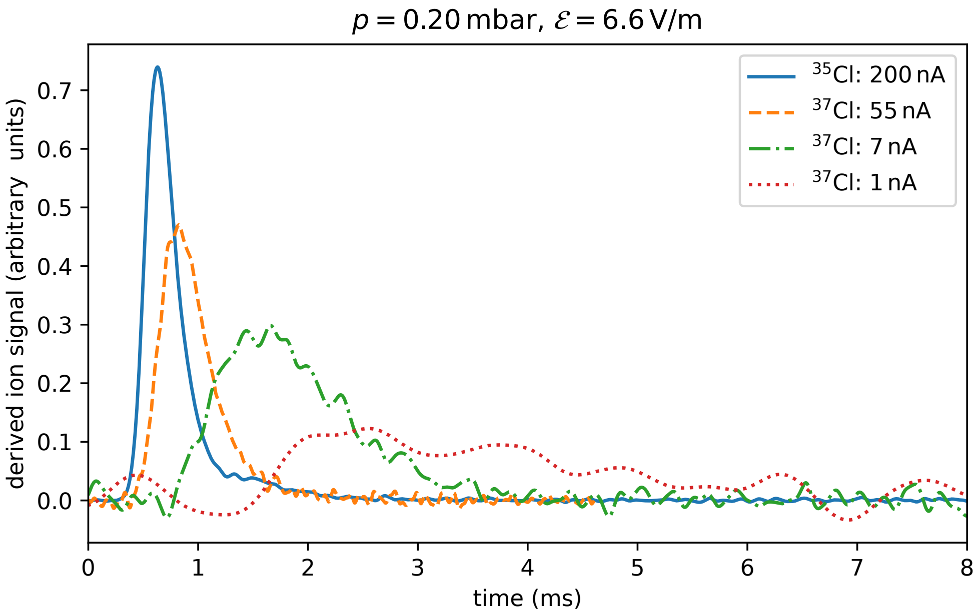

Figure 47: Shown are the derivatives of the step-on experiment curves from Figure 46. One has to again note the different nature of the initial cooler state for both tracer isotopes: The solid blue line corresponds to $^{35}Cl^-$ being injected into a $^{37}Cl^-$-filled cooler, while the reverse is true for the other lines.

by integrating over either the inverted step-on curve or the step-off curve (washout function), as explained in section 1.3. The step-off measurements are shown in the following section, but the mean residence times obtained by them are already included in this analysis.

The mean residence times are plotted in Figure 48 as a function of buffer gas pressure and injected ion current. For higher pressures, as well as lower currents, a longer mean residence time is observed. The values obtained by the step-off experiment are consistent (within their error bars) with the step-on change values.

Figure 49 shows the dependence of mean residence times on the guiding field strength, as well as the ion beam current. The decrease of residence times for higher field strengths is visible, but not as strong as the pressure dependence, coinciding with previous measurements by (Moreau, 2016). The ion current dependence is relatively strong, however. Again, the step-off values are comparable to the step-on values, except for one data point for $\mathcal{E} = 2.2\,\mathrm{V/m}$, where the step-off value of 2.038(17) ms is lower than the step-on value of 2.54(14) ms.

In general, the mean residence times extracted from the step-off experiment are around 0.1 ms lower than the step-on values, which means they are mostly within their respec-

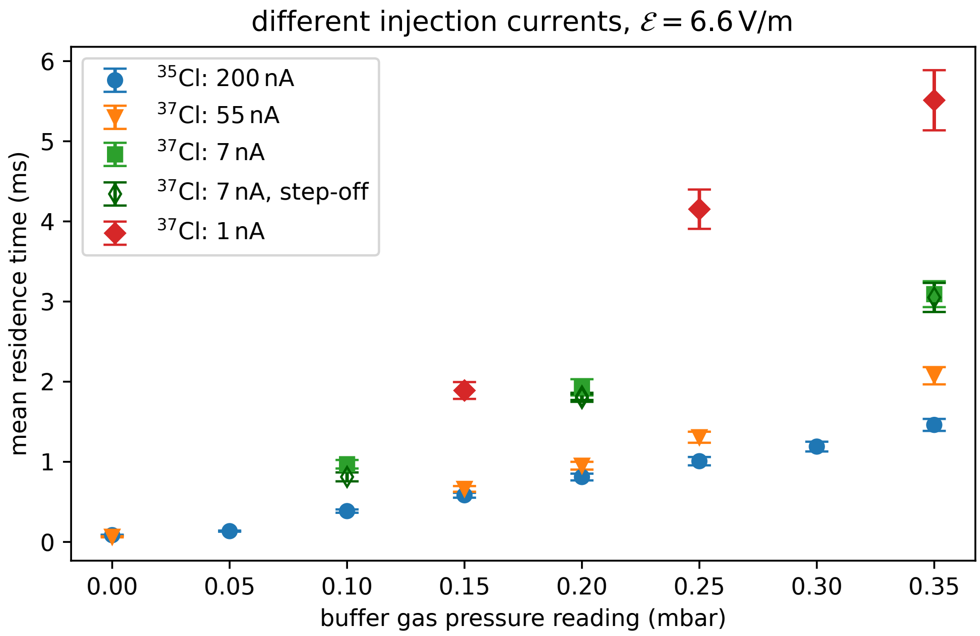

Figure 48: Mean residence time, depending on the buffer gas pressure reading (at the gas inlet) and injected current. Most values are from the step-on change experiment, and for comparison, some were obtained by the step-off experiment. The times obtained by $^{35}\mathrm{Cl}^-$ and $^{37}\mathrm{Cl}^-$ are comparable only with caution taken towards the different state that the cooler is initially in, as explained in Figure 46.

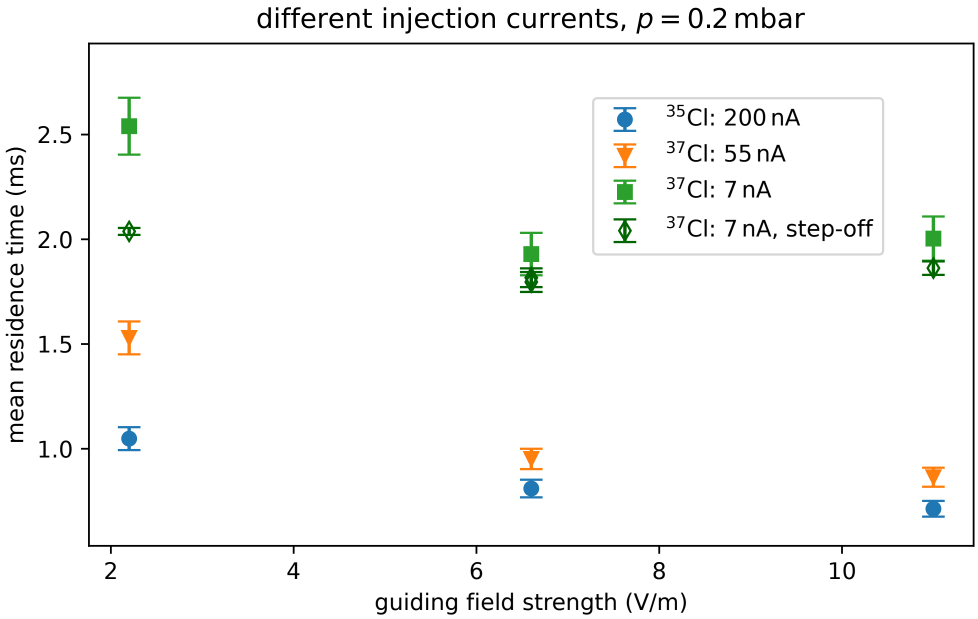

Figure 49: Mean residence time, depending on the guiding field strength and injected current. Values from both the step-on and step-off experiments are shown for comparison. A trend towards lower residence times for higher guiding field strength is visible, however the dependence is not as strong as for the buffer gas pressure.

tive uncertainties. This could be an indication that there is a dependence of the measured residence time on the current difference of the ion species. For the step-on experiment, the tracer species of $^{37}\mathrm{Cl}^{-}$ is injected into the densely filled cooler, which could lead to longer initial residence times than in the equilibrium state. On the other hand for the step-off experiment, the reverse would be true. This behaviour is observed, albeit only to a small degree.

7.3.2 Observation of space charge effects

Instead of loading the cooler with the tracer species and observing the current increase, the opposite was done to conduct a step-off experiment. Previous measurements by (Moreau, 2016), as shown in Figure 41, showed a strong dependence of the observed residence times firstly on the nature of the experiment (step-on or step-off), and secondly on the repetition frequency of the measurement. This dependence couldn't be reproduced. However, another interesting effect was observed, which is shown in Figure 50.

When the cooler was filled with $^{37}\mathrm{Cl}^{-}$ and a step change to $^{35}\mathrm{Cl}^{-}$ was introduced, an increase of the $^{37}\mathrm{Cl}^{-}$ signal was observed. This peak is not seen when the cooler is just unloaded and no $^{35}\mathrm{Cl}^{-}$ is injected afterwards.

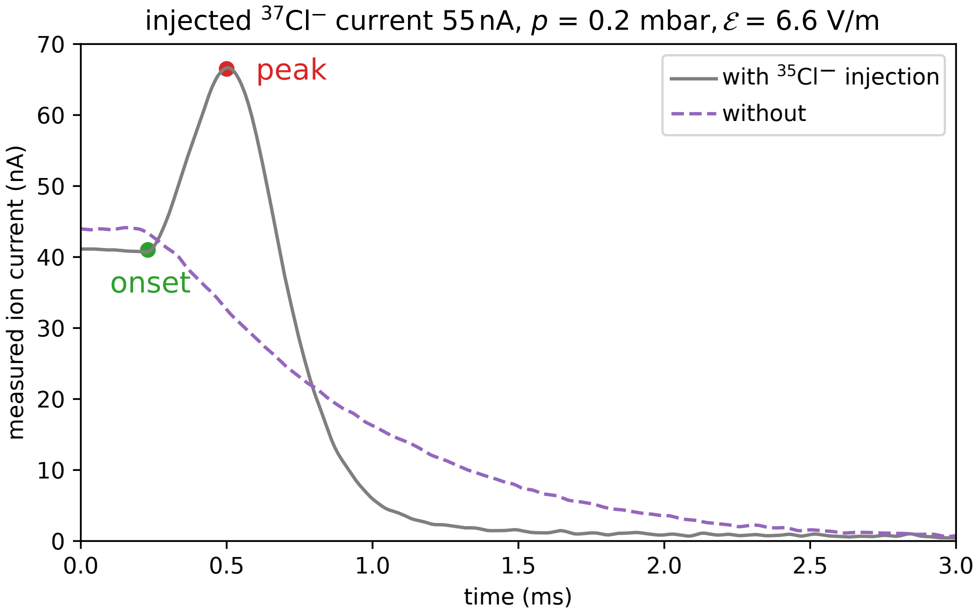

Figure 50: Step change from ^{37}Cl$^-$ to ^{35}Cl$^-$, observing the step-off of ^{37}Cl$^-$. The solid grey curve represents the situation with subsequent ^{35}Cl$^-$ injection, and the dashed purple curve shows "cooler unloading", i.e. no following ^{35}Cl$^-$ injection.

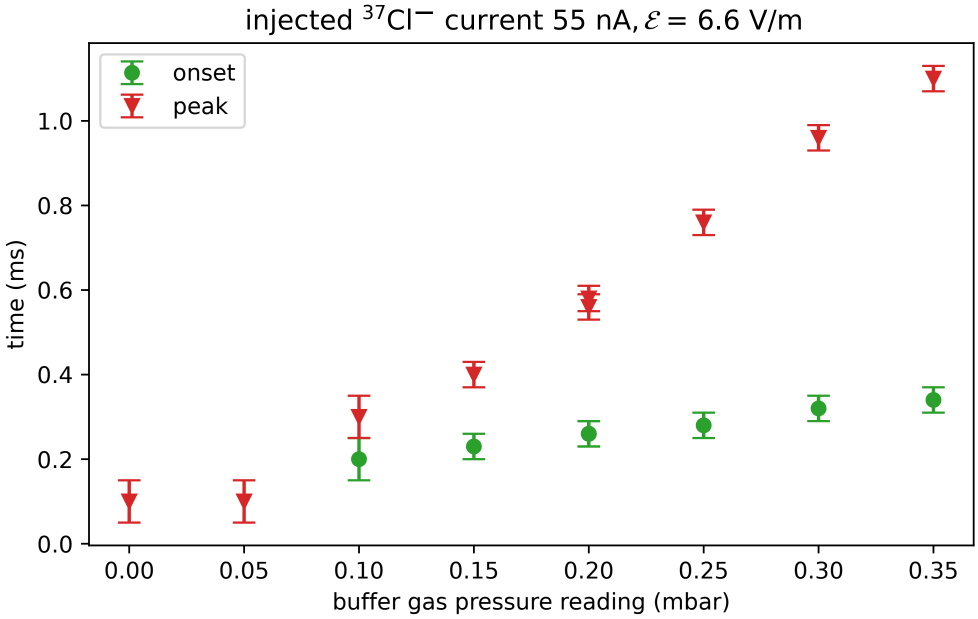

Figure 51: Dependence of the onset and peak of the curve shown in Figure 50 on the buffer gas pressure reading, exhibiting similar behaviour as the residence times shown in Figure 48.

The most probable explanation for this behaviour is the space charge effect of the higher current $^{35}\mathrm{Cl}^-$ beam pushing the $^{37}\mathrm{Cl}^-$ out of the cooler. As the onset of the current increase at around $t_0 = 240\,\mu\mathrm{s}$ (solid grey curve) almost coincides with the onset of the current decrease for the unloading case (dashed purple curve), t_0 could represent the time it takes for the space charge effect to traverse the cooler.

Traversing one cooler length of 1 m in t_0 corresponds to a speed of around 4200 m/s and varies with different cooler parameters. In Figure 51, the dependence of t_0 and t_{max} (the time of the peak) on the buffer gas pressure is shown. While t_{max} increases significantly with rising pressure, t_0 increases only slightly. This can be interpreted such that the space charge effects propagate (a little) slower for higher buffer gas pressures, as t_0 corresponds to the time it takes for the $^{37}\mathrm{Cl}^-$ output current to increase. On the other hand, t_{max} corresponds to the time when the current starts to decrease again and is thus similar to the minimum residence time.

The dependence of t_0 on the guiding field strength is negligible, and t_{max} decreases only slightly (around 0.15 ms) when increasing $\mathcal{E}$ from 2.2 to 11 V/m.

One has to note that the curves in Figure 50 don't correspond anymore to $1 - \mathrm{CDF}(t)$, because the equilibrium condition of $Q_{\mathrm{out}} = Q_{\mathrm{in}}$ isn't given for all times, but only for $t \leq 0$. This means that they must be interpreted differently (e.g. by observing t_0 and t_{max}); still, the integral over the curve is of interest. It corresponds to the number of tracer ions inside the cooler at $t = 0$, which is representative of the cooler condition for $t \leq 0$ (before changing the injected ion species), where an equilibrium is being held. Thus, the integrals of the observed washout functions correspond to the mean residence time before switching the tracer off, regardless of the shape of the observed curve (and the observed space charge effects). The change of this shape is considered in section 7.3.3.

Normally, the ion beam is tuned for high transmission such that it completely fits through the cooler injection aperture (in the ideal case). An ion beam centred on the aperture thus yields the highest current through the cooler, while a beam with the same parameters, but off-centre, gives less current.

This idea can be exploited considering the 3:1 abundance ratio of $^{35}\mathrm{Cl}$ and $^{37}\mathrm{Cl}$, which normally results in an ion beam current ratio of 3:1. To reach a different ratio of ion beam currents (e.g. 1:1), one can inject the $^{35}\mathrm{Cl}^-$-beam off-centred so that less current is injected into the cooler. For example, if the magnet is set to let through $^{35}\mathrm{Cl}^-$, applying a voltage to the normally grounded magnet chamber will deflect the $^{35}\mathrm{Cl}^-$ beam from the injection aperture centre and lower the $^{35}\mathrm{Cl}^-$ current entering the cooler.

In the case of this step-off experiment, one can apply this technique to lower the current of ^{35}Cl^{-} following the injection of ^{37}Cl^{-}, and thus “lower the bump” in Figure 50. There could be other ion optical effects caused by off-centre injection, which are neglected here.

By detuning the MBS voltage from the optimum towards either side, the pushing effect diminishes more and more, which is shown in Figure 52. Interesting to note are two cases: The dashed purple line was obtained with no follow-up beam of ^{35}Cl^{-}, which is comparable to the measurements by (Moreau, 2016) and essentially represents the case of “cooler unloading”, with a long tail of ions leaving the cooler quite late.

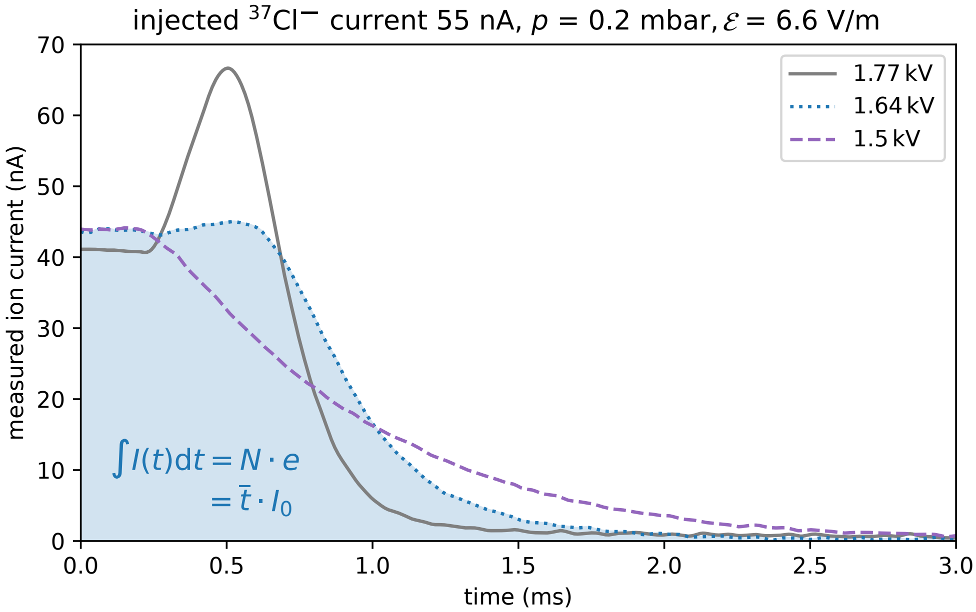

Figure 52: Step change from ^{37}Cl^{-} to ^{35}Cl^{-}, observing the unloading of ^{37}Cl^{-}. Lower MBS voltages represent lower following ^{35}Cl^{-} current, and thus a less pronounced space charge effect. Also shown is the integral under the dotted blue curve, corresponding to the cooler inventory.

In the other case of the dotted blue line, the ^{35}Cl^{-} beam current is almost equal to the one of ^{37}Cl^{-}, leading to an equilibrium situation for all times. The resulting curve looks like a washout function shown in section 1.3, neglecting a slight bump at around 0.5 ms, and can be derived to obtain the actual RTD, which is shown later.

The integral under the measured curve corresponds to the cooler charge inventory $N \cdot e$, which is plotted in Figure 53 for all measured MBS offset voltages. The values are scattered but within their respective uncertainties. The mean cooler inventory for all MBS detuning voltages is $\overline{N} = 272(11) \times 10^6$.

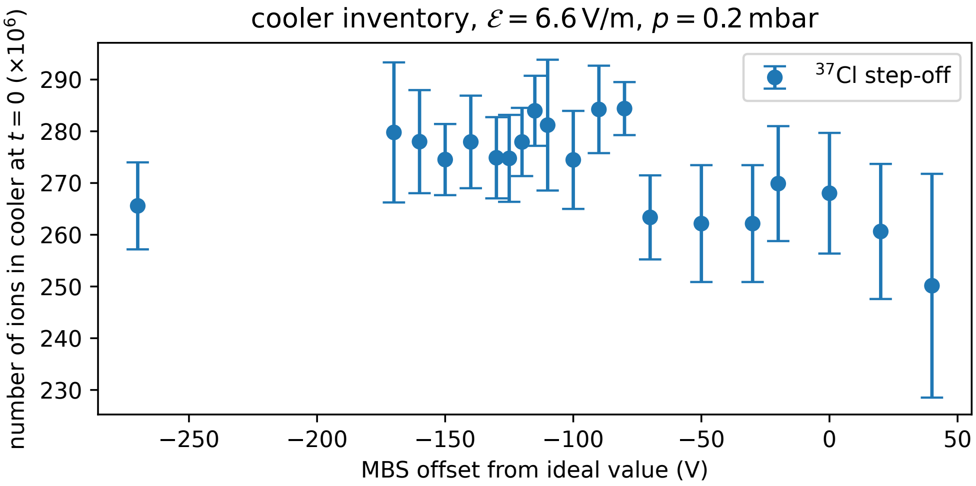

Figure 53: For a step-off experiment with ^{37}Cl$^-$ as the tracer, the cooler inventory, i.e. the number of ions in the cooler at $t = 0$, is plotted for several detuned MBS voltages (non-ideal injection of ^{35}Cl$^-$), as calculated by formula (10). The ideal MBS voltage of 1.77 kV is in this plot labelled as 0, and represents the normal case of 3:1 ion beam current ratio of ^{35}Cl$^-$ and ^{37}Cl$^-$. The mean value is $\overline{N} = 272(11) \times 10^6$.

The cooler inventory is in turn proportional to the equilibrium mean residence time, as explained in section 1.3. An additional, inverse dependency on the initial current I_0, which varied between measurements, facilitates the need for separate plots. In Figure 54, three methods to calculate the mean residence time are compared. They lead to somewhat different results, with the step experiments yielding comparable residence times of around 1 ms, while the pulse experiment gives a longer result of 1.4 ms.

To further demonstrate the difference between step and pulse experiments, residence time distributions obtained by the three measurement methods are compared, see Figure 55.

While the curves obtained by the step change experiments agree, the pulse experiment exhibits a shift to longer residence times, which was observed at various cooler settings. This shift is likely due to the non-equilibrium state of the cooler during pulsed injection: The continuous injection of ^{35}Cl$^-$ into the cooler is interrupted for 207 μs to inject the lesser-current ^{37}Cl$^-$, with no current injected for a total of 24 μs. This could lead to a behaviour more similar to a lower overall current, and thus longer residence times, hence the shift of the RTD towards longer times.

Consider the step-on experiment, which was carried out with the 3:1 current ratio of ^{35}Cl$^-$ (equilibrium in cooler) and ^{37}Cl$^-$ (tracer). One can only measure a signal, once the ^{37}Cl$^-$ ions have traversed one cooler length. Thus, if there is an effect of the different injection currents, it still only will be visible after the minimum residence time,

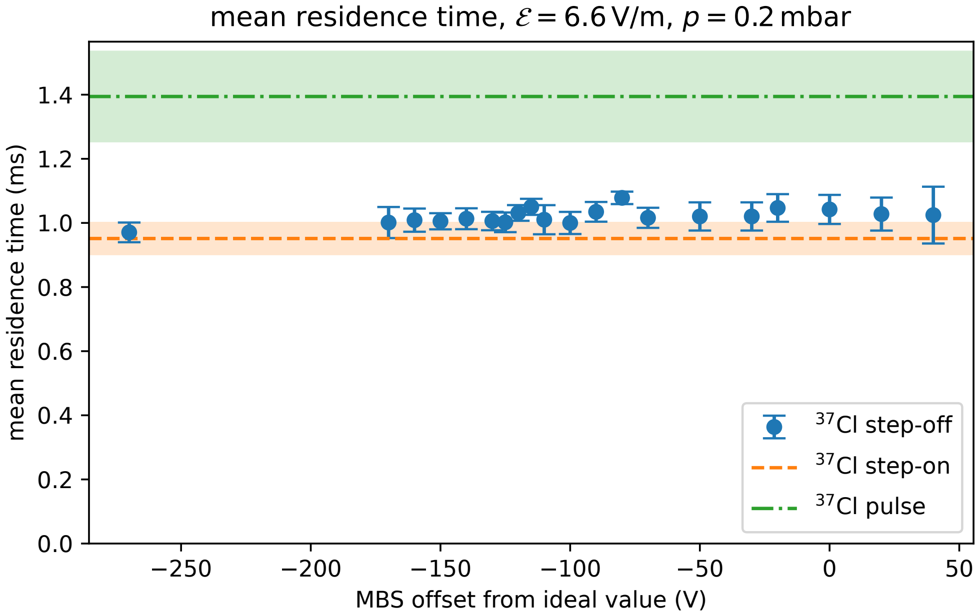

Figure 54: Mean residence times of a 55 nA beam of ^{37}Cl$^-$, obtained by three different methods: Step-off (washout function), step-on (CDF), and pulsed injection. For the step-off experiment, several values obtained by "non-ideal" injection (detuned MBS voltage) are plotted, with the value of −130 V representing an almost equal injection current. The other experiments were not performed at detuned MBS voltages, so a line shows the measured value, with the pale area indicating the uncertainty. The mean residence time seems to be quite independent of the ^{35}Cl$^-$ current.

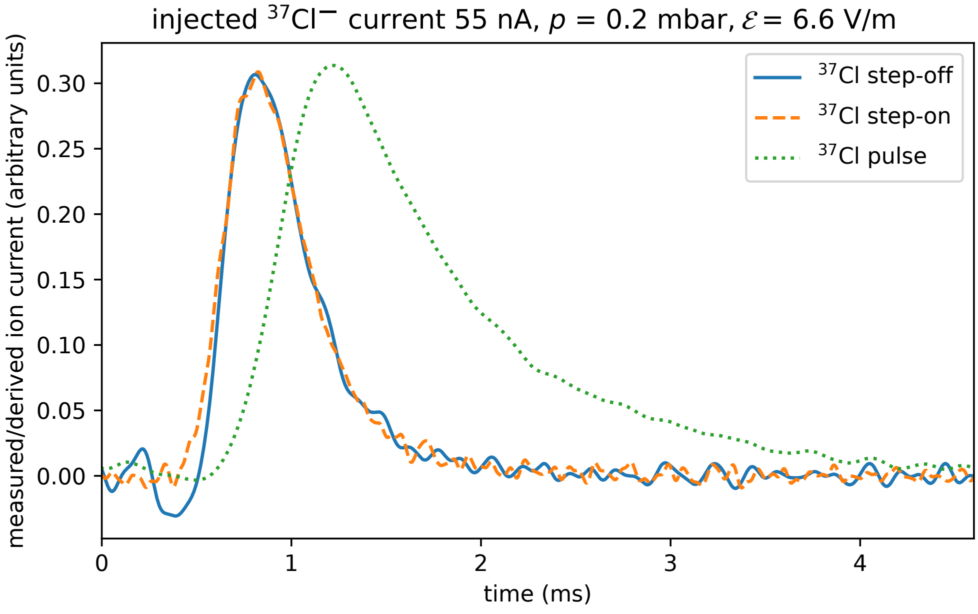

Figure 55: Comparison of residence time distributions obtained with the three measurement methods. All were conducted at the same cooler parameters and beam current. For the step-off change, the MBS was detuned to inject an equal current of ^{35}Cl$^-$ after the tracer beam of ^{37}Cl$^-$, i.e. shown here in solid blue is the derivative of the dotted blue curve in Figure 52. For the step-on change, the orange dashed curve from Figure 47 is shown.

not like the bump in the step-off experiment. Thus, the fact that step-on and step-off experiments agree, regarding the RTD, means that the space charge effects experienced by $^{37}\mathrm{Cl}^-$ in the densely filled cooler are not measurable at the exit. Apparently, it takes less than one residence time for a new equilibrium to be formed, and one can thus assume an equilibrium for the step-on experiments for $t > 0$ as well as $t \leq 0$. The derived RTDs shown in Figure 47 are thus a reliable representation of the actual distribution of residence times.

All mean residence times obtained by step experiments are shown in Table 7 in the Appendix.

7.3.3 Weighted mean residence time

The step-off experiment of $^{37}\mathrm{Cl}^-$ revealed a washout function that changes its shape towards longer times when less $^{35}\mathrm{Cl}^-$ current was injected afterwards. The equilibrium mean residence time calculated from it, as shown in the previous section, only takes into account the area under the washout function (which didn't change), not its shape. To quantify this effect, one can use the weighted mean residence time, defined in equation (13), and applied here as $\int t \cdot I(t)\,\mathrm{d}t/(I_0 \cdot \bar{t})$.

In Figure 56, the calculation of the weighted mean residence time is visualised. The lower bound of the integral is the onset $t_0 = 240\,\mu\mathrm{s}$. This shifts the resulting time only by a fixed amount but accounts for the fact that until this point, no ion having left the cooler carries effects from the change of the space charge density. Only after t_0, these effects are observed at the exit, which represents a good starting point for the weighted integral.

The resulting weighted mean residence times are plotted in Figure 57 over the MBS offset voltage. A decrease in $\bar{t}_\mathrm{w}$ can be seen with increasing $^{35}\mathrm{Cl}^-$ injection current, i.e. with increasing space charge effect. This can be interpreted in general as the reducing effect the space charge has on ion residence times inside the cooler.

7.3.4 Equilibrium mean residence time estimation from Moreau, 2016

The cooler inventory and thus the equilibrium mean residence time is almost constant for different MBS detuning voltages, as shown in Figure 54. As a result, a mean residence time can be extracted by integrating over the washout function even from a measurement where equilibrium is only given for $t < 0$, i.e. before the injected ion species is changed.

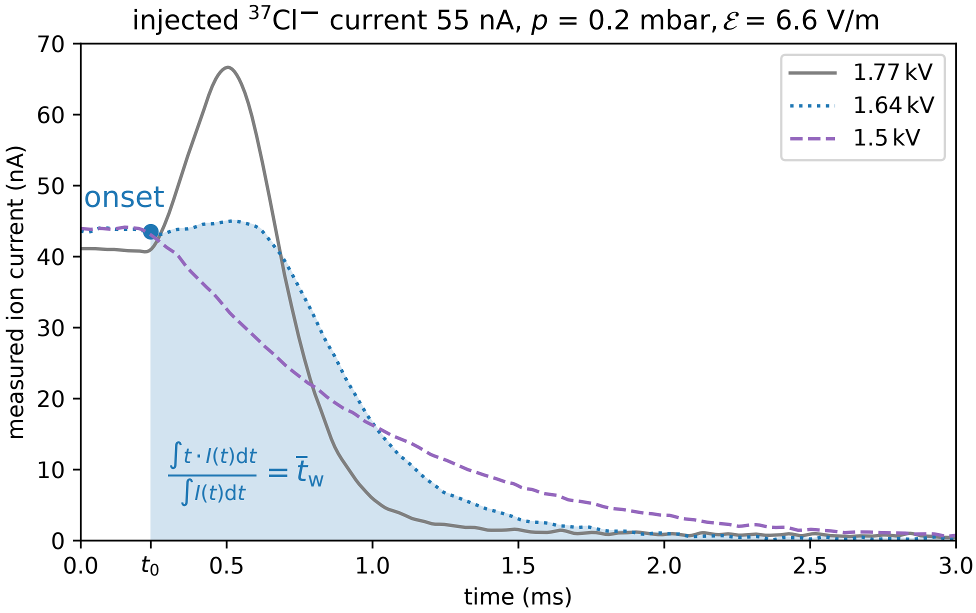

Figure 56: Step change from ^{37}Cl$^-$ to ^{35}Cl$^-$, observing the unloading of ^{37}Cl$^-$. The observed curve shifts towards longer times for a more offset ^{35}Cl$^-$ beam (i.e. lower MBS voltage), resulting in a longer residence time of the residual ^{37}Cl$^-$ ions, and quantified by $\bar{t}_\mathrm{w}$. The integration starts at the onset of the current increase, t_0.

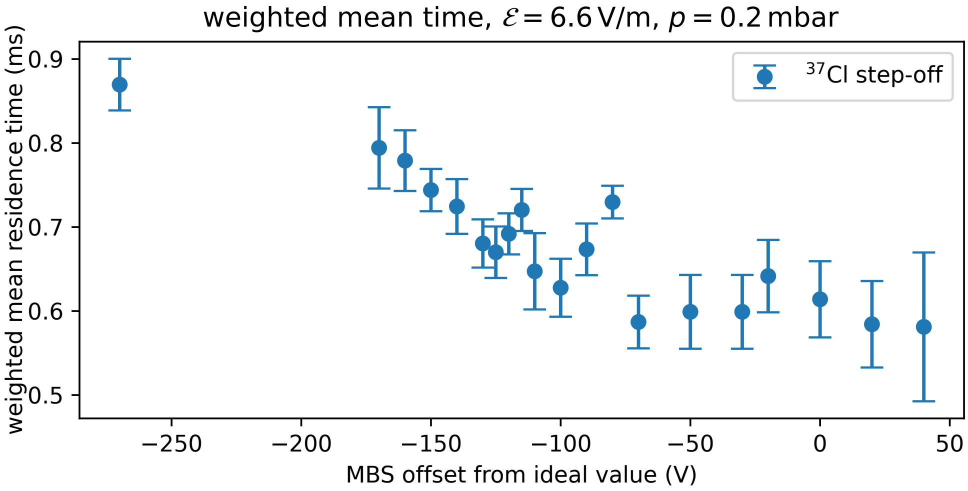

Figure 57: For a step-off experiment with ^{37}Cl$^-$ as the tracer, the weighted mean time is shown, i.e. the integral $\int t \cdot I(t)\mathrm{d}t/(I_0 \cdot \bar{t})$. A decrease of $\bar{t}_\mathrm{w}$ with increasing ^{35}Cl$^-$ injection current can be seen.

This in turn means that equilibrium mean residence times can be calculated from the measurements by (Moreau, 2016), which was done for some cooler parameters as shown in Figure 58.

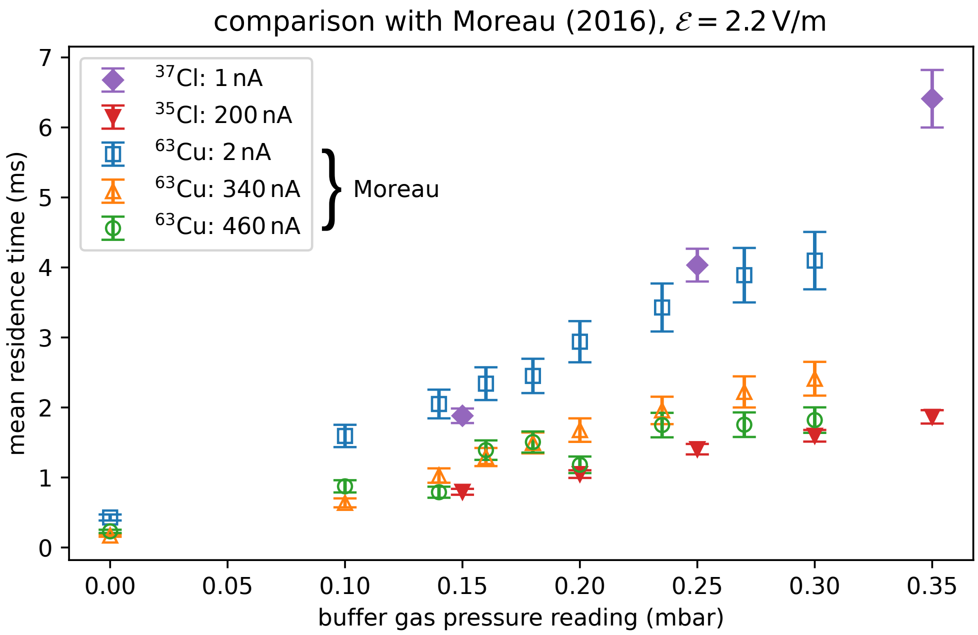

Figure 58: Comparison of equilibrium mean residence times obtained by step change experiments with $^{35}\mathrm{Cl}^-$ and $^{37}\mathrm{Cl}^-$ with calculated ones from raw data by (Moreau, 2016), where $^{63}\mathrm{Cu}^-$ was used as a tracer. The displayed current is the injected ion beam current, but transmission through the cooler is lower for $^{63}\mathrm{Cu}^-$, so the effective current in the cooler is comparable between Moreau's and own measurements. The mean residence times agree to some extent, but especially for high currents, residence times from Moreau are longer than own measurements.

The main difference in the measurement method is the cooler transmission, which only reaches 30 to 50 % with $^{63}\mathrm{Cu}^-$, cf. (Martschini et al., 2019). For Cl^-, the transmission is in the range of 80 %. To be able to compare results from the different experiments, one has to consider the effective current within the cooler. In this sense, the 200 nA injected $^{35}\mathrm{Cl}^-$ current from this measurement is actually comparable to 340 to 460 nA injected $^{63}\mathrm{Cu}^-$ current from Moreau, so the equilibrium mean residence times should normally match. Similarly, the cooler situation with an injected $^{37}\mathrm{Cl}^-$ current of 1 nA should match that of 2 nA injected $^{63}\mathrm{Cu}^-$ current.

The mean residence times for low currents are comparable, but the 340 nA values from (Moreau, 2016) are systematically 40 to 50 % larger than the measurements of this thesis, while the 460 nA values are scattered between both. A possible factor could be a mass dependence of residence times, as the almost twice-as-heavy isotope of $^{63}\mathrm{Cu}^-$ was used by (Moreau, 2016). This dependence is discussed in section 7.6.

7.4 Discussion

Some of the observations by (Moreau, 2016) can be confirmed, such as the injection current having the biggest influence on cooler residence time, followed by buffer gas pressure, while the guiding field strength shows the least influence.

However, the effects of the injection frequency on the residence time distribution (RTD), as well as the long tails observed by (Moreau, 2016) could not be reproduced. A more compact RTD was observed instead, which also can be confirmed by multiphysics simulations of the cooler (Baumgartner, 2024). Using both the step change and pulse experiment approach, this experiment could more confidently quantify the equilibrium mean residence time, as well as the shape of the residence time distribution, at different cooler parameters.

The step experiments were designed such that the injected ion species was changed e.g. from $^{35}\text{Cl}^-$ to $^{37}\text{Cl}^-$ at a specific time, defined as $t = 0$. Using a Wien filter, the outgoing ion beam current of one of the species was observed. If for example the Wien filter was set to $^{37}\text{Cl}^-$, the current started to rise with some delay after $t = 0$, reaching its maximum after all initially injected ions had propagated through the cooler, i.e. after the maximum residence time. This experiment is then called a step-on experiment. For the step-off experiment, first $^{37}\text{Cl}^-$ was injected, and at $t = 0$ a switch to $^{35}\text{Cl}^-$ was introduced, with the $^{37}\text{Cl}^-$ current decrease being monitored behind the Wien filter.

Generally, it is favourable to observe an equilibrium situation of $Q_{\text{out}} = Q_{\text{in}}$, as this not only is a requirement for the theoretical description but also represents the actual usage of the cooler. This equilibrium condition was fulfilled for all experiments, including the ones by (Moreau, 2016), up until the injected ion species was changed, i.e. for $t \leq 0$. For the step experiments, a mean residence time of the situation before $t = 0$ was thus calculated from the measurements. For the step-off experiment with a 1:1 injection current ratio, an equilibrium for $t > 0$ was given, and the shape of the RTD could be extracted.

Regarding the latter, figures 54 and 55 show that more trust can be placed in the step-change experiments, than in the pulse experiment. The step-off of $^{37}\text{Cl}^-$ was conducted with a changing injection current of the following $^{35}\text{Cl}^-$. Even though the latter was varied between 0 and 300 % of the previously injected $^{37}\text{Cl}^-$ current, little change was observed in the cooler inventory and thus the mean residence time. A detuning of the MBS voltage until the injection current of both isotopes was equal could reproduce the ideal equilibrium situation for all times. This led to a confident estimation of the corresponding RTD, shown in Figure 55. Its shape closely matches the RTD obtained by the step-on experiment. This implies that even though the step-on experiments were performed with the 3:1 injection currents of $^{35}\mathrm{Cl}^-$ and $^{37}\mathrm{Cl}^-$, the ions spend enough time in the cooler so that a new equilibrium is established. Thus, the derived RTDs shown in Figure 47 are a good representation of the equilibrium situation in the cooler.

A possible explanation for the disagreement between step change and pulse experiments is that for the pulse experiment, there is a longer overall pause of injection, as the MBS has to be switched back and forth within 207 µs. This corresponds to an injection dead time of around 10 % in that phase, making the situation in the cooler more comparable to lower injection currents, where longer residence times would be observed, which is actually the case. Followingly, no residence times from the pulse experiments were calculated. However, this method proved worthy of having a comparison with the other methods.

Figure 51 shows a dependence of the bump onset t_0 of the washout function on the buffer gas pressure, similar to, but much shorter than the mean residence time. The time t_0 can be seen as the time it takes for an intense ion beam to push ions within the cooler to the extraction lens. The space charge effect thus propagates much faster through the cooler than the ions themselves. The fact that this time also depends on the buffer gas pressure gives some insights into the physics happening inside the cooler, as also discussed by (Baumgartner, 2024) using multiphysics simulations of the ion cooler.

If the buffer gas pressure is low, the mean free path is longer, i.e. individual ions travel further before they interact with other particles. The mean overall ion velocity inside the cooler points in the positive z direction (towards the exit), so a longer mean free path results in the ions generally moving more easily towards the cooler exit. If an additional acceleration away from the entrance is present, such as the more intense ion beam of $^{35}\mathrm{Cl}^-$ entering the cooler and repelling the ions within, this effect increases.

This repelling potential moves faster through the cooler than the ions, which can be explained when comparing an individual ion's z-velocity v_z with its absolute velocity v, as shown by (Baumgartner, 2024). Averaged along the individual ions' paths, v is much larger than v_z, because the ion scatters around the cooler, gaining speed, hitting other particles and thus slowing down again. The momentum transfer to other particles is how the effect of space charge propagates, so for a longer mean free path, the space charge effectively has a longer reach, and can thus propagate faster through the cooler. For a smaller mean free path, i.e. higher buffer gas pressure, there are more collisions per time unit, thus the ions can only travel shorter distances, and the space charge effect propagates slower.

The space charge effect appears in the step-off measurement of $^{37}\mathrm{Cl}^-$ as the shift of the whole distribution towards shorter times for a higher subsequent $^{35}\mathrm{Cl}^-$ injection current. This shift was quantified by calculating a weighted mean residence time $\bar{t}_\mathrm{w}$. In Figure 57, $\bar{t}_\mathrm{w}$ is plotted over the MBS detuning voltage, which changed the $^{35}\mathrm{Cl}^-$ injection current following the step-off of $^{37}\mathrm{Cl}^-$. The decrease of $\bar{t}_\mathrm{w}$ with increasing $^{35}\mathrm{Cl}^-$ current is a direct representation of the reducing effect of space charge on ion residence time, induced by the continuous injection of ions into the cooler.

At last, equilibrium mean residence times were calculated from measurements by (Moreau, 2016). They show a similar dependence on the buffer gas pressure as own measurements, but especially at high injection currents, the residence time is longer for the $^{63}\mathrm{Cu}^-$ ions used by Moreau. This effect might be mass-dependent and is explored in section 7.6.

7.5 Uncertainty estimation

The uncertainty of the numerical integration was quantified for an uncertainty estimation of the mean residence time, as shown in section 1.3.

The scattering of the actual measurements around the weighted mean average, as shown in Figure 45, is taken into account for the uncertainty propagation in the form of the standard deviation σ_i for each time step i. The integration consists of summing over all time steps and multiplying by the time step size. Using the Gaussian formula for uncertainty propagation, this translates to an uncertainty of $\bar{t}$:

$$\mathrm{u}(\bar{t}) = \Delta t \sqrt{\sum_{t=0}^{t_\mathrm{max}} \sigma_i^2} \tag{30}$$

This value only takes into account statistical variation between the individual signals, but there is additional ambiguity in the data evaluation. One has to choose a voltage offset where the signal is considered zero (either on the SRS or in the analysis), which is different for each amplification setting. Furthermore, the maximum signal intensity I_0 has to be averaged over a time range as well, as the signal is normalised to this value for integration.

An additional relative uncertainty of 5 % was added, to account for the ambiguity in the choice of these time ranges. They were carefully selected for each measurement (and are shown in Figure 67 in the Appendix), but some subjectivity always remains. This approach is used for all values measured with a positive step change experiment, as well as the measurements by (Moreau, 2016).

For the negative step change experiments, only one measurement was done for each MBS voltage. Thus, no statistical σ for each time step could be defined, and instead the signal at $0 < t < 0.2$ ms was considered. Here, the current is relatively constant and is defined as I_0. The standard deviation of the current around I_0, which is proportional to the signal noise, was used as the first term of uncertainty.

In this particular experiment, the current from the source was somewhat unstable, so another uncertainty arises from the instability of I_0, as the residence times vary with the current. This error from normalizing the signal is calculated as the normalised difference of I_0 from the value $\overline{I_0}$ averaged over all MBS voltages:

$$I_{\text{norm}}(t) = \frac{I(t)}{I_0} \tag{31}$$

$$\mathrm{u}(I_{\text{norm}}) = \frac{I_0 - \overline{I_0}}{\overline{I_0}} \tag{32}$$

7.6 Other possible isotopic systems for mass-dependent effect

Other than space charge effects, ion movement inside the cooler is largely diffusion-dominated (Baumgartner, 2024). The diffusion coefficient, known from Fick's laws, is inversely proportional to the square root of the reduced mass of ions and buffer gas atoms, i.e. $D \sim 1/\sqrt{m_{\text{r}}}$ (Chapman & Cowling, 1970). This means in turn that heavier ions spread slower if governed by diffusion. But also due to space charge effects, the movement would be slower for heavier particles, which could in effect lead to longer residence times for heavier ions. Recent simulations with COMSOL® confirm this effect (Baumgartner, 2024), which was possibly observed in the measurements shown in section 7.3.4.

A proposed follow-up experiment to quantify the mass-dependence of ion residence times would be to use a different target element with matching isotopic abundances but in different mass ranges. In Table 4, some of these elements are shown, which could be used in a similar experiment as in this thesis. Similar to this thesis, the reduction of the more abundant isotope's beam current, by detuning the MBS, is a possibility to balance the beam currents of two isotopes. However, non-centred injection into the cooler could have other ion optical effects, so a closely matching current of the individual isotopes is favourable.

Table 4: Possible systems with two or more similarly abundant isotopes. Next to the individual abundances (Soti et al., 2019), their ratios are shown, close to 1 being a good measure. A rough, order-of-magnitude estimate for the achievable current is given, taken from (Middleton, 1989). Highlighted in grey are especially promising candidates at low, medium and high mass ranges.

	mass (amu)	abundance (%)	abundance ratio	current (μA)
Silicon	29 30	4.67 3.1	**0.664**	10
Chlorine	35 37	75.77 24.23	0.320	100
Bromine	79 81	50.69 49.31	0.973	30
Molybdenum I	95 96	15.92 16.68	0.954	0.15
Molybdenum II	97 100	9.55 9.63	0.992	0.1
Silver	107 109	51.839 48.161	**0.929**	50
Tungsten	184 186	30.67 28.6	0.933	1
Platinum	194 195	32.9 33.8	**0.973**	100

After finding elements with similarly abundant isotopes in (Soti et al., 2019), information about the creation of negative ions from them in a SNICS was gathered (Middleton, 1989). For example, magnesium has two similarly abundant isotopes, but cannot form elemental anions, so it wasn't included here.

Similarly, Bromine would be a great candidate abundance-wise, but the commonly used sample material KBr is hygroscopic, so $^{79}\text{BrH}_2^-$ could be coinciding with $^{81}\text{Br}^-$. A particular emphasis was thus laid on elements with a low hydride signal.

Still, there could be background current from other molecular isobars, which would have to be further investigated. Transmission through the cooler is another factor that would need to be addressed, as this would affect the comparability of the data.

Three systems look particularly promising, as they have a relatively high achievable current from the ion source (over 10 μA), a close-to-one abundance ratio, and lie in different mass ranges: Silicon with $^{30}\text{Si}/^{29}\text{Si} = 0.664$ (which is twice as close to 1:1 as chlorine), silver with $^{109}\text{Ag}/^{107}\text{Ag} = 0.929$, and platinum with $^{194}\text{Pt}/^{195}\text{Pt} = 0.973$. All three are easy to chemically prepare and press into a sample holder, can give high elemental currents, and show a low hydride current.

8 Conclusion and outlook

This work aimed at building a new multi-beam switcher (MBS) for the Vienna Environmental Research Accelerator (VERA) and integrating it into the existing setup for Ion-Laser InterAction Mass Spectrometry (ILIAMS). Furthermore, the new MBS should be used to measure ion residence times inside the ILIAMS cooler, as well as to observe space charge effects.

In the first part of this work, the phase space of various ion beams was measured and evaluated. Previous measurements lacked a systematic approach, as well as some technical elements required for precise results, i.e. two movable slits, which were now available. The results presented here show that there is a strong dependence of the phase space on the sputtering history of the target. Fresh carbon targets gave a highly astigmatic beam at high currents, with the waist in x and y directions almost half a meter apart. For long-sputtered targets, the beam waist coincides better in the x and y direction, leading to better transport through the beamline and injection into the cooler. This effect is also dependent on the target material, with carbon being a worse candidate for fresh targets than fluorine.

Based on the phase space measurements, simulations were conducted to characterise the ion optics of the cooler injection beamline. They showed that the injection ion optics are the main obstacle to reaching optimal cooler transmission. Due to the varying phase space of the ion beam leaving the source, this could only be overcome by a quadrupole lens, which was implemented in the simulations as an electrostatic quadrupole, based on an existing beam steerer. The transmission of a $^{12}\mathrm{C}^-$ ion beam based on the phase space measurements was shown to increase from 40 to 61 % with an optimised quadrupole voltage.

This setup could be implemented at VERA with minimal work on the beamline, and a quadrupole tuning step required at least once during the lifetime of one target. The resulting increase in measurement time would be in turn reduced by higher cooler transmission and thus higher count rate, as well as using the multi-beam switcher for fast sequential injection of different isotopes. This would make accelerator mass spectrometry measurements with the ILIAMS system faster and more efficient overall, and probably increase the precision through a more reproducible cooler injection.

The simulations were also performed to prepare the design of a new MBS. The importance of the existence, rather than the shape of electrodes protruding from the magnet chamber into the beamline was characterised. This helped in overcoming the obstacle of very tight space constraints, as the electrode length could be fitted to the available space. A setup with short bellows, custom-made electrodes and PEEK insulators was devised and subsequently built, held together by nylon screws.

After simulations were concluded, the MBS was built and integrated into the existing ILIAMS cooler injection beamline at VERA. The space constraints made it challenging to place the electrodes properly inside the insulator and bellows, but after careful alignment, the magnet chamber holds a vacuum of $\sim 2 \times 10^{-8}$ mbar with two turbopumps in operation next to it.

The new MBS was then characterised for transmission and switching speed, showing good results in both. From simulations, it was expected that the use of the MBS would introduce a slight transmission decrease of up to 3 %. Measurements using a $^{35}\mathrm{Cl}^-$ beam showed a similar transmission decrease of 4 to 5 %.

Using the newly constructed setup, the residence time of chlorine ions inside the ILIAMS cooler was measured for different cooler parameters, recreating and partly verifying the results of (Moreau, 2016). The general trend of longer residence times with higher buffer gas pressure, lower guiding field strength and lower injection current was confirmed. In contrast, long tails of the residence time distribution (RTD) towards long residence times observed by Moreau were shown to emanate from shortcomings in the measurement method. A more robust estimation of the shape of the RTD, being more compact than observed by Moreau, was achieved in this work. Different experiments, namely step-on, step-off and pulsed injection were performed and compared, leading to a further quantification of equilibrium mean residence times for different cooler parameters.

Moreover, space charge effects inside the cooler were directly observed in a step-off experiment with $^{37}\mathrm{Cl}^-$ ions, which were pushed through the cooler faster than in equilibrium by the following, higher current $^{35}\mathrm{Cl}^-$ ions. Varying the injection intensity of the latter made it possible to rate the quality of the step change experiments as being robust against a difference in isotopic abundance.

The observations also confirm a leading theory that the space charge effects of a changing current propagate fast through the cooler (up to 240 μs for one cooler length), with a new equilibrium taking less than one residence time to form.

The re-evaluation of measurements by (Moreau, 2016) yielded a more robust estimation of equilibrium mean residence times of $^{63}\mathrm{Cu}^-$. When compared to the measurements of $^{35}\mathrm{Cl}^-$ and $^{37}\mathrm{Cl}^-$ performed by the author, longer residence times of the copper isotope were observed, which indicates a mass dependent effect.

In the future, the effect of ion mass on residence times could be further quantified in a follow-up experiment involving different target materials. Three systems are proposed, using silicon, silver and platinum isotopes with a closely matching abundance. As they cover a broad mass range from 29 to 195 amu, the influence of ion mass on the residence time could be experimentally quantified.

References

aviva metals. (2023). OFHC copper characteristics. Retrieved from `https://www.avivametals.com/products/c10200-oxygen-free-copper`

Banford, A. (1966). *The transport of charged particle beams*. New York: Spon.

Baumgartner, D. (2024). *Simulating space charge effects inside the ILIAMS ion cooler*. Master's thesis, University of Vienna, unpublished.

Brumby, A. (2008). Silver, silver compounds, and silver alloys. *Ullmann's Encyclopedia of Industrial Chemistry*. Retrieved from `https://doi.org/10.1002/14356007.a24_107.pub2`

Chapman, S., & Cowling, T. (1970). *Mathematical theory of non-uniform gases* (3rd ed.). Cambridge University Press.

COMSOL AB, S., Stockholm. (2021). COMSOL Multiphysics® v. 6.0. Retrieved from `www.comsol.com`

Conte, M., & Mackay, W. W. (2008). *An introduction to the physics of particle accelerators (2nd edition)*. Singapore: World Scientific Publishing Company.

Courant, E., & Snyder, H. (1958). Theory of the alternating-gradient synchrotron. *Annals of physics*, *3*(1), 1–48.

Danckwerts, P. (1953). Continuous flow systems: Distribution of residence times. *Chemical Engineering Science*, *2*(1), 1-13. Retrieved from `https://www.sciencedirect.com/science/article/pii/0009250953800011`

Danfysik A/S, D., Taastrup. (2015). Probably the best magnet technology you can buy. Retrieved from `https://www.danfysik.dk/media/1106/magnet-technology.pdf`

Direct Plastics. (2013). Why engineering plastics outgas and why should you care. Retrieved from `https://www.directplastics.co.uk/news/why-engineering-plastics-outgas-and-why-should-you-care`

Edwards, D. A., & Syphers, M. J. (2008). *An introduction to the physics of high energy accelerators*. New York: John Wiley & Sons.

Flannigan, E. (2024). *Installation and testing of the Isobar Separator for Anions at the A. E. Lalonde AMS laboratory using chlorine-36 analysis*. PhD thesis, University of Ottawa.

Gaggl, P. (2021). *Multiphysics simulation of negative ions in a gas filled RF-quadrupole*. Master's thesis, University of Vienna.

Hinterberger, F. (2008). *Physik der Teilchenbeschleuniger und Ionenoptik*. Wiesbaden: Springer Berlin Heidelberg.

Holzer, B. (2013). Introduction to transverse beam dynamics. *Proceedings of the CAS-CERN Accelerator School: Superconductivity for Accelerators*.

Kutschera, W. (2013). Applications of accelerator mass spectrometry. *International Journal of Mass Spectrometry*, *349-350*, 203-218. Retrieved from `https://www.sciencedirect.com/science/article/pii/S1387380613002091`

Kutschera, W., Jull, A. J. T., Paul, M., & Wallner, A. (2023, Sep). Atom counting with accelerator mass spectrometry. *Rev. Mod. Phys.*, *95*, 035006. Retrieved from `https://link.aps.org/doi/10.1103/RevModPhys.95.035006`

Kögler, C. (2014). *Standard-Einsatz-Regeln: Elektrischer Strom im Einsatz*. Landsberg: ecomed-Storck GmbH.

Lehr, J., & Ron, P. (2017). *Electrical breakdown in gases*. John Wiley & Sons, Ltd. Retrieved from `https://onlinelibrary.wiley.com/doi/abs/10.1002/9781118886502.ch8`

Levenspiel, O. (1998). *Chemical reaction engineering*. New York: John Wiley & Sons.

Litherland, A., Tomski, I., Zhao, X.-L., Cousins, L. M., Doupé, J., Javahery, G., & Kieser, W. (2007). Isobar separation at very low energy for ams. *Nuclear Instruments & Methods in Physics Research. Section B, Beam Interactions with Materials and Atoms*, *259*(1), 230–235.

Liu, Y., Beene, J., Havener, C., & Liang, J. (2005). Isobar suppression by photodetachment in a gas-filled RF quadrupole ion guide. *Applied Physics Letters*, *87*(11).

Lux, J. (1998). Rogowski profiles. Retrieved from `https://web.archive.org/web/20100617223746/http://home.earthlink.net/~jimlux/hv/rogowski.htm`

Manura, D. (2022). PA antimirroring in 8.1.1.32 - SIMION discussion group. Retrieved from `https://forum.simion.com/topic/2815-pa-antimirroring-in-81132/?do=findComment&comment=9266`

Manura, D., & Dahl, D. (2011). SIMION 8.1. Retrieved from `https://simion.com`

Martschini, M., Hanstorp, D., Lachner, J., Marek, C., Priller, A., Steier, P., . . . Golser, R. (2019, 04). The ILIAMS project – an RFQ ion beam cooler for selective laser photodetachment at VERA. *Nuclear Instruments & Methods in Physics Research. Section B, Beam Interactions with Materials and Atoms*, *456*. doi: 10.1016/j.nimb.2019.04.039

Martschini, M., Lachner, J., Hain, K., Kern, M., Marchhart, O., Pitters, J., . . . Golser, R. (2021, 09). 5 years of ion-laser interaction mass spectrometry - status and prospects of isobar suppression in AMS by lasers. *Radiocarbon*, *64*, 1-14. doi: 10.1017/RDC.2021.73

Martschini, M., Pitters, J., Moreau, T., Andersson, P., Forstner, O., Hanstorp, D., . . . Golser, R. (2017, 12). Selective laser photodetachment of intense atomic and molecular negative ion beams with the ILIAS RFQ ion beam cooler. *International Journal of Mass Spectrometry*, *415*. doi: 10.1016/j.ijms.2016.12.015

Middleton, R. (1989). *A negative-ion cookbook*. Department Of Physics, University of Pennsylvania: Philadelphia Unpublished.

Moreau, T. (2016). *Development and characterization of the Ion Laser InterAction Setup (ILIAS)*. Master's thesis, University of Vienna.

Nauman, E. (2003). Residence time distributions. In *Handbook of industrial mixing* (p. 1-17). John Wiley & Sons, Ltd. Retrieved from `https://onlinelibrary.wiley.com/doi/abs/10.1002/0471451452.ch1`

Nauman, E. (2008, 04). Residence time theory. *Industrial & Engineering Chemistry Research*, *47*. doi: 10.1021/ie071635a

Nave, C. (2017). Magnetic properties of ferromagnetic materials. Retrieved from `http://hyperphysics.phy-astr.gsu.edu/hbase/tables/magprop.html#c2`

Nawri, N. (2019). Berechnung von Kovarianzellipsen. Retrieved from `https://web.archive.org/web/20190814081830/http://imkbemu.physik.uni-karlsruhe.de/~eisatlas/covariance_ellipses.pdf`

Pitters, J. (2015). *Laser photodetachment in a gas-filled RF-quadrupole*. Master's thesis, University of Vienna.

Rogowski, W. (1923 and 1926). *Archiv für Elektrotechnik* (Volume 12 and 16 ed.).

Sammartano, S., et al. (2020). Outgassing rates of PEEK, Kapton®

and Vespel® foils. *CERN-ACC-NOTE-2020-0039*. Retrieved from `https://indico.cern.ch/event/1031708/contributions/4355322/attachments/2267727/3964487/Outgassing%20rates%20of%20PEEK%20Kapton%20and%20Vespel%20foils%20ATS%20NoteFinal.pdf`

Schiffer, M., Machhart, O., Priller, A., Herb, S., Hackenberg, G., Heinze, S., ... Dewald, A. (2022, 10). An advanced radio-frequency quadrupole ion cooler for accelerator mass spectrometry. *Nuclear Instruments & Methods in Physics Research. Section B, Beam Interactions with Materials and Atoms*, *528*, 27-33. doi: 10.1016/j.nimb.2022.07.010

Schillaci, F., Manura, D., et al. (2017). Importing a field map - SIMION discussion group. Retrieved from `https://forum.simion.com/topic/1577-importing-a-field-map/?do=findComment&comment=7406`

Soti, Z., Magill, J., & Dreher, R. (2019, 05). Karlsruhe nuclide chart – new 10th edition 2018. *EPJ Nuclear Sciences & Technologies*, *5*, 6. doi: 10.1051/epjn/2019004

Steier, P. (2000). *Exploring the limits of VERA: A universal facility for Accelerator Mass Spectrometry*. Dissertation, Universität Wien.

Wasserburger, P. (2018). *Simulation und Optimierung des Laser-Ionen-Aufbaus an VERA*. Diplomarbeit, Universität Wien.

Wollnik, H. (1987). *Optics of charged particles* (1st ed.). San Diego, London: Academic Press.

Appendix

Bash scripts to move `SLT S2-1`

The code can also be accessed at github.com/felix-albrecht/ionbeam.

Position control: `pos.sh`

```
#!/bin/bash
#Script to set the position of slitpair SLT S2-1
#by Felix Albrecht, March 2023

set_pos () {
  #1: new Slit position
  #2: x or y

  #set $now as current position
  freadxpar "L:Slt S2-1|${2}cPosR" now
  if [ $(echo "${now} > ${1}" |bc -l) -eq 1 ]
  then
    #if current position is greater that desired value, move left/down
    fsetpar "Slt S2-1|${2}cMovC" 1
    movein=1
  elif [ $(echo "${now} < ${1}" |bc -l) -eq 1 ]
  then
    #if current position is less that desired value, move right/up
    fsetpar "Slt S2-1|${2}cMovC" 3
    movein=0
  else
    break
  fi

  #calculate the estimated time (eta) to move the slits
  speed=0.08
  start=$(date +%s)
  eta=$(echo "($now - $1) / $speed" | bc -l)
  fin=$(echo "${eta#-} + $start" | bc -l)

  while [ $(echo "$now < $fin" | bc -l) -eq 1 ]
```

```
  do
    usleep 100000
    #get current position and output it
    freadxpar "L:Slt S2-1|${2}cPosR" current
    echo $current
    if [ $(echo "$current <= $1 && $movein" |bc -l) -eq 1 ]
    then
      #break out of loop if desired position is reached (too early)
      break
    elif [ $(echo "$current >= $1 && $movein==0" |bc -l) -eq 1 ]
    then
      #likewise, but for the other movement direction
      break
    fi
    #get current time
    now=$(date +%s)
  done
  #stop moving
  fsetpar "Slt S2-1|${2}cMovC" 0
}

#call the main function two times to get more accurate results
set_position () {
  set_pos $1 $2
  sleep 2
  set_pos $1 $2
}

. $SCRIPTDIR/scriptheader
#actual function call
set_position $1 $2
```

Distance control: `pos.sh`

```
#!/bin/bash
#Script to set the distance of slitpair SLT S2-1
#by Felix Albrecht, March 2023

set_dist () {
  #1: new Slit distance
  #2: x or y

  #set $now as current distance
  freadxpar "L:Slt S2-1|${2}dPosR" now
  if [ $(echo "${now} > ${1}" |bc -l) -eq 1 ]
  then
    #if current distance is greater that desired value, reduce
    fsetpar "Slt S2-1|${2}dMovC" 1
    movein=1
  elif [ $(echo "${now} < ${1}" |bc -l) -eq 1 ]
  then
    #if current distance is less that desired value, increase
    fsetpar "Slt S2-1|${2}dMovC" 3
    movein=0
  else
    break
  fi

  #calculate the estimated time (eta) to move the slits
  speed=0.075
  start=$(date +%s)
  eta=$(echo "($now - $1) / $speed" | bc -l)
  fin=$(echo "${eta#-} + $start" | bc -l)

  while [ $(echo "$now < $fin" | bc -l) -eq 1 ]
  do
    usleep 230000
    #get current distance and output it
    freadxpar "L:Slt S2-1|${2}dPosR" current
    echo $current
    if [ $(echo "$current <= $1 && $movein" |bc -l) -eq 1 ]
```

```
    then
      #break out of loop if desired distance is reached (too early)
      break
    elif [ $(echo "$current >= $1 && $movein==0" |bc -l) -eq 1 ]
    then
      #likewise, but for the other movement direction
      break
    fi
    #get current time
    now=$(date +%s)
  done
  #stop moving
  fsetpar "Slt S2-1|${2}dMovC" 0
}

#call the main function 3 times to get more accurate results
set_distance () {
  set_dist $1 $2
  sleep 2
  set_dist $1 $2
  sleep 2
  set_dist $1 $2
}

. $SCRIPTDIR/scriptheader
#actual function call
set_distance $1 $2
```

Calculations

Maximum values

Using the parametric equation (22) for x' of the ellipse, to find x_0, one can set x' to zero:

$$\begin{aligned} x'(t) &\overset{!}{=} 0 = a\sin\theta\cos t + b\cos\theta\sin t \\ \Rightarrow \tan(t) &= \frac{-a\tan\theta}{b} \\ \Rightarrow x_0 &= a\cos\theta\cos\left(\arctan\left(\frac{-a\tan\theta}{b}\right)\right) - b\sin\theta\sin\left(\arctan\left(\frac{-a\tan\theta}{b}\right)\right). \end{aligned}$$

With $\cos(\arctan(x)) = \frac{1}{\sqrt{x^2+1}}$ and $\sin(\arctan(x)) = \frac{x}{\sqrt{x^2+1}}$, and working similarly for x'_0 one can see:

$$x_0 = \frac{a\cos\theta + a\sin\theta\tan\theta}{\sqrt{\frac{a^2\tan^2\theta}{b^2}+1}} = \frac{ab}{\sqrt{a^2\sin^2\theta + b^2\cos^2\theta}}, \tag{33}$$

$$x'_0 = \frac{a\sin\theta + a\cos\theta/\tan\theta}{\sqrt{\frac{a^2}{b^2\tan^2\theta}+1}} = \frac{ab}{\sqrt{a^2\cos^2\theta + b^2\sin^2\theta}}. \tag{34}$$

Finally, using (23), it follows:

$$x_{\mathsf{max}} = \frac{ab}{x'_0} = \sqrt{a^2\cos^2\theta + b^2\sin^2\theta}, \tag{35}$$

$$x'_{\mathsf{max}} = \frac{ab}{x_0} = \sqrt{a^2\sin^2\theta + b^2\cos^2\theta}. \tag{36}$$

For the values x_0 and x'_{max}, which are the two more meaningful in the use case of phase space ellipses, the uncertainty propagation was calculated as follows:

$$\mathrm{u}(x_0) = \sqrt{\frac{b^6\cos^4\theta\cdot\mathrm{u}(a)^2 + a^6\sin^4\theta\cdot\mathrm{u}(b)^2 + \left(ab(b^2-a^2)\sin^2\theta\cos^2\theta\right)^2\cdot\mathrm{u}(\theta)^2}{\left(a^2\sin^2\theta + b^2\cos^2\theta\right)^{3/2}}} \tag{37}$$

$$\mathrm{u}(x'_{\mathsf{max}}) = \sqrt{\left(\frac{b}{x_0}\cdot\mathrm{u}(a)\right)^2 + \left(\frac{a}{x_0}\cdot\mathrm{u}(b)\right)^2 + \left(\frac{ab}{x_0^2}\cdot\mathrm{u}(x_0)\right)^2} \tag{38}$$

Waist position

The equation (36) represents the maximum divergence of any particle on the 1σ ellipse of a beam. In a phase space diagram, it is the upper bound of the ellipse and is invariant under linear beam transformations. If one looks at the phase space of a beam and wants to determine where the waist of the beam is, one can look at how far to the right the top of the ellipse x'_{max} has shifted. If it is directly above the centre, i.e. $x(x'_{\text{max}}) = 0$, one is looking at the waist. If the beam has moved further by d, then $x(x'_{\text{max}}) = d \cdot \tan(x'_{\text{max}})$. To calculate the beam waist position from a sheared phase ellipse, one can thus calculate $d_{\text{waist}} = \frac{x(x'_{\text{max}})}{\tan(x'_{\text{max}})} \approx \frac{x(x'_{\text{max}})}{x'_{\text{max}}}$ by first looking at the ellipse parameter t_m at x'_{max}:

$$x'(t) \overset{!}{=} x'_{\text{max}} = a\sin\theta\cos t + b\cos\theta\sin t =: A\cos t + B\sin t\,. \tag{39}$$

With $A = a\sin\theta$, $B = b\cos\theta$, where $x'^2_{\text{max}} = A^2 + B^2$, see (36), and $y = \tan\frac{t}{2}$, where $\sin t = \frac{2y}{y^2+1}$ and $\cos t = \frac{-y^2+1}{y^2+1}$, it follows:

$$\begin{aligned}
0 &= -x'_{\text{max}} + A \cdot \frac{-y^2+1}{y^2+1} + B \cdot \frac{2y}{y^2+1} \\
0 &= -y^2(x'_{\text{max}} + A) - x'_{\text{max}} + A + 2By \\
\frac{x'_{\text{max}} - A}{x'_{\text{max}} + A} &= -y^2 + \frac{2By}{x'_{\text{max}} + A} \\
\frac{x'_{\text{max}} - A}{x'_{\text{max}} + A} - \frac{B^2}{(x'_{\text{max}} + A)^2} &= \underbrace{-y^2 + \frac{2By}{x'_{\text{max}} + A} - \frac{B^2}{(x'_{\text{max}} + A)^2}}_{-\left(y - \frac{B}{x'_{\text{max}}+A}\right)^2} \\
y &= \frac{B}{x'_{\text{max}} + A} \pm \sqrt{\frac{(x'_{\text{max}} - A)\cdot(x'_{\text{max}} + A) - B^2}{(x'_{\text{max}} + A)^2}} \\
\tan\left(\frac{t_m}{2}\right) &= \frac{B \pm \overbrace{\sqrt{x'^2_{\text{max}} - A^2 - B^2}}^{=(A^2+B^2)-A^2-B^2=0}}{x'_{\text{max}} + A} = \frac{B}{A + \sqrt{A^2+B^2}} \\
t_m &= 2 \cdot \arctan\left(\frac{b\cos\theta}{a\sin\theta + \sqrt{a^2\sin^2\theta + b^2\cos^2\theta}}\right)\,.
\end{aligned} \tag{40}$$

Finding the value $x(x'_{\text{max}})$ is then only a matter of placing t_m in the equation for $x(t)$:

$$x(t_m) = a\cos\theta\cos(t_m) - b\sin\theta\sin(t_m)\,.$$

With the identities $\cos(2\cdot\arctan(x)) = \frac{1-x^2}{x^2+1}$ and $\sin(2\cdot\arctan(x)) = \frac{2x}{x^2+1}$, one gets:

$$\begin{aligned}
x(t_m) &= \frac{a\cos\theta - a\cos\theta\cdot\frac{b^2\cos^2\theta}{(a\sin\theta+x'_{\text{max}})^2} - 2b\sin\theta\cdot\frac{b\cos\theta}{a\sin\theta+x'_{\text{max}}}}{\frac{b^2\cos^2\theta}{(a\sin\theta+x'_{\text{max}})^2}+1} \\
&= \frac{a\cos\theta(a\sin\theta+x'_{\text{max}})^2 - ab^2\cos^3\theta - 2b^2\sin\theta\cos\theta(a\sin\theta+x'_{\text{max}})}{b^2\cos^2\theta+(a\sin\theta+x'_{\text{max}})^2} \\
&= \frac{(a^2-b^2)(\sin\theta\cos\theta(a\sin\theta+\sqrt{a^2\sin^2\theta+b^2\cos^2\theta}))}{a^2\sin^2\theta+b^2\cos^2\theta+a\sin\theta\sqrt{a^2\sin^2\theta+b^2\cos^2\theta}} \\
&= \frac{(a^2-b^2)\cdot\sin\theta\cos\theta}{\sqrt{a^2\sin^2\theta+b^2\cos^2\theta}} = \frac{(a^2-b^2)\cdot\sin\theta\cos\theta}{x'_{\text{max}}}\,.
\end{aligned} \tag{41}$$

Conclusively, one gets the distance between the waist and phase space measurement point:

$$d_{\text{waist}} = \frac{x(t_m)}{\tan(x'_{\text{max}})} \approx \frac{(a^2-b^2)\cdot\sin\theta\cos\theta}{x'^2_{\text{max}}} = \frac{(a^2-b^2)\cdot\sin\theta\cos\theta}{a^2\sin^2\theta+b^2\cos^2\theta}\,. \tag{42}$$

For the uncertainty propagation, one can calculate:

$$\mathrm{u}(d_{\text{waist}}) = \sqrt{\frac{(4a^2\mathrm{u}(a)^2+4b^2\mathrm{u}(b)^2+4(a^2-b^2)^2\mathrm{u}(x'^2_{\text{max}})^2/x'^2_{\text{max}})\cdot\sin^2\theta\cos^2\theta}{x'^4_{\text{max}}}} \tag{43}$$

Courant-Snyder parameters

The previously calculated values can also be expressed using the Courant-Snyder (CS) parameters (Courant & Snyder, 1958), also called Twiss parameters. Using the conventions from (Holzer, 2013), namely $x_0 = \sqrt{\frac{\epsilon}{\gamma}}$, $x'_0 = \sqrt{\frac{\epsilon}{\beta}}$, $x(x'_{\text{max}}) = -\alpha\sqrt{\frac{\epsilon}{\gamma}}$, and $\epsilon = ab$, as well as using formulas (33), (34), and (41) it follows that:

$$\alpha = (b^2-a^2)\sin\theta\cos\theta/ab \tag{44}$$

$$\beta = (a^2\cos^2\theta+b^2\sin^2\theta)/ab \tag{45}$$

$$\gamma = (a^2\sin^2\theta+b^2\cos^2\theta)/ab \tag{46}$$

Furthermore, following the common rule for propagation of uncertainty, one can see:

$$\mathrm{u}(\alpha) = \sqrt{\left(\frac{(a^2+b^2)\cdot\sin(\theta)\cdot\cos(\theta)}{a^2\cdot b}\cdot \mathrm{u}(a)\right)^2 + \overline{+\left(\frac{(a^2+b^2)\cdot\sin(\theta)\cdot\cos(\theta)}{a\cdot b^2}\cdot \mathrm{u}(b)\right)^2 + \left(\frac{(a^2-b^2)\cdot(\cos(\theta)^2-\sin(\theta)^2)}{a\cdot b}\cdot \mathrm{u}(\theta)\right)^2}} \tag{47}$$

$$\mathrm{u}(\beta) = \sqrt{\left(\left(\frac{\cos(\theta)^2}{b} - \frac{b\sin(\theta)^2}{a^2}\right)\cdot \mathrm{u}(a)\right)^2 + \overline{+\left(\left(\frac{\cos(\theta)^2}{a} - \frac{a\sin(\theta)^2}{b^2}\right)\cdot \mathrm{u}(b)\right)^2 + \left(\frac{2(a^2-b^2)\cdot\sin(\theta)\cdot\cos(\theta)}{ab}\cdot \mathrm{u}(\theta)\right)^2}} \tag{48}$$

$$\mathrm{u}(\gamma) = \sqrt{\left(\left(\frac{\sin(\theta)^2}{b} - \frac{b\cos(\theta)^2}{a^2}\right)\cdot \mathrm{u}(a)\right)^2 + \overline{+\left(\left(\frac{\cos(\theta)^2}{a} - \frac{a\sin(\theta)^2}{b^2}\right)\cdot \mathrm{u}(b)\right)^2 + \left(\frac{2(a^2-b^2)\cdot\sin(\theta)\cdot\cos(\theta)}{ab}\cdot \mathrm{u}(\theta)\right)^2}} \tag{49}$$

All phase space measurements

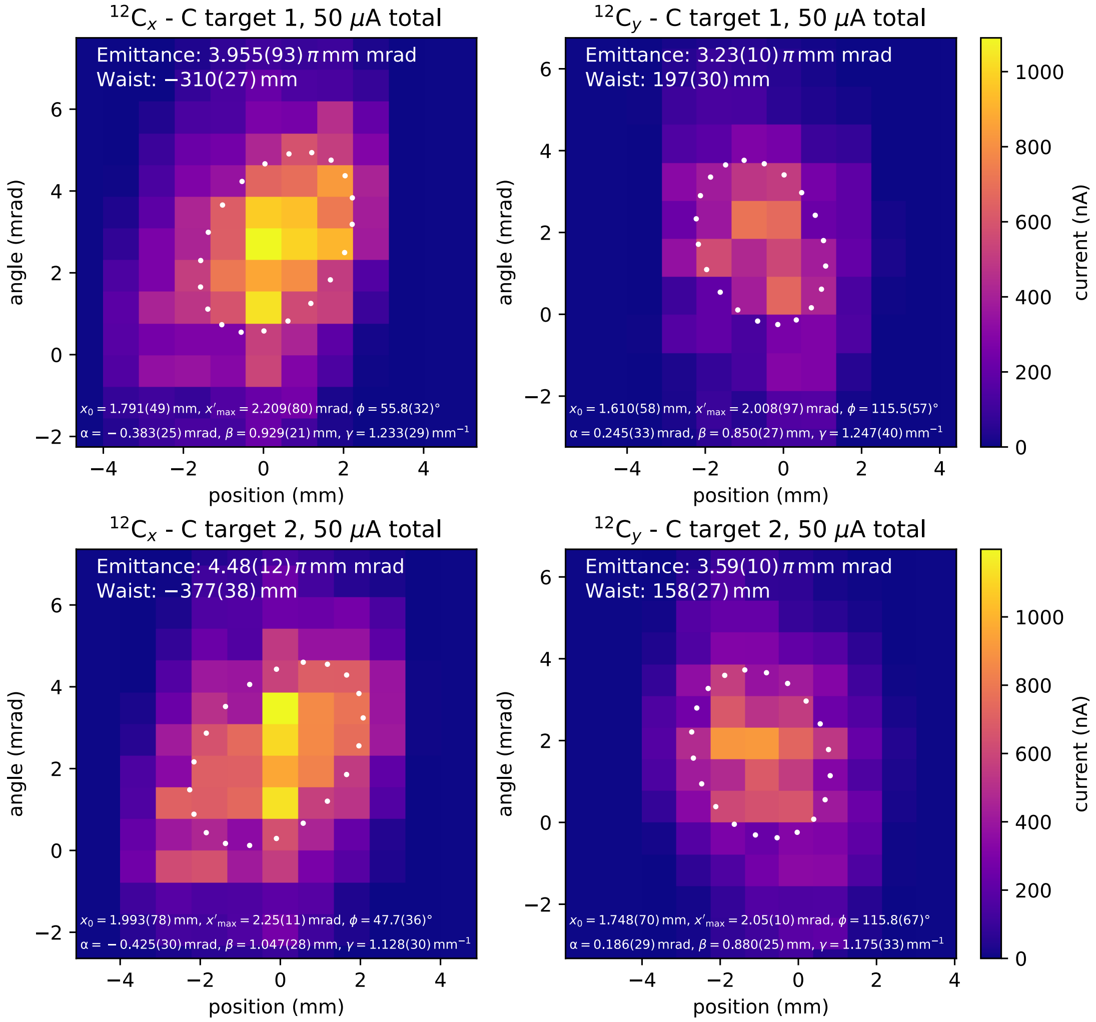

Figure 59: Part 1 of phase space measurements of a high current $^{12}C^-$ beam.

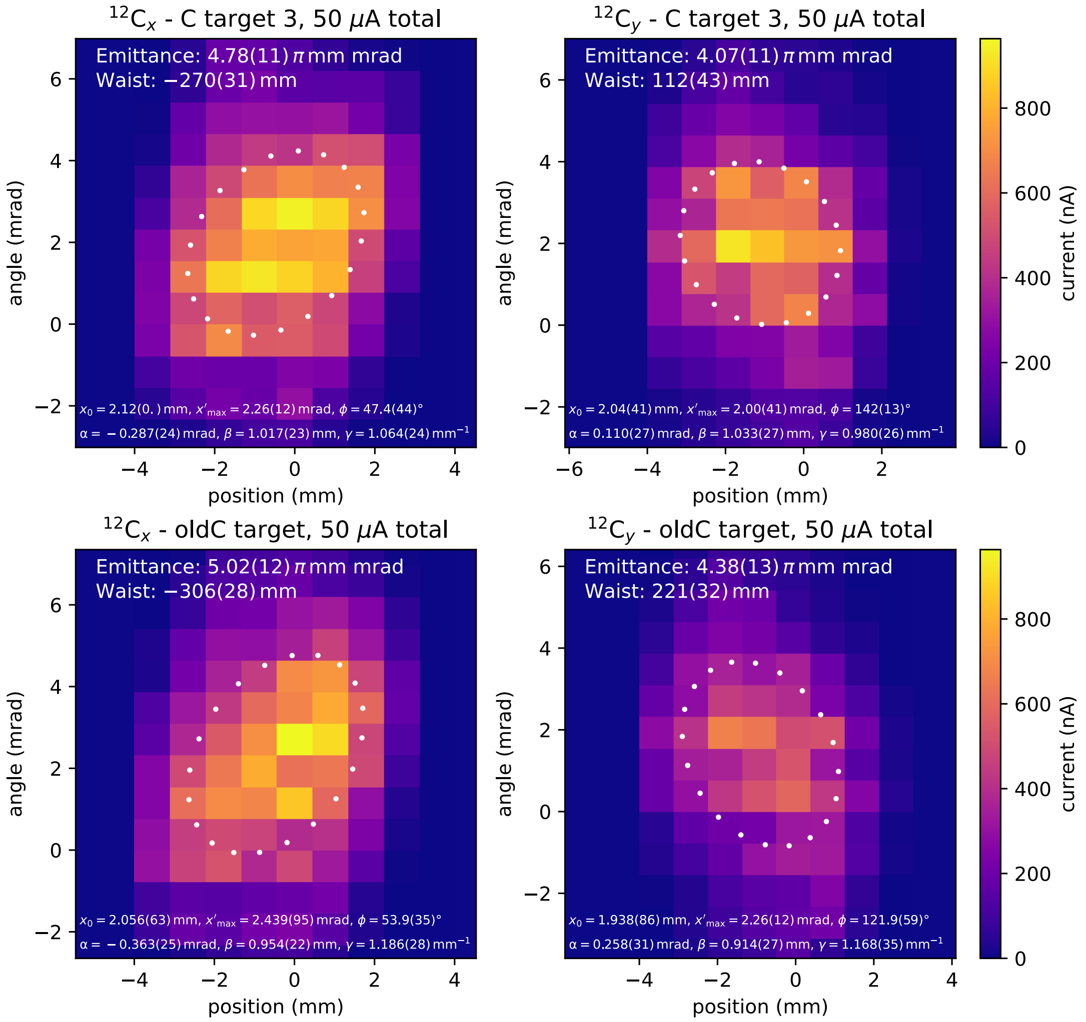

Figure 60: Part 2 of phase space measurements of a high current $^{12}C^-$ beam.

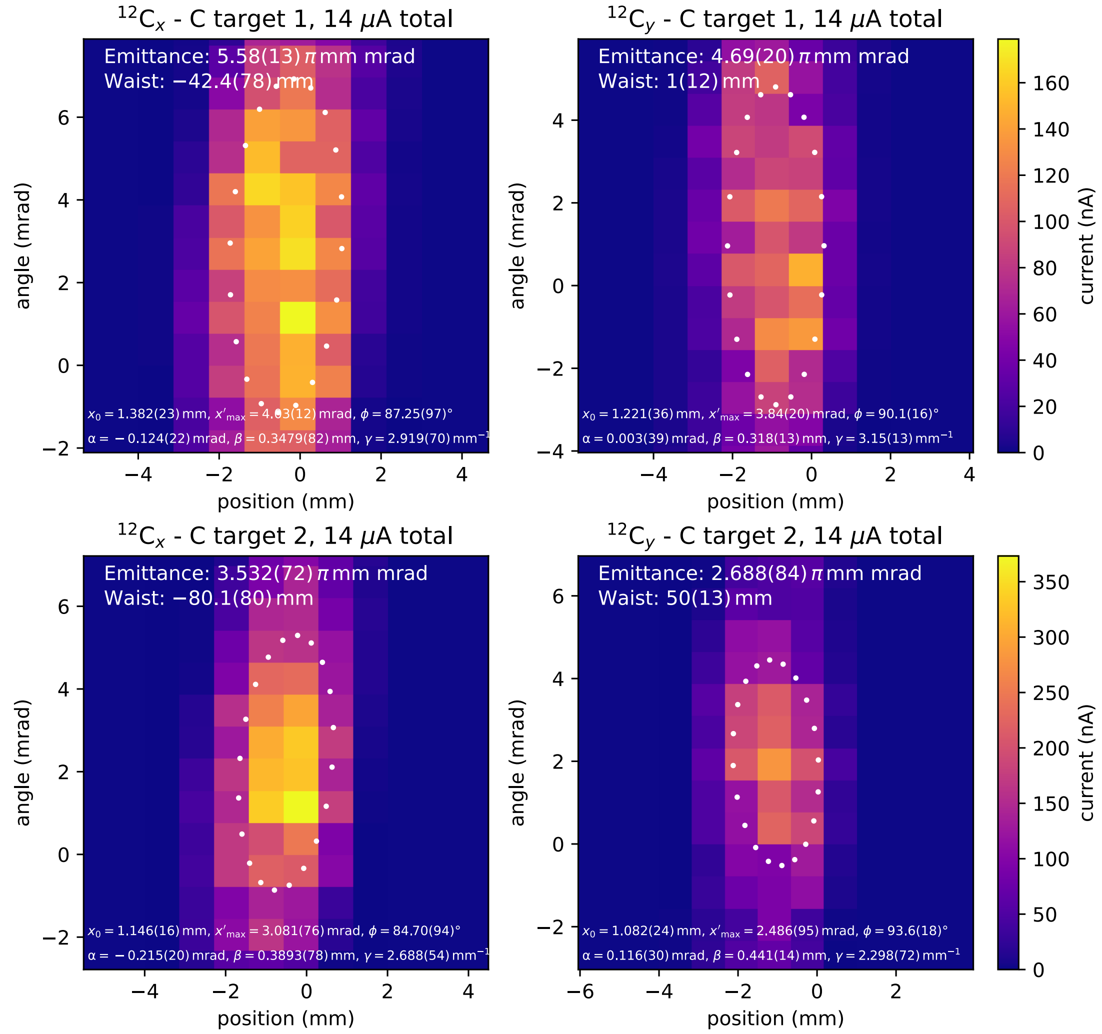

Figure 61: Part 1 of phase space measurements of a low current $^{12}C^-$ beam.

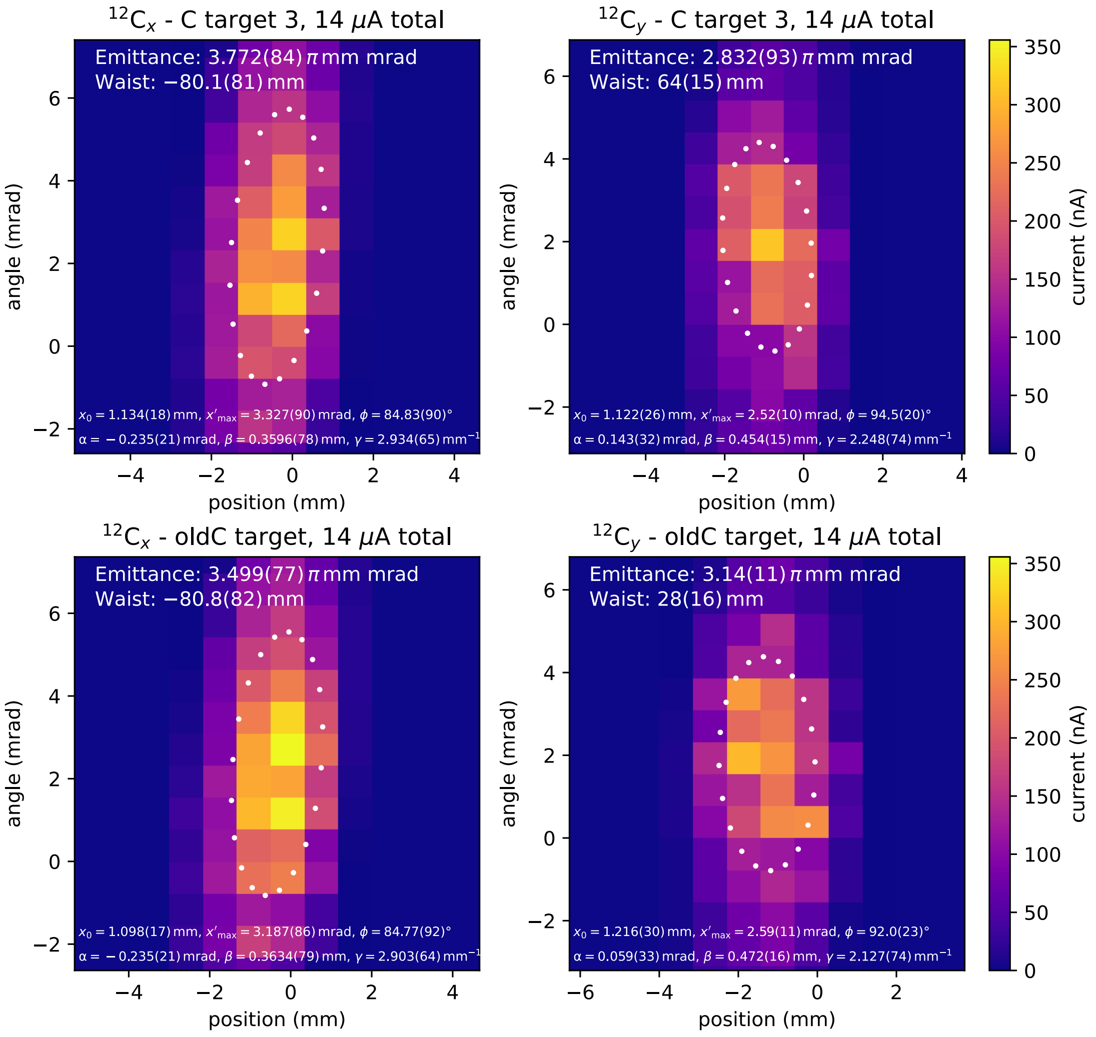

Figure 62: Part 2 of phase space measurements of a low current $^{12}C^-$ beam.

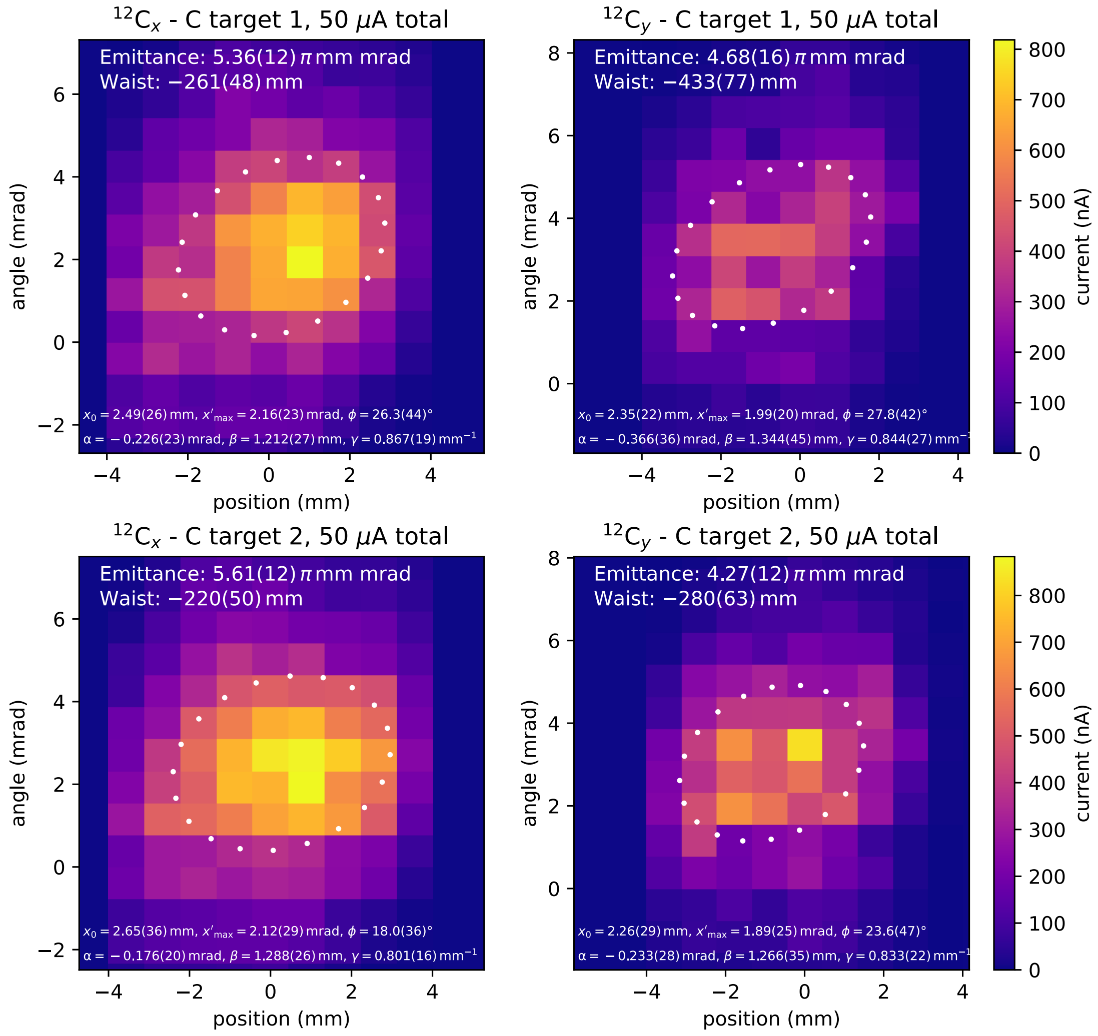

Figure 63: Phase space measurements of high current $^{12}C^-$ beams, after the target was sputtered for $4-5$ h.

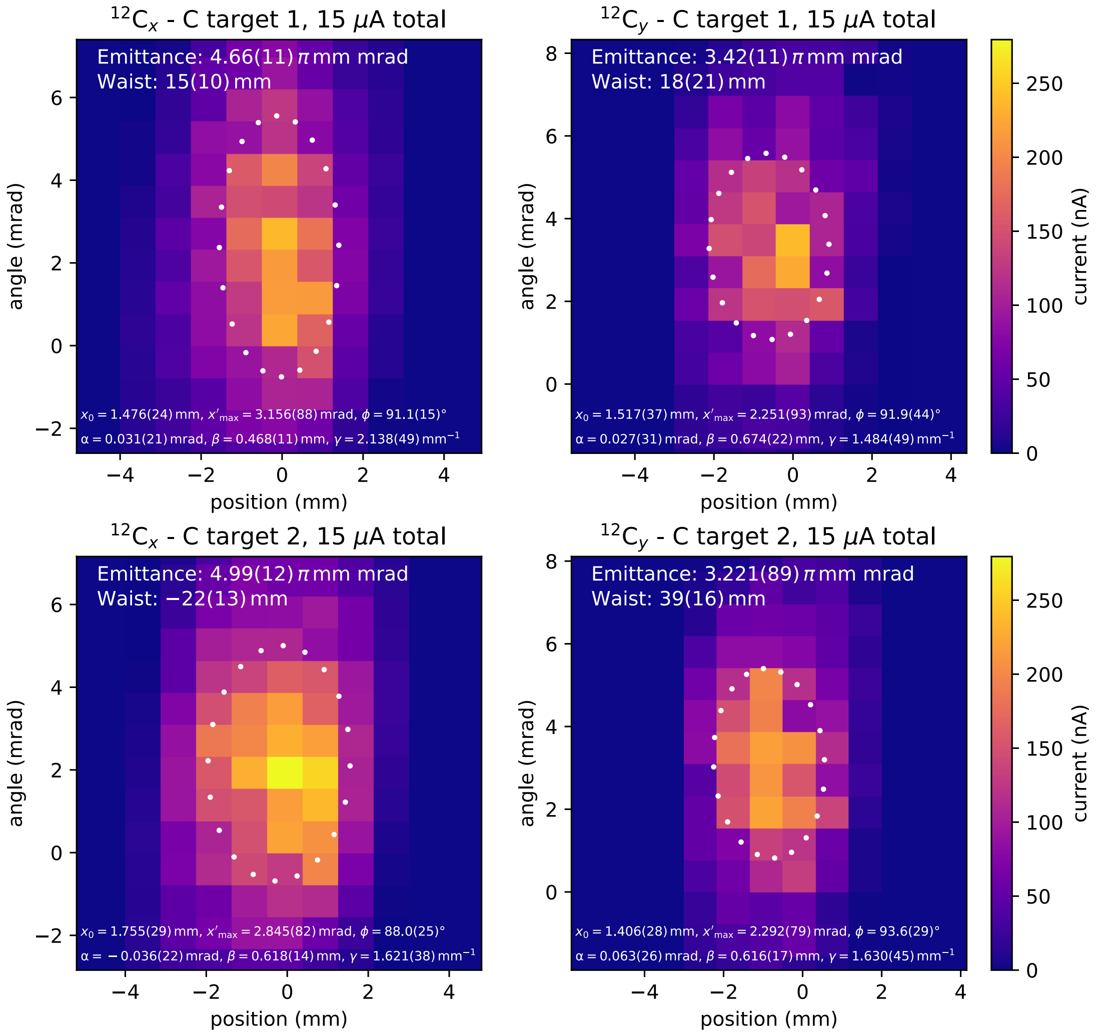

Figure 64: Phase space measurements of low current $^{12}C^-$ beams, after the target was sputtered for $4 - 5$ h.

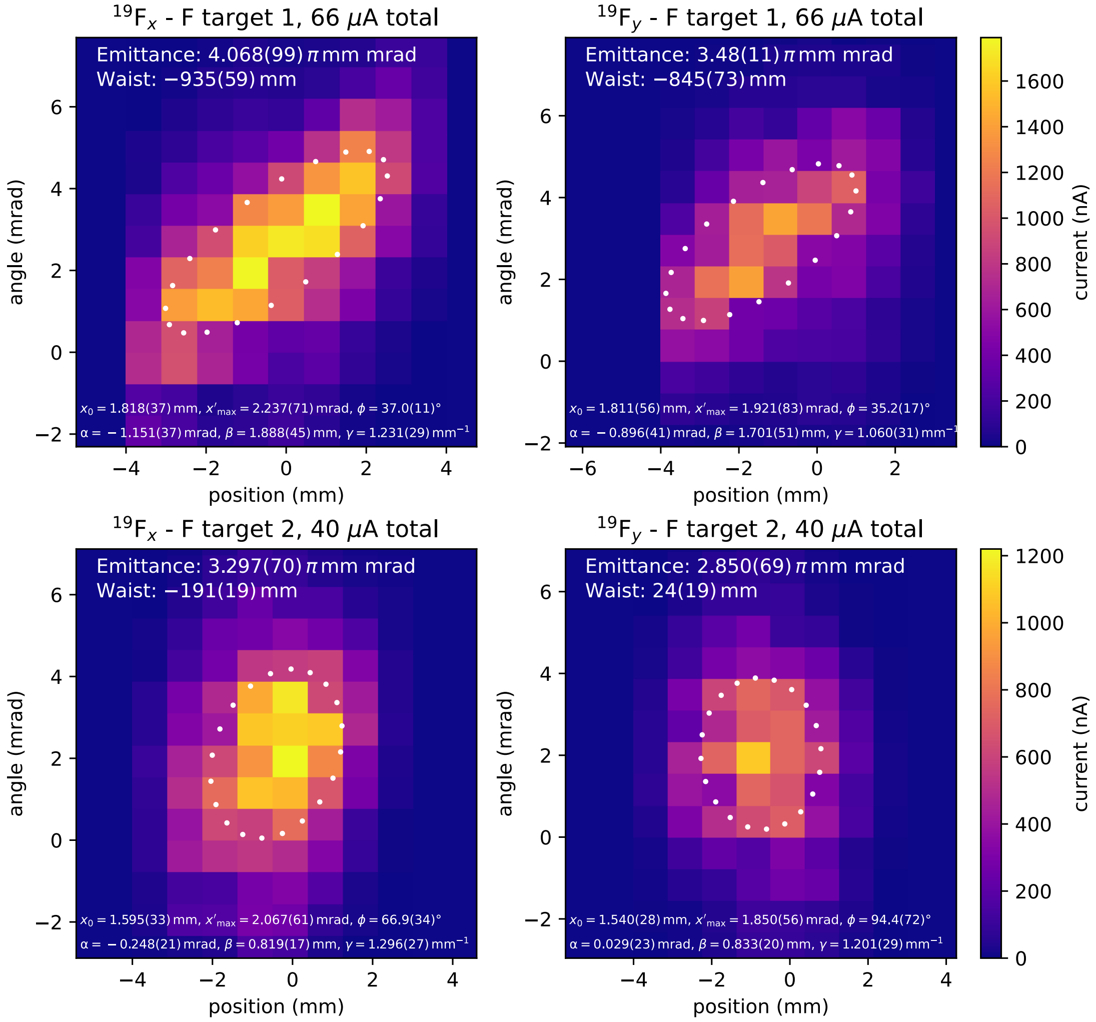

Figure 65: Phase space measurements of high current $^{19}F^-$ beams.

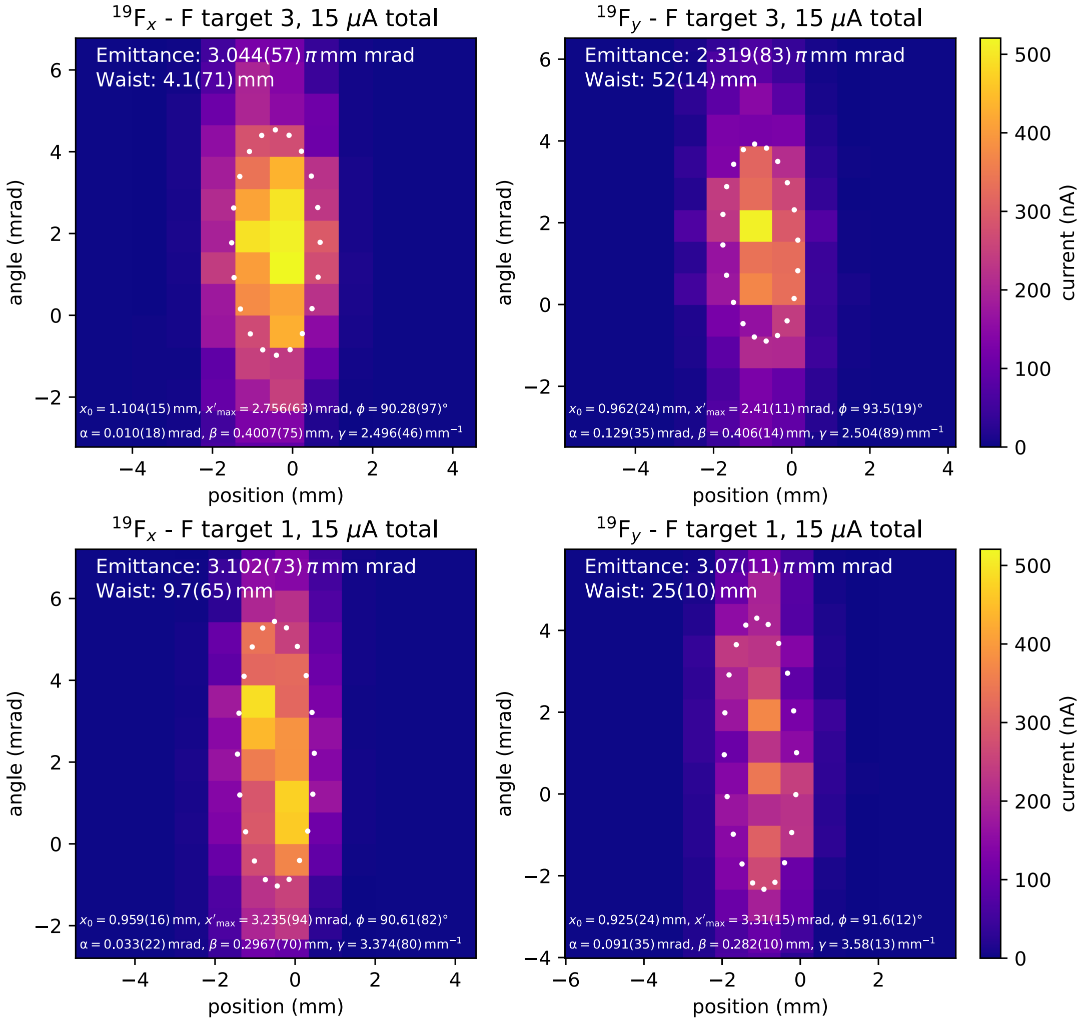

Figure 66: Phase space measurements of low current $^{19}F^-$ beams.

Table 5: All phase space measurement fit values, x direction. A positive sign of the waist position signifies a waist downstream from the measurement point of `SLT S2-1`.

	ion beam current (μA)	x emittance (mm mrad π)	x waist (mm)	x_0 (mm)	x'_{m} (mrad)	ϕ_x (°)	α_x (mrad)	β_x (mm)	γ_x (mm^{-1})
C target 1	50	3.955(93)	−310(27)	1.791(49)	2.209(80)	55.8(32)	−0.383(25)	0.929(21)	1.233(29)
C target 2	50	4.48(12)	−377(38)	1.993(78)	2.25(11)	47.7(36)	−0.425(30)	1.047(28)	1.128(30)
C target 3	50	4.78(11)	−270(31)	2.12(10)	2.26(12)	47.4(44)	−0.287(24)	1.017(23)	1.064(24)
oldC target	50	5.02(12)	−306(28)	2.056(63)	2.439(95)	53.9(35)	−0.363(25)	0.954(22)	1.186(28)
C target 1	14	5.58(13)	−42.4(78)	1.382(23)	4.03(12)	87.25(97)	−0.124(22)	0.3479(82)	2.919(70)
C target 2	14	3.532(72)	−80.1(80)	1.146(16)	3.081(76)	84.70(94)	−0.215(20)	0.3893(78)	2.688(54)
C target 3	14	3.772(84)	−80.1(81)	1.134(18)	3.327(90)	84.83(90)	−0.235(21)	0.3596(78)	2.934(65)
oldC target	14	3.499(77)	−80.8(82)	1.098(17)	3.187(86)	84.77(92)	−0.235(21)	0.3634(79)	2.903(64)
C target 1, long	50	5.36(12)	−261(48)	2.49(26)	2.16(23)	26.3(44)	−0.226(23)	1.212(27)	0.867(19)
C target 2, long	50	5.61(12)	−220(50)	2.65(36)	2.12(29)	18.0(36)	−0.176(20)	1.288(26)	0.801(16)
C target 1, long	15	4.66(11)	15(10)	1.476(24)	3.156(88)	91.1(15)	0.031(21)	0.468(11)	2.138(49)
C target 2, long	15	4.99(12)	−22(13)	1.755(29)	2.845(82)	88.0(25)	−0.036(22)	0.618(14)	1.621(38)
PbF_2 target 1	66	4.068(99)	−935(59)	1.818(37)	2.237(71)	37.0(11)	−1.151(37)	1.888(45)	1.231(29)
PbF_2 target 2	40	3.297(70)	−191(19)	1.595(33)	2.067(61)	66.9(34)	−0.248(21)	0.819(17)	1.296(27)
PbF_2 target 3	15	3.044(57)	4.1(71)	1.104(15)	2.756(63)	90.28(97)	0.010(18)	0.4007(75)	2.496(46)
PbF_2 target 1	15	3.102(73)	9.7(65)	0.959(16)	3.235(94)	90.61(82)	0.033(22)	0.2967(70)	3.374(80)

Table 6: All phase space measurement fit values, y direction. A positive sign of the waist position signifies a waist downstream from the measurement point of `SLT S2-1`.

	ion beam current (μA)	y emittance (mm mrad π)	y waist (mm)	y_0 (mm)	y'_m (mrad)	ϕ_y (°)	α_y (mrad)	β_y (mm)	γ_y (mm^{-1})
C target 1	50	3.23(10)	197(30)	1.610(58)	2.008(97)	115.5(57)	0.245(33)	0.850(27)	1.247(40)
C target 2	50	3.59(10)	158(27)	1.748(70)	2.05(10)	115.8(67)	0.186(29)	0.880(25)	1.175(33)
C target 3	50	4.07(11)	112(43)	2.04(41)	2.00(41)	142(13)	0.110(27)	1.033(27)	0.980(26)
oldC target	50	4.38(13)	221(32)	1.938(86)	2.26(12)	121.9(59)	0.258(31)	0.914(27)	1.168(35)
C target 1	14	4.69(20)	1(12)	1.221(36)	3.84(20)	90.1(16)	0.003(39)	0.318(13)	3.15(13)
C target 2	14	2.688(84)	50(13)	1.082(24)	2.486(95)	93.6(18)	0.116(30)	0.441(14)	2.298(72)
C target 3	14	2.832(93)	64(15)	1.122(26)	2.52(10)	94.5(20)	0.143(32)	0.454(15)	2.248(74)
oldC target	14	3.14(11)	28(16)	1.216(30)	2.59(11)	92.0(23)	0.059(33)	0.472(16)	2.127(74)
C target 1, long	50	4.68(16)	−433(77)	2.35(22)	1.99(20)	27.8(42)	−0.366(36)	1.344(45)	0.844(27)
C target 2, long	50	4.27(12)	−280(63)	2.26(29)	1.89(25)	23.6(47)	−0.233(28)	1.266(35)	0.833(22)
C target 1, long	15	3.42(11)	18(21)	1.517(37)	2.251(93)	91.9(44)	0.027(31)	0.674(22)	1.484(49)
C target 2, long	15	3.221(89)	39(16)	1.406(28)	2.292(79)	93.6(29)	0.063(26)	0.616(17)	1.630(45)
$\mathrm{PbF_2}$ target 1	66	3.48(11)	−845(73)	1.811(56)	1.921(83)	35.2(17)	−0.896(41)	1.701(51)	1.060(31)
$\mathrm{PbF_2}$ target 2	40	2.850(69)	24(19)	1.540(28)	1.850(56)	94.4(72)	0.029(23)	0.833(20)	1.201(29)
$\mathrm{PbF_2}$ target 3	15	2.319(83)	52(14)	0.962(24)	2.41(11)	93.5(19)	0.129(35)	0.406(14)	2.504(89)
$\mathrm{PbF_2}$ target 1	15	3.07(11)	25(10)	0.925(24)	3.31(15)	91.6(12)	0.091(35)	0.282(10)	3.58(13)

All residence time measurements

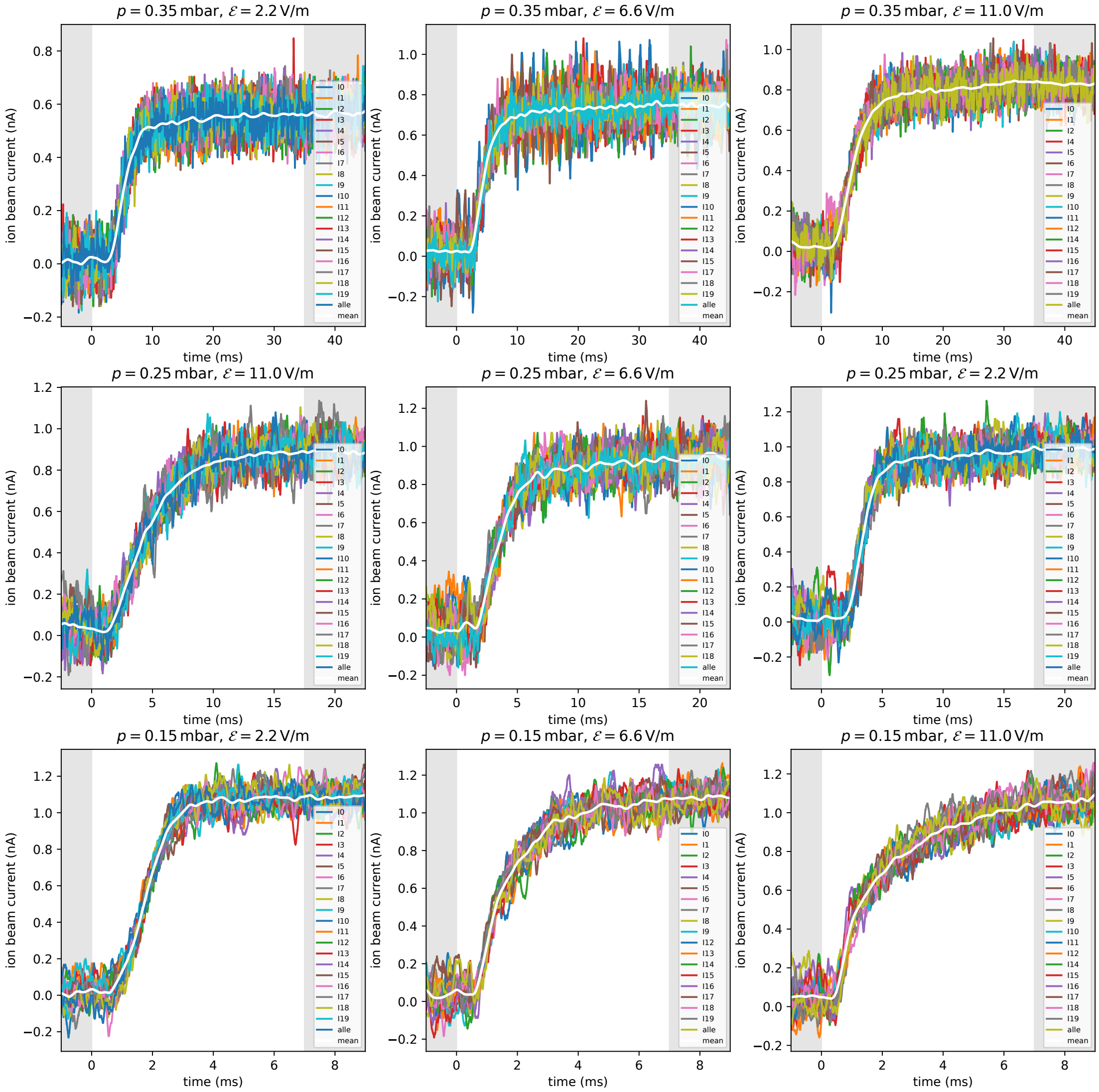

Figure 67: Step-on experiment with a 1 nA beam of $^{37}\mathrm{Cl}^{-}$, including a moving weighted average with $\sigma = 20$, where the whole time range consists of 2500 samples for each plot. Grey areas indicate the minimum and maximum values, to which the signal was normalised.

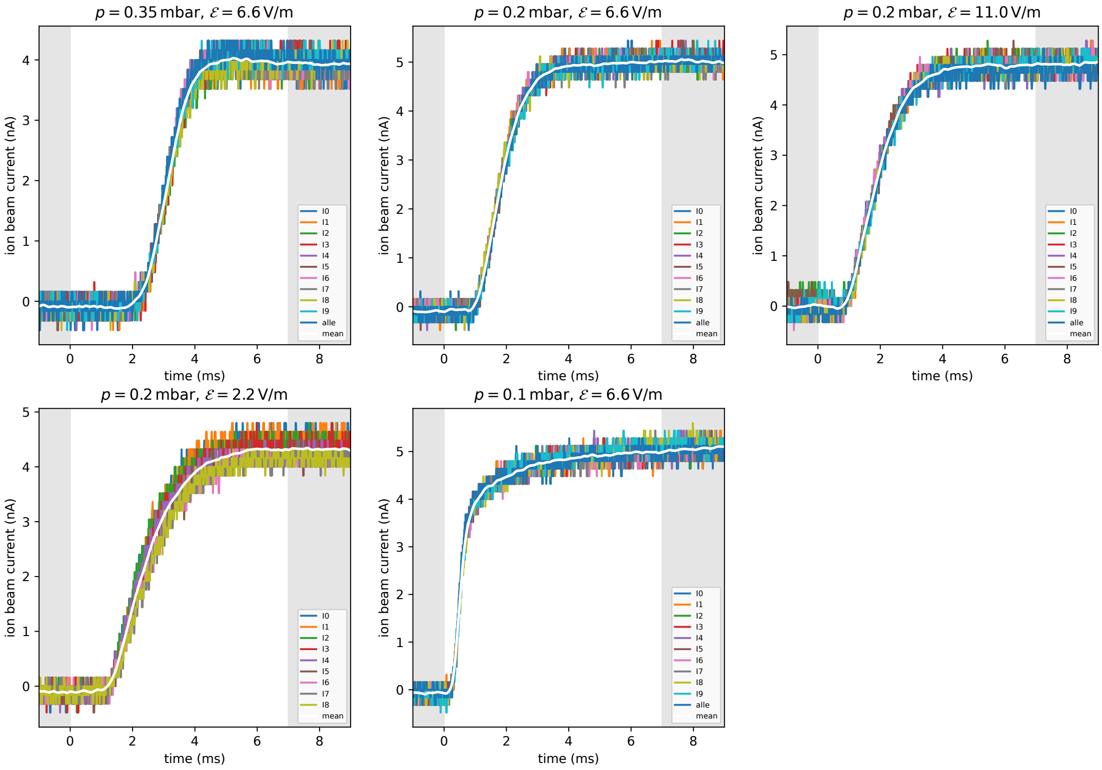

Figure 68: Step-on experiment with a 7 nA beam of $^{37}\mathrm{Cl}^{-}$, including a moving weighted average with $\sigma = 15$, where the whole time range consists of 2500 samples for each plot. Grey areas indicate the minimum and maximum values, to which the signal was normalised.

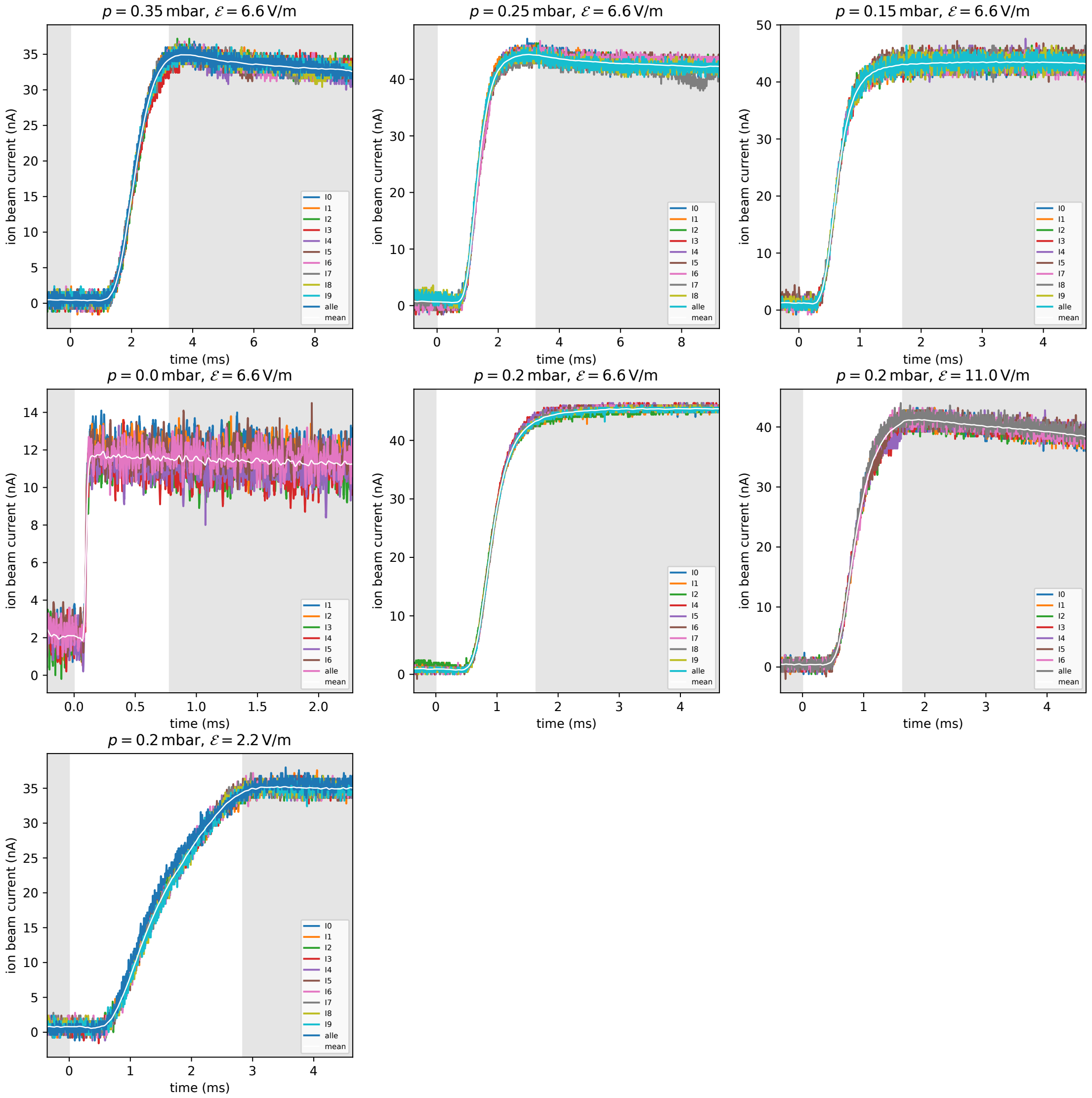
$p = 0.35\,\mathrm{mbar}$, $\mathcal{E} = 6.6\,\mathrm{V/m}$

$p = 0.25\,\mathrm{mbar}$, $\mathcal{E} = 6.6\,\mathrm{V/m}$

$p = 0.15\,\mathrm{mbar}$, $\mathcal{E} = 6.6\,\mathrm{V/m}$

$p = 0.0\,\mathrm{mbar}$, $\mathcal{E} = 6.6\,\mathrm{V/m}$

$p = 0.2\,\mathrm{mbar}$, $\mathcal{E} = 6.6\,\mathrm{V/m}$

$p = 0.2\,\mathrm{mbar}$, $\mathcal{E} = 11.0\,\mathrm{V/m}$

$p = 0.2\,\mathrm{mbar}$, $\mathcal{E} = 2.2\,\mathrm{V/m}$

Figure 69: Step-on experiment with a 55 nA beam of $^{37}\mathrm{Cl}^{-}$, including a moving weighted average with $\sigma = 10$, where the whole time range consists of 2500 samples for each plot. Grey areas indicate the minimum and maximum values, to which the signal was normalised.

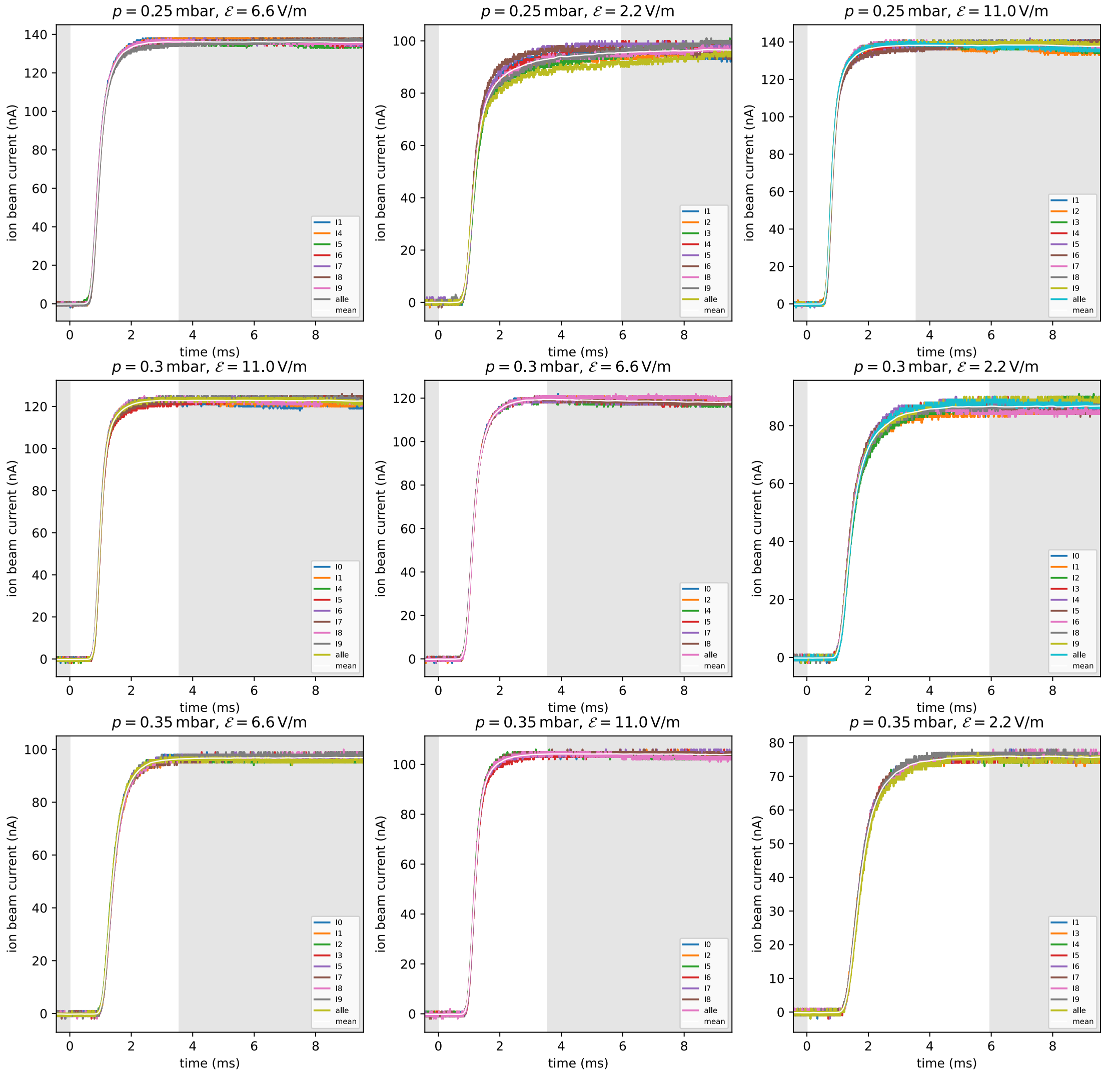

Figure 70: Part 1 of step-on experiment with a 200 nA beam of $^{35}\mathrm{Cl}^-$, including a moving weighted average with $\sigma = 10$, where the whole time range consists of 2500 samples for each plot. Grey areas indicate the minimum and maximum values, to which the signal was normalised.

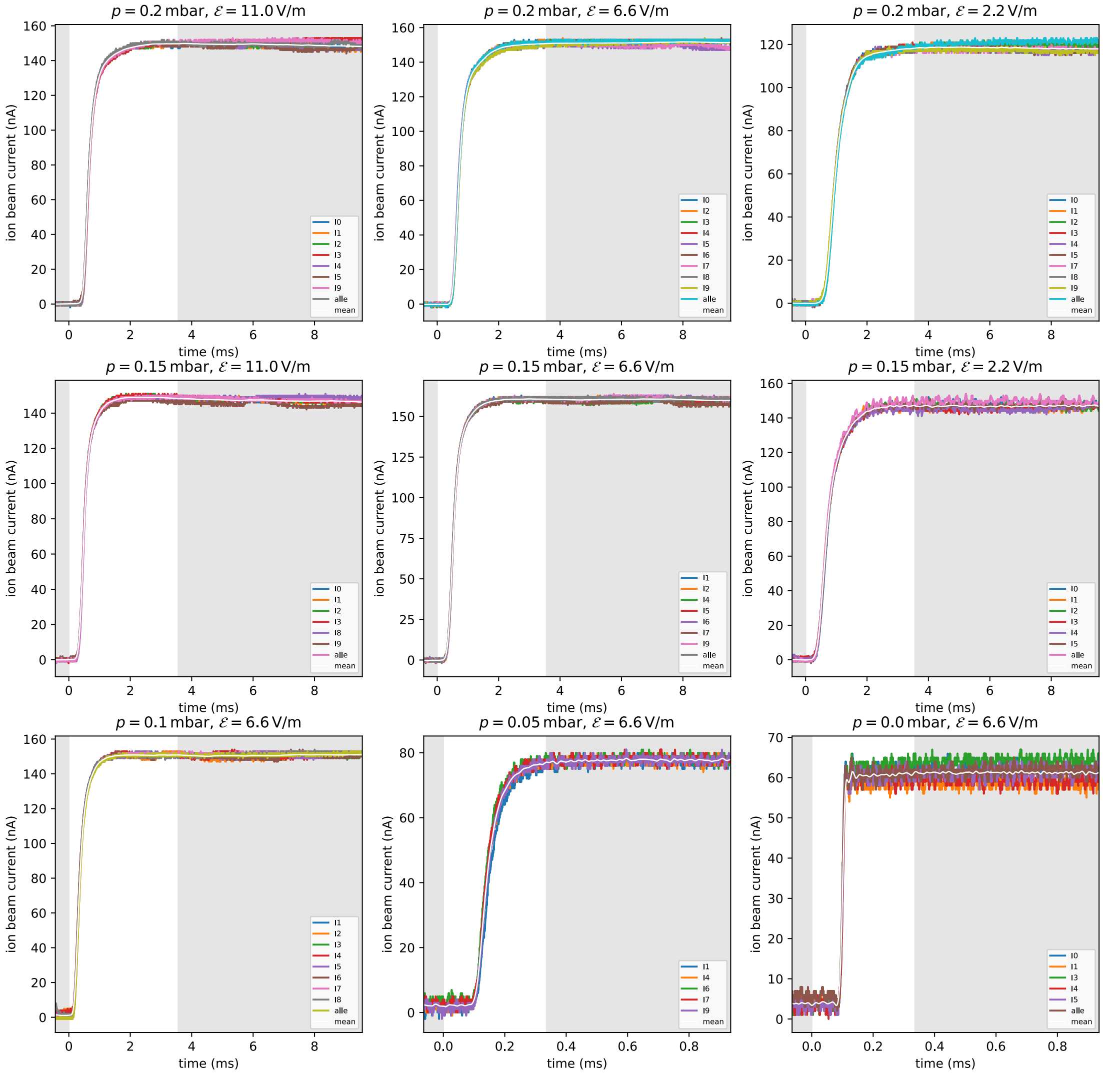

Figure 71: Part 2 of step-on experiment with a 200 nA beam of $^{35}\text{Cl}^{-}$, including a moving weighted average with $\sigma = 10$, where the whole time range consists of 2500 samples for each plot. Grey areas indicate the minimum and maximum values, to which the signal was normalised.

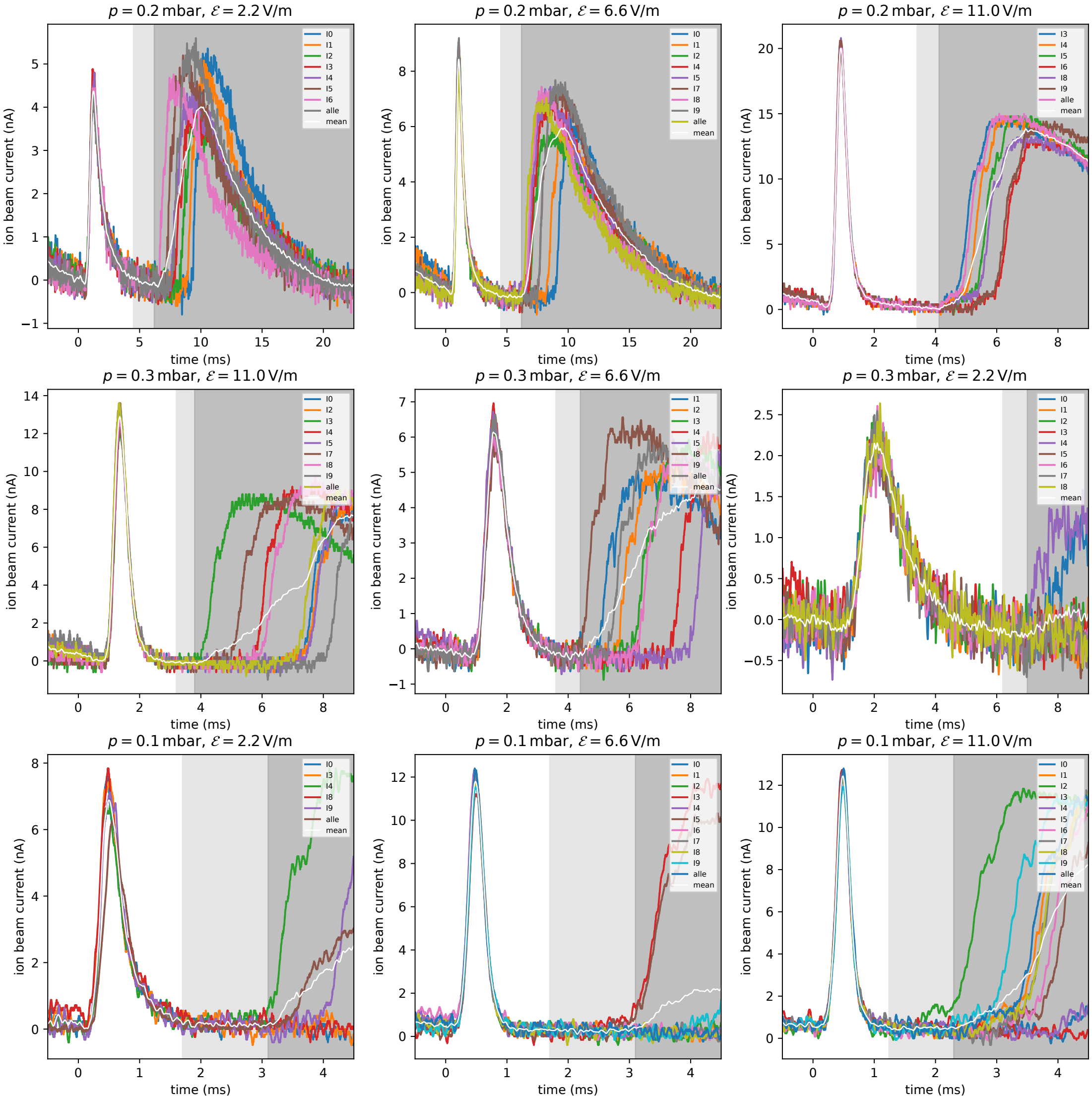

Figure 72: Pulse experiment with a 55 nA beam of $^{37}\mathrm{Cl}^{-}$, including a moving weighted average with $\sigma = 5$, where the whole time range consists of 2500 samples for each plot. Light grey areas indicate the minimum values, to which the signal was normalised, dark grey areas were discarded due to the 50 Hz ripple.

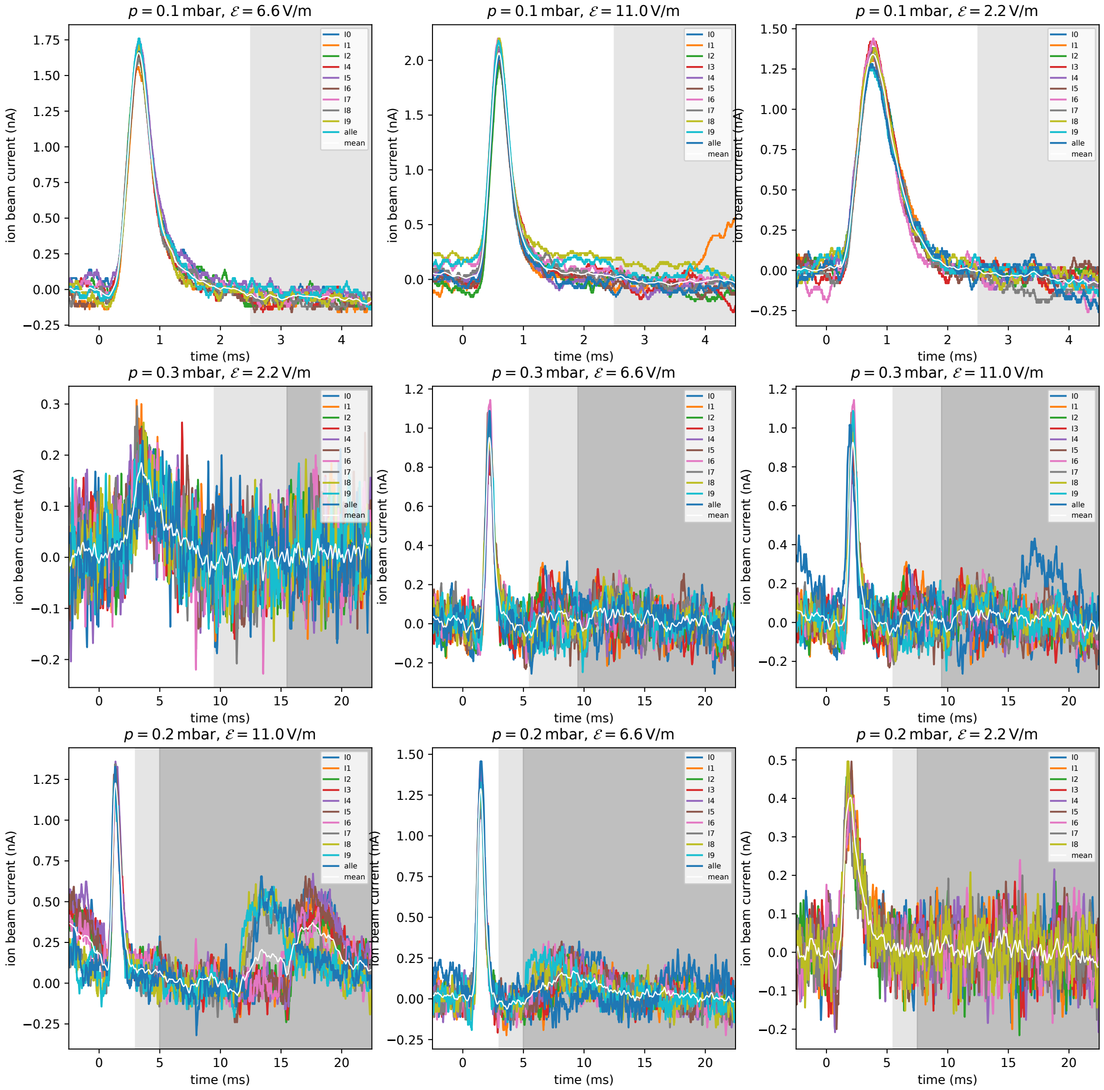

Figure 73: Pulse experiment with a 7 nA beam of $^{37}\text{Cl}^-$, including a moving weighted average with $\sigma = 5$, where the whole time range consists of 2500 samples for each plot. Light grey areas indicate the minimum values, to which the signal was normalised, dark grey areas were discarded due to the 50 Hz ripple.

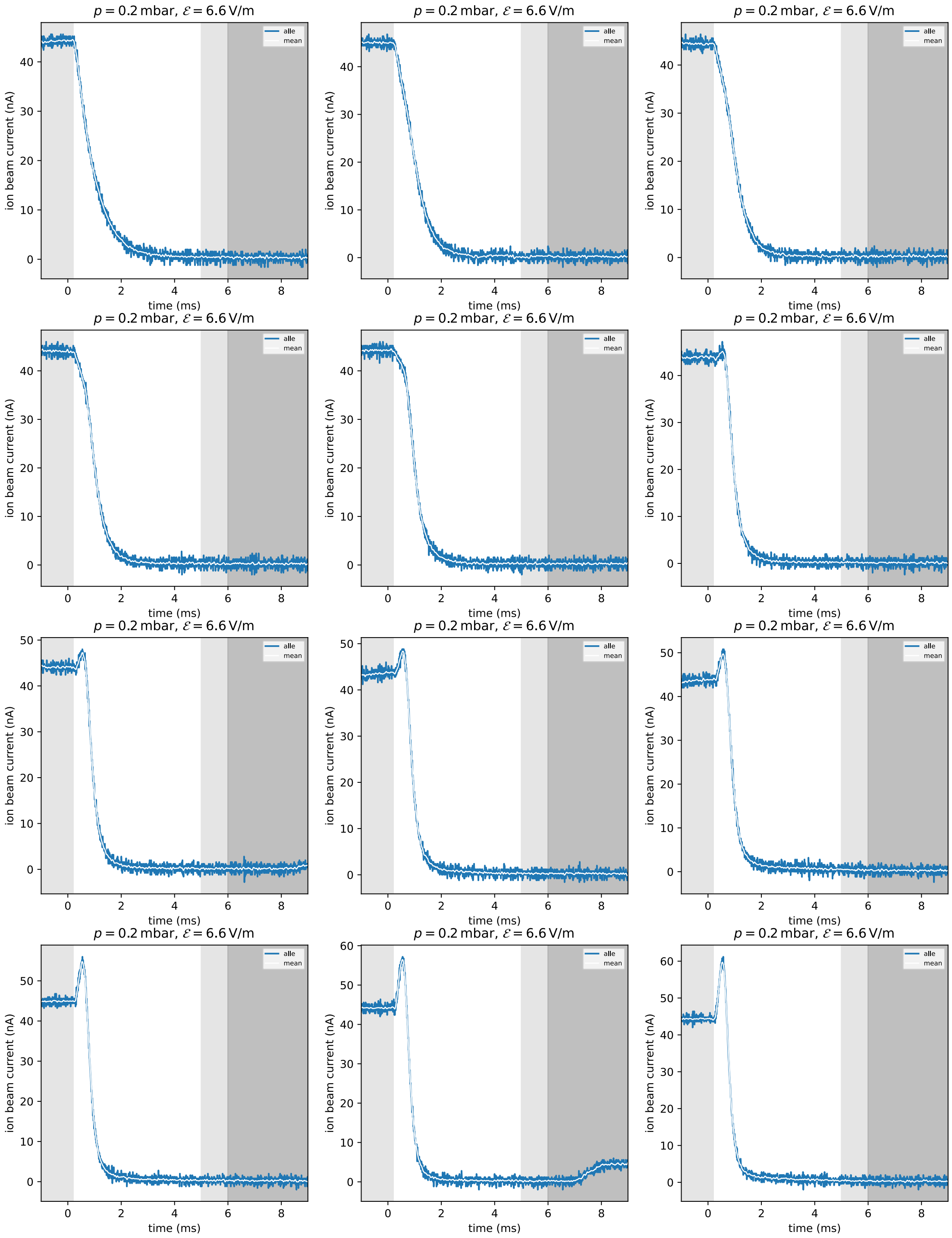

Figure 74: Part 1 of step off experiment (varying MBS voltage) with a 55 nA beam of $^{37}\mathrm{Cl}^-$, including a moving weighted average with $\sigma = 5$, where the whole time range consists of 2500 samples for each plot. Light grey areas indicate the initial/minimum values, to which the signal was normalised, dark grey areas were discarded.

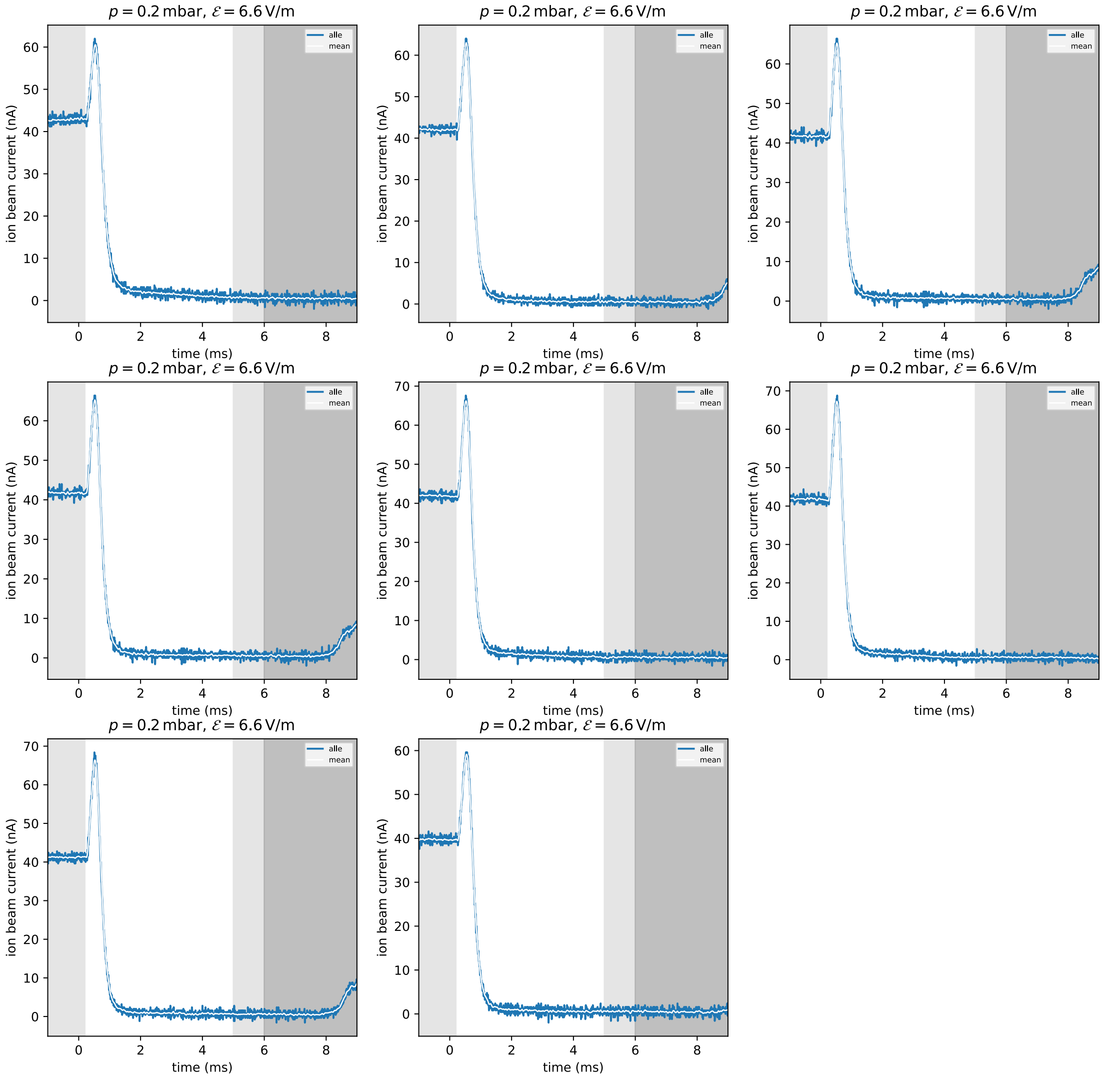

Figure 75: Part 2 of step off experiment (varying MBS voltage) with a 55 nA beam of $^{37}\mathrm{Cl}^-$, including a moving weighted average with $\sigma = 5$, where the whole time range consists of 2500 samples for each plot. Light grey areas indicate the initial/minimum values, to which the signal was normalised, dark grey areas were discarded.

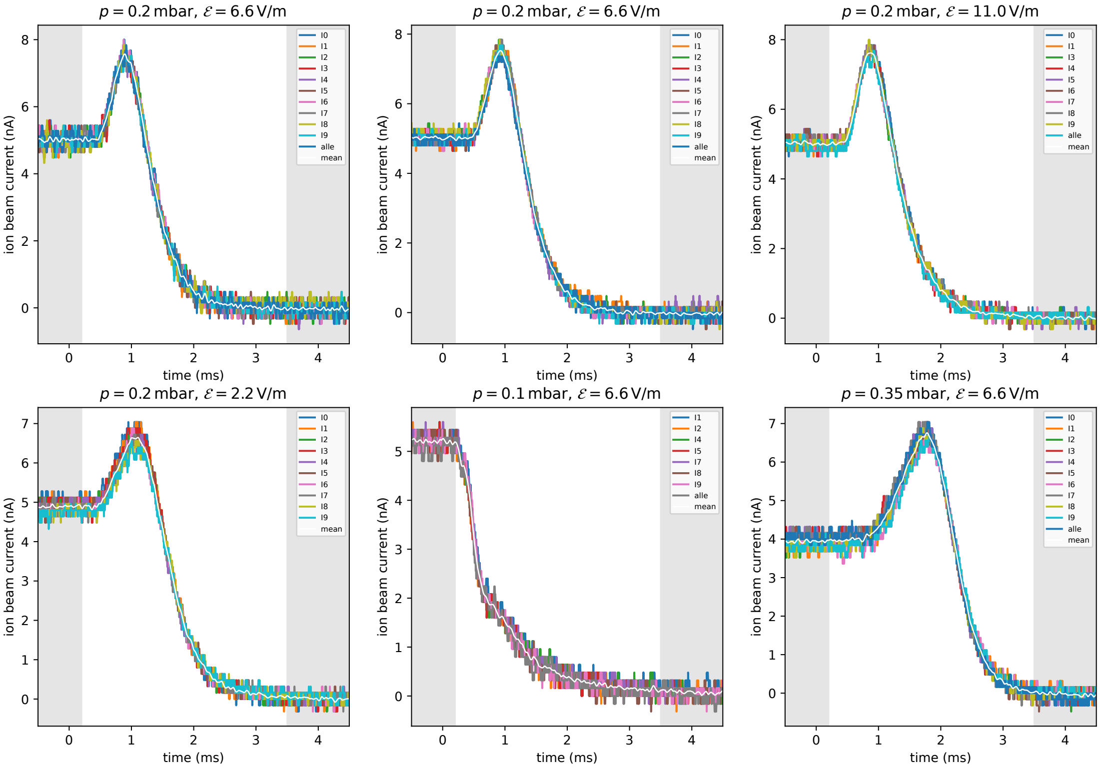

Figure 76: Step off experiment (varying cooler parameters) with a 7 nA beam of $^{37}\mathrm{Cl}^{-}$, including a moving weighted average with $\sigma = 5$, where the whole time range consists of 2500 samples for each plot. Light grey areas indicate the initial/minimum values, to which the signal was normalised.

Table 7: All mean residence times from step experiments.

		200 nA	55 nA	7 nA			1 nA
		step-on	step-on	step-on	step-off	weight. av.	step-on
p (mbar)	$\mathcal{E}$ (V/m)	$\bar{t}$ (ms)					
0.0	6.6	0.0851(49)	0.0647(71)				
0.05	6.6	0.1350(71)					
0.1	6.6	0.385(21)		0.970(53)	0.812(56)	0.893(39)	
0.15	2.2	0.795(42)					1.88(10)
	6.6	0.583(31)	0.662(35)				1.89(11)
	11.0	0.505(27)					2.07(11)
0.2	2.2	1.048(55)	1.529(78)	2.54(14)	2.038(17)	2.092(21)	
	6.6	0.810(42)	0.951(49)	1.93(10)	1.807(33)	1.838(35)	
	11.0	0.713(38)	0.864(45)	2.00(11)	1.862(32)	1.893(35)	
0.25	2.2	1.404(75)					4.03(23)
	6.6	1.008(52)	1.307(69)				4.15(25)
	11.0	0.888(47)					5.01(28)
0.3	2.2	1.596(83)					
	6.6	1.190(61)					
	11.0	1.044(54)					
0.35	2.2	1.866(95)					6.41(41)
	6.6	1.460(75)	2.07(11)	3.09(16)	3.05(18)	3.07(12)	5.51(38)
	11.0	1.238(63)					6.47(39)

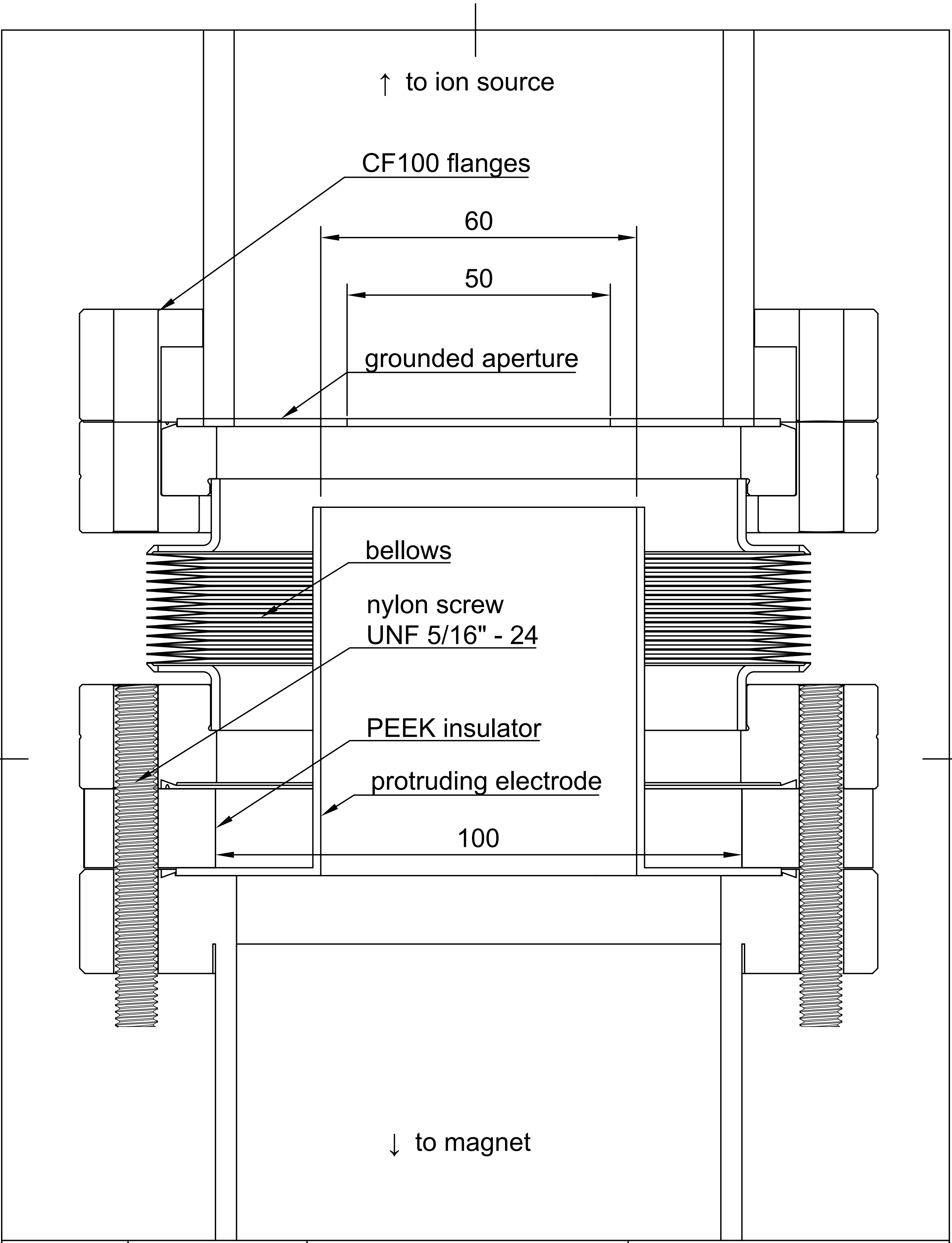

Dept.	Technical reference	Created by Felix Albrecht 18.12.23	Approved by
scale 1:1 measurements in mm		Document type	Document status
		Title BM I1 MBS electrode entry side	DWG No.
			Rev. / Date of issue / Sheet 1/1

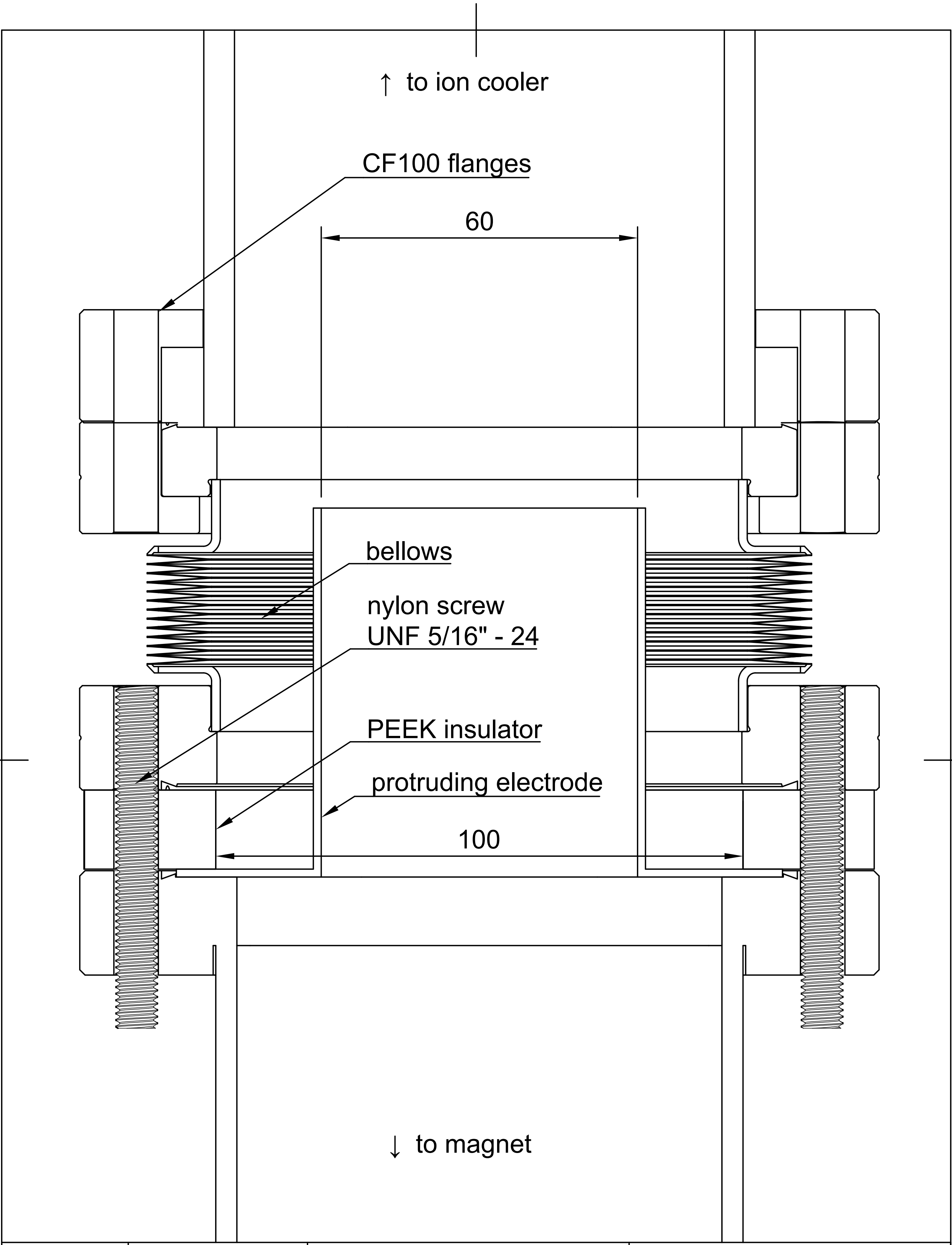

Dept.	Technical reference	Created by Felix Albrecht 18.12.23	Approved by
scale 1:1 measurements in mm		Document type	Document status
		Title BM I1 MBS electrode exit side	DWG No.
			Rev. | Date of issue | Sheet 1/1